

Fast, Accurate State Measurement in
Superconducting Qubits

©2014

Daniel Sank

July 29, 2014

Contents

1	Introduction	5
1.1	Information processing machines	5
1.1.1	Information is physical	5
1.1.2	Classical physics limits information processing	6
1.1.3	Quantum Information	8
1.1.4	Summary	10
1.2	Quantum Bits	11
1.2.1	Qubits are hard to make because quantum states are fragile	11
1.2.2	Requirements for a quantum computer	13
1.2.3	Candidate systems for qubits	14
1.3	Superconducting Qubits	16
1.3.1	Superconductivity allows quantum modes with engineered parameters	17
1.3.2	Superconducting circuits allow qubit engineering	17
1.3.3	Non-linearity: Josephson junction	18
1.3.4	Advantages of superconducting qubits	19
1.3.5	Disadvantages - outstanding challenges	20
1.4	Fault tolerance	21
1.4.1	Surface code	22
2	Measuring a Qubit's State	24
2.1	Measurement is hard	24
2.2	Examples	26
2.2.1	Charge measurement	26
2.2.2	Flux measurement	28
2.2.3	Inductance measurement	31
2.3	The transmon qubit - RF measurement	32
2.3.1	Qubit as a photo-detector	34
2.3.2	Energy measurement with travelling waves	35
2.3.3	Dispersive measurement	37
2.3.4	Filters	39

CONTENTS	2
-----------------	----------

3 Dispersive Measurement	42
3.1 Introduction	42
3.2 Dispersive Hamiltonian	42
3.3 Scattering	45
3.4 Qubit measurement	47
3.5 Fresnel lollipops - separation error	47
3.6 Measurement induced dephasing	48
3.7 Resonator energy to output power ratio	51
3.7.1 Resonator internal energy	51
3.7.2 Output power	52
3.7.3 Ratio	52
4 Bandpass Filter	54
4.1 Analysis	54
4.1.1 Analytic treatment	54
4.1.2 Numeric treatment	58
4.1.3 Discussion	59
4.2 Circuit parameters	59
4.3 Device	63
4.3.1 Layout	63
4.3.2 Filter	63
4.3.3 Measurement resonators	68
4.3.4 Mode shape coupling factor	72
4.3.5 Parameters	72
4.4 Fabrication	72
5 Experimental Setup and methods	74
5.1 Wiring	74
5.1.1 General view	74
5.1.2 Input line	75
5.1.3 Output line	77
5.2 Signal generation	78
5.3 Signal detection	79
6 Results	80
6.1 Characterization	80
6.1.1 Resonator frequencies	80
6.1.2 Coupling strength - g	80
6.1.3 Resonator transient response rate - κ_r	81
6.2 Photon number calibration	83
6.3 Stimulated qubit transitions	85
6.3.1 Comparison with theory	86
6.4 Coherence	88
6.5 Time dependence and accuracy	88
6.5.1 State preparation - heralding	88
6.5.2 Fidelity at fixed measurement time	88

CONTENTS	3
-----------------	----------

6.5.3 Time dependence	90
6.5.4 Multiplexed measurement	94
6.6 Measurement efficiency	94
A Quantum Mechanics Reference	99
A.1 Commutators	99
A.1.1 Products	99
A.1.2 Translation by an operator	99
A.1.3 Baker-Campbell-Hausdorff	100
A.1.4 Conjugate Variables	100
A.2 Pauli operators	100
A.2.1 Representation	100
A.2.2 Products and commutators	100
A.2.3 Translation	101
A.3 Rotating Frame	101
B Quantum Oscillator Reference	103
B.1 General Form	103
B.1.1 Zero point fluctuation	104
B.2 Algebra	104
B.3 Equations of Motion	105
C IQ Mixer	106
C.1 Modulation	106
C.2 Demodulation to baseband	107
C.3 Demodulation to DC	108
C.4 Demodulation Mixer Imbalance	109
D Formal Theory of Superconducting Qubits	110
D.1 Introduction - Parallel LC	110
D.2 Driving	111
D.2.1 Summary - Simple derivation	112
D.3 Coupling	113
D.3.1 Capacitive coupling	113
D.3.2 Summary - Simple derivation	115
D.4 Rotating Frame	115
D.4.1 Operators	116
D.4.2 Driving	116
D.4.3 coupling	119
E Discrete Fourier transform of White Noise	120
E.1 White noise	120
E.1.1 Distribution of r^2	123
E.2 Correlated noise	124

CONTENTS	4
----------	---

F External Loading of a Resonant Mode	126
F.1 Parallel-Series Equivalence	126
F.1.1 Large Q limit	127
F.2 Loaded resonant mode	127

Chapter 1

Introduction

This introductory chapter explains the notion of quantum information processing and why it might be useful.

1.1 Information processing machines

Information processing pervades our civilization. Examples of information processing, essential to our way of life include communication, data storage and retrieval, and problem solving machines. Digital information processing has become especially important since the invention of the vacuum tube, and later, the transistor. We spend enormous effort and resources improving our information processing hardware: in 2013 Intel spent more than ten billion dollars on research and development [10].

1.1.1 Information is physical

A computer contains an array of physical elements, such as gears in a mechanical computer, or transistors in an electronic one. The physical states of those elements stores information. In the mechanical computer the physical state is the rotational orientation of the gears, and in the electronic computer it is the current and voltage in the transistor. Physical interactions between elements, causing them to change their state, achieves computation. In a mechanical computer, sliding rods pushing on one another lead to the positions of a register of output rods that depend on the positions of the inputs. In a solid state electronic computer, arrays of input voltages are transferred from memory circuits into the central processing unit (CPU) where they interact in logic circuits such as NAND or XOR gates to produce resulting output voltages. Figure 1.1 illustrates two examples: a mechanical OR gate and an electronic NAND gate. These examples are meant to emphasize the fundamentally physical nature of information processors.

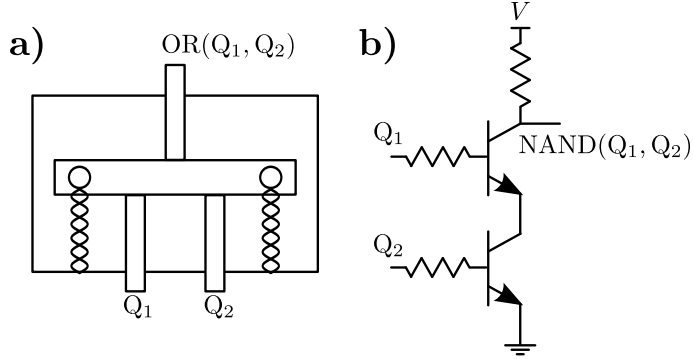


Figure 1.1: Two physical implementations of logic elements. a) A mechanical OR gate. If either of the bottom rods is pushed, the output rod extends. If neither input rod is pushed, springs retract the output rod. b) An electronic NAND gate. If voltage is applied to both input wires then current flows freely through the transistors, bringing the output node to ground.

1.1.2 Classical physics limits information processing

The above example computers, and in fact in any existing information processing device, ignore a great deal of information associated to the physical elements in the computer. A particular state of a transistor implicitly includes an enormous set of possible microscopic states (“microstates”) of the individual electrons carrying the current. This is illustrated in Fig. 1.2 where multiple microstates are shown for left flowing and right flowing macroscopic current states in a wire. Information processing in the computer is insensitive to these microstates by construction. Ignorance of this information is essential for the operation of a real machine: if the logical state of a transistor depended on the precise state of every electron, we would have to eliminate phonon scattering and operate at absolute zero temperature in order to have a usable machine. In other words, ignorance of precise microscopic dynamics affords the computer robustness against real-world non-ideal effects.

On the other hand, it turns out that this ignorance restricts the computer to physical processes which obey classical physics.¹ At any point in the computation, the computer’s state is described by independently specifying the state of each information storage element,

$$\begin{aligned} |\text{computer}\rangle &= |\text{state of } 0^{\text{th}} \text{ element}\rangle \dots |\text{state of } N - 1^{\text{th}} \text{ element}\rangle \\ \text{eg. } |0\rangle|1\rangle|1\rangle \dots |1\rangle|0\rangle|0\rangle &= |011\dots 100\rangle, \end{aligned} \quad (1.1)$$

where 0 and 1 indicate the two possible states of a logic element. Note that a system with N bits requires N 0’s and 1’s to specify its state. While this representation may seem obvious and unavoidable, from a physical point of view

¹A demonstration of *why* this is the case will be given subsequently.

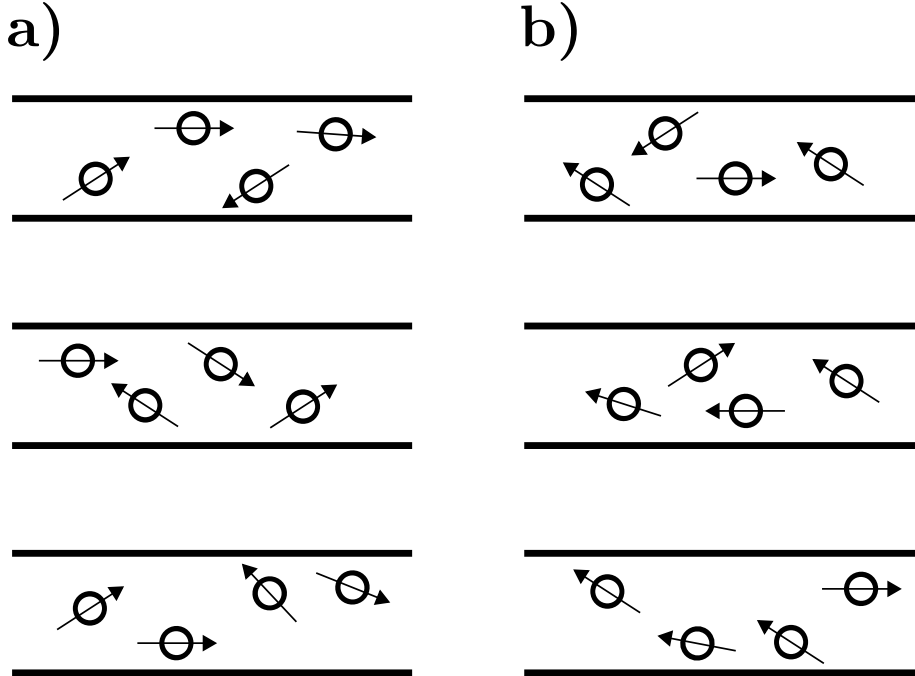


Figure 1.2: A wire with two different macroscopic current states.(a) and (b) show three microscopic states corresponding respectively to rightward and leftward current. Note that in each microscopic state some electrons may be moving in a direction against the macroscopic current.

it is somewhat limited. We know that Nature fundamentally allows for physical states more complex than the one in Eq. (1.1): quantum mechanics describes a physical state as a weighted superposition of states, such as $c_0|0\rangle + c_1|1\rangle$ where $\{c_i\}$ are complex numbers. These superposition states are more complex than their classical counterparts, so use of only classical states in information processors limits the their power.

Suppose we want to compute properties of N quantum two level systems where each one interacts with its nearest neighbours, a so-called “quantum spin chain”, as shown in Figure 1.3 a. The system is described by $2^N - 1$ complex numbers c_i ,²

$$|\text{spin chain}\rangle = c_0|00\dots 00\rangle + c_1|00\dots 01\rangle + \dots + c_{2^N}|11\dots 11\rangle. \quad (1.2)$$

Note that each term in the sum corresponds to one complete classical state of the spin chain as in (1.1). The number of parameters needed to specify *one particular* quantum state is proportional to the number of *all possible* classical

²Normalization and the irrelevance of the global phase reduce the parameter count by 2 real numbers, or equivalently one complex number.

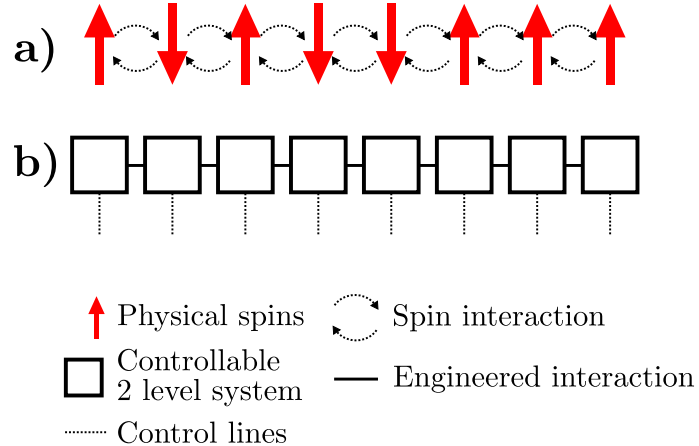


Figure 1.3: The physics of a quantum spin chain can be investigated by construction of a controllable and measurable analogue system. a) A physical spin chain. b) An array of two level systems engineered to match the physics of the spin chain.

states. Suppose each of the numbers c_i is represented in a classical computer by an m bit number. Then, to represent a single state of the quantum system we need $m2^N$ classical bits, so the size of the classical computer needed to simulate a quantum system grows exponentially in the size of the quantum system. This illustrates one limitation of classical computers: they cannot efficiently store the information needed to represent quantum mechanical physics problems.

That classical computers cannot efficiently simulate quantum mechanics is not too surprising since we know that quantum states are more complex than classical ones. However, classical computers seem to be limited even in their ability to solve abstract math and logic problems. A famous example of this is the problem of finding the prime factors of an integer. Although this problem has been known since ancient times, no polynomial time classical algorithm has ever been found.³ The best modern algorithm, the general number field sieve [16], factors a b bit number in time asymptotically proportional to

$$\exp \left((1.9 + o(1)) (b \ln 2)^{1/3} (\ln(b \ln 2))^{2/3} \right) \quad (1.3)$$

in the limit of large b . Note the super-polynomial (but sub-exponential) scaling.

1.1.3 Quantum Information

In the previous section, we showed that a quantum state cannot be efficiently stored on a classical computer. This problem suggests its own solution: use

³A simple but slow algorithm for deciding whether a number is prime and finding its factors is attributed to Eratosthenes of Cyrene (c. 276 BC - c. 195/194 BC).

an information processor in which the logic elements themselves are quantum mechanical. A simple approach is to build an analogous system out of elements that are amenable to experimental control and measurement, as shown in Figure 1.3 b. By engineering the analogue system to have the same physics (ie. same Hamiltonian) as the spin chain, we can infer properties of the spin chain from observations of the engineered system. A realistic analogue system for the spin chain could be a chain of ions trapped in an optical lattice. Existing technology allows for exquisite control and measurement of trapped ions. Note that this idea of building an analogous system, or “model” that is amenable to precise engineering and measurement is not restricted to quantum systems. Indeed, modeling has been used for architectural projects for centuries and is in some sense the oldest form of information processing.

The modeling approach works for systems in which the physics is simple enough that a controllable analogue system can be realized, but this will not always be possible. It is difficult to imagine building a controllable analogue system for a high energy particle scattering problem. For problems for which we cannot build models we need a more abstract approach. Historically, we addressed this type of problem by constructing a mathematical model of the physics problem and solving the model with a numerical computer. However, we already saw that a quantum state cannot be efficiently stored on a computer which uses classical physics. Looking again at Figure 1.3 b, we can re-imagine the array of controllable two level quantum elements, originally conceived as proxies for a spin chain, as a quantum bit register. This suggests the notion of a general purpose abstract computer that uses quantum bits instead of classical ones. Information would be processed by controlled interactions between quantum bits in the register. We could engineer the interactions between two quantum elements such that they undergo specific transformations, akin to the classical logic gates used in normal computers such as XOR and NAND gates. A quantum example is described by the following unitary matrix

$$\begin{array}{c|cccc} |00\rangle & 1 & 0 & 0 & 0 \\ |01\rangle & 0 & 1 & 0 & 0 \\ |10\rangle & 0 & 0 & 0 & 1 \\ |11\rangle & 0 & 0 & 1 & 0 \end{array}. \quad (1.4)$$

This operation is known as a “controlled NOT” or CNOT gate, because the state of the second bit inverts if the first bit is on (ie. in the $|1\rangle$ state). This example shares with the classical cases the general idea of using controlled interactions to produce changes in the bits representing a logical computation. Importantly, the quantum gate works on superposition states in addition to the usual classical states. Operations like this could form a collection of quantum logic gates analogous to classical logic gates, and we can imagine a generic Turing-style computer based on transformation of quantum states through such gates. Similarly to how the NOT and AND gates form a universal set of operations in classical computing, arbitrary single qubit controls along with the CNOT form a universal set for a quantum computer.

Amazingly, this kind of generic quantum information processor might be able to solve some types of abstract problems more efficiently than classical computers. A famous algorithm for factoring prime numbers, Shor’s algorithm [37], runs on a quantum computer in a time that goes as a polynomial in the number of input digits. This is an example of a case where a quantum computer solves an abstract problem more efficiently than a classical computer, and the practical applications of prime factoring in cryptography is a strong driving force behind quantum information research. It’s important to note that the current lack of a known classical algorithm for prime factoring does not preclude the possibility that one will be found in the future. It has not been proven that efficient factoring on a classical computer is impossible, and so the utility of quantum computers for abstract problem solving is not necessarily firmly established. On the other hand, there is one known problem that quantum computers can solve faster than is possible on a classical computer: function inversion. Given a function f , a set of possible inputs $\{x\}$ of length N , and an output y , the quantum “Grover Search” algorithm can find x such that $f(x) = y$ in time proportional to \sqrt{N} .⁴ Classically, the search time scales as N . This square root speed-up for the quantum algorithm is less impressive than the near exponential speed-up associated to Shor’s factoring algorithm, but is a strong indicator that quantum information processors are fundamentally more powerful than classical ones, at least for some types of problems.

1.1.4 Summary

Quantum information processors may be able to efficiently solve some problems that classical processors cannot. Quantum algorithms are known for prime factoring and function inversion. The former represents a significant speed-up over known classical algorithms and seems very likely to indicate that quantum processors are significantly more powerful than classical ones. The latter establishes that in at least one case quantum processors can solve problems faster than is fundamentally possible on a classical processor, although the speed-up is modest. Quantum processors seem to be clearly superior to classical processors for quantum physics problems as they can more efficiently store the information needed to represent the state of the system being simulated.

Two types of quantum information processors were described. In the first type the processor is simply a model of a physics problem and is used to directly measure properties of the analogous system. In the second type an array of quantum elements are used as an information storage register and computations are done through physical interactions between them, just as in a normal computer.

⁴The Grover Search is sometimes described as a database lookup. The connection to function inversion comes by choosing f such that $f(x) = \text{True}$ only when x is the desired database entry. Note that, on a normal computer, *structured* databases can be searched in constant time by using hash lookup or similar methods.

1.2 Quantum Bits

To build a quantum computer, we need quantum mechanical logic elements that are controllable and measurable. As in the classical case, these elements could have any number of possible states, but analysis and construction is simplest in the case of two possible states. With homage to the term “bit” for a controllable two-state information storage element in classical computers, we refer to the quantum analogue as a “**qubit**”. In this section we explain why building usable qubits is hard. With that understanding we explain the requirements for a working quantum computer. Finally we discuss a few possible candidate physical systems for making qubits.

1.2.1 Qubits are hard to make because quantum states are fragile

As discussed previously, classical computers are insensitive to many of the details of the physical processes taking place inside their bits. As indicated in Figure 1.2, the logical state of a transistor does not depend on the individual states of the electrons in the wire, but rather only on the average of those states. The following states correspond to upward current

$$\{|\uparrow\uparrow\uparrow\rangle, |\downarrow\uparrow\uparrow\rangle, |\uparrow\downarrow\uparrow\rangle, |\uparrow\uparrow\downarrow\rangle\} \quad (1.5)$$

and the following correspond to downward current

$$\{|\downarrow\downarrow\downarrow\rangle, |\uparrow\downarrow\downarrow\rangle, |\downarrow\uparrow\downarrow\rangle, |\downarrow\downarrow\uparrow\rangle\} \quad (1.6)$$

where $\uparrow(\downarrow)$ indicates a single electron carrying current upward(downward). The computer’s ignorance of the individual electron states means that if the system undergoes a transition

$$|\uparrow\uparrow\uparrow\rangle \rightarrow |\downarrow\uparrow\uparrow\rangle, \quad (1.7)$$

then the state of the transistor, and thus the logical state of the computer, does not change. For classical computers this is an essential feature: if the computer’s state depended on such microscopic processes we would have to completely eliminate all scattering processes in the wires, a seemingly impossible task. By remaining insensitive to these processes the classical computer can operate at finite temperatures with imperfect materials, etc. Now, it turns out that ignorance of these processes is also what makes the machine classical instead of quantum mechanical. To see why, suppose we have a pair of transistors in an initial quantum state

$$|\text{transistors}\rangle = |\uparrow\uparrow\uparrow\rangle|\uparrow\downarrow\downarrow\rangle + |\downarrow\downarrow\downarrow\rangle|\uparrow\uparrow\uparrow\rangle \equiv |1\rangle|0\rangle + |0\rangle|1\rangle \quad (1.8)$$

where $|1\rangle$ means upward current and $|0\rangle$ means downward current. Now suppose the first transistor suffers the transition given in (1.7). The resulting transition for the computer is

$$\begin{aligned} \text{physical: } & |\uparrow\uparrow\uparrow\rangle|\uparrow\downarrow\downarrow\rangle + |\downarrow\downarrow\downarrow\rangle|\uparrow\uparrow\uparrow\rangle \rightarrow |\downarrow\uparrow\uparrow\rangle|\uparrow\downarrow\downarrow\rangle + |\downarrow\downarrow\downarrow\rangle|\uparrow\uparrow\uparrow\rangle \\ \text{logical: } & |1\rangle|0\rangle + |0\rangle|1\rangle \rightarrow |1\rangle|0\rangle + |0\rangle|1\rangle. \end{aligned} \quad (1.9)$$

The logical state does not change so it appears that nothing important has happened. However, the electron state change cannot happen in isolation. If the electron state changes, it must be due to interaction with something else. Suppose the electron state change coincides with creation of a phonon in the wire. Adding the phonon state to our representation, we re-write the electron state change process as

$$\begin{aligned} & |\text{computer}\rangle \rightarrow |\text{computer}'\rangle \\ \text{physical: } & |\uparrow\uparrow\uparrow\rangle|\uparrow\downarrow\downarrow\rangle|0\rangle + |\downarrow\downarrow\downarrow\rangle|\uparrow\uparrow\uparrow\rangle|0\rangle \rightarrow |\downarrow\uparrow\uparrow\rangle|\uparrow\downarrow\downarrow\rangle|1\rangle + |\downarrow\downarrow\downarrow\rangle|\uparrow\uparrow\uparrow\rangle|0\rangle \\ \text{logical: } & |1\rangle|0\rangle|0\rangle + |0\rangle|1\rangle|0\rangle \rightarrow |1\rangle|0\rangle|0\rangle + |0\rangle|1\rangle|0\rangle \end{aligned} \quad (1.10)$$

where here the third ket being $|0\rangle(|1\rangle)$ represents the absence(presence) of the phonon. The information carried by the state of the phonon is not available to the computer, so to understand what information is still carried by the computer we must re-express the state without the phonon . On the left hand side of Eq. (1.10) the phonon is always in state $|0\rangle$, so the information available to the computer is easily written by dropping the phonon part

$$|\text{computer}\rangle = |1\rangle|0\rangle + |0\rangle|1\rangle \quad (1.11)$$

The right hand side of Eq. (1.10) includes terms where the phonon state is not always the same. It turns out that in this case, the state takes on a statistical nature⁵

$$|\text{computer}'\rangle = \begin{cases} |0\rangle|1\rangle & \text{probability} = 1/2 \\ |1\rangle|0\rangle & \text{probability} = 1/2 \end{cases}. \quad (1.12)$$

The state after the phonon scattering event, $|\text{computer}'\rangle$, is a statistical mix of either $|10\rangle$ or $|01\rangle$ with no quantum superposition. You can think of this as a collapsed wave function that occurs after the phonon measures the state of the first electron. With the quantum superposition in the computer state now gone, the computer's function is limited to processes described in classical physics.

It only required *one* electron state change in a phonon scattering event to cause the *complete* destruction of the computer state's quantum superposition. In a real transistor, with orders of magnitude more electrons, single scattering processes like the one illustrated here are overwhelmingly likely to occur with extremely high frequency. This explains why quantum coherence is so fragile and illustrates why normal computers are classical.⁶ The phenomenon illustrated here, by which quantum superposition of a subsystem is lost when it interacts with other degrees of freedom, is known as "decoherence". Identification of processes causing decoherence and elimination of those processes is one of the crucial challenges of experimental quantum information.

Decoherence in qubits is typically characterized by the rates of two types of processes. The first process is decay from $|1\rangle$ to $|0\rangle$ accompanied by absorption

⁵This can be shown rigorously using the density matrix formalism.

⁶In fact, what we have illustrated here may be the essence of why we do not observe quantum interference in common experience.

of a quantum of energy from the qubit by something in the surrounding environment. This process frequently occurs with constant probability per unit time and can therefore be described by an exponential time constant T_1 . The second process is randomization of the relative phase between $|0\rangle$ and $|1\rangle$, caused by fluctuations in the energy difference between those two states. This is typically characterized by a time constant T_2 , although in many systems the noise responsible for this process is correlated in time, so the decoherence does not go exponentially and must be described by a more complex function of time, such as $\exp[-t/T_{\phi_1} - (t/T_{\phi_2})^2 - \dots]$.

1.2.2 Requirements for a quantum computer

The requirements for a working quantum computer are summarized in the “Di-Vencenzo criteria” for a set of usable qubits:

1. Reliable qubit state preparation
2. Low qubit decoherence
3. Accurate quantum logic operations for single qubits and between pairs of qubits
4. Accurate measurement of the qubit states

Items 2, 3, and 4 are interrelated and warrant discussion. Low decoherence is not really a meaningful criterion by itself. If it were required that qubits maintain coherence for the entire duration of a quantum computation, the task would appear hopeless because the coherence would have to scale exponentially with the number of qubits. However it is theoretically possible to use qubits in an algorithm lasting much longer than their coherence times by using error correction. With quantum error correction, the important figure of merit is the ratio of the qubit coherence times to the time needed for an error correction cycle. Error correction typically involves several single and two qubit logic gates followed by projective measurement of a subset of the qubits, and succeeds in preserving the logical state of the computer if those operations and measurements are done with high enough accuracy and large enough system size. Therefore, in order to actually run a quantum computer, we need to be able to do only a few logic operations with high accuracy in times short compared to the qubit coherence times. Similarly the projective measurement must be done in a time short compared to the qubit coherence times, and must be done with high accuracy. The precise meaning of “high accuracy” will be discussed later.

From the previous section it is clear that there is an intrinsic tension between accurate control for logic operations and qubit coherence. By construction, the hardware coupled to the qubits to control their states introduces decoherence channels. The same is true for the apparatus used to measure the qubits’ states. Navigating this tension is the main challenge of experimental quantum information.

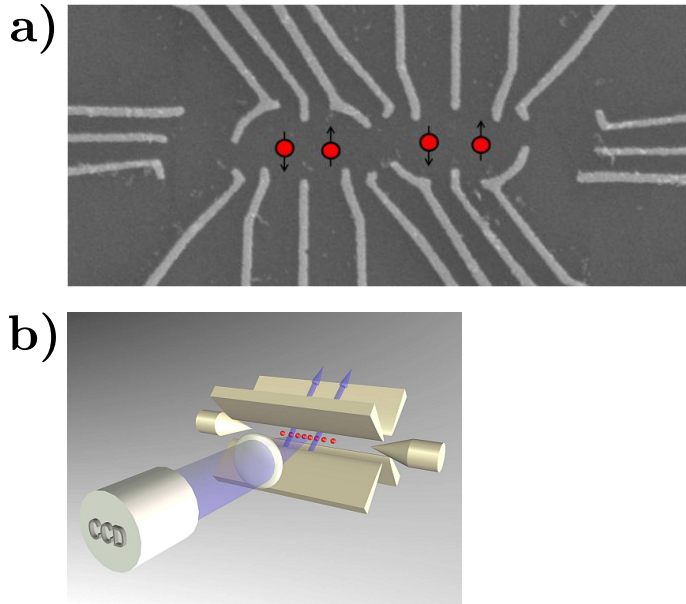


Figure 1.4: Qubit implementations. a) Electrons embedded in a semiconductor are used as qubits through their spin degree of freedom. This image shows a “double quantum dot” qubit in which two electrons are used to implement a single logical qubit. Note the large number of control wires needed to control this qubit. The image was taken from the website of Amir Yacobi at Harvard. b) Ions trapped in a linear “Paul trap”. Blue arrows indicate axes through which laser light is brought into the trap to control the qubit states. State measurement is done through a state dependent fluorescent technique and the outgoing light is collected by a CCD camera. The image was taken from the website of Rainer Blatt at Innsbruck.

1.2.3 Candidate systems for qubits

In this section we describe two real qubit implementations and discuss the challenges involved in using them to build a quantum computer.

Electron spin

Single electron spins have the natural advantage that they are two level systems by nature and can be controlled via their magnetic dipole moment. Typical experiments work with electrons embedded in semiconductors, as shown in Fig. 1.4 a. Metal electrodes formed lithographically on the surface of the semiconductor produce electromagnetic fields which contain and control the qubit states. A challenge with electron spin qubits is that the parameters of the qubit depend on microscopic properties of the semiconductor crystal in which the electrons are embedded. In engineering parameters of the quantum computer,

we are constrained not only by the general physics of electron spins in a crystal, but also by what materials can actually be realized. The problem of growing a material compatible with high accuracy two qubit logic gates is a subject of ongoing research.

Another challenge comes from the weak and short range nature of the dipole interaction, which requires that the electrons be kept very close together in order to perform two-qubit logic operations. This presents a challenge for bringing control wires into the system; the area needed by the control wires in Fig. 1.4a is large compared to the area of the qubits, which makes scaling to a large computer system difficult.

Trapped ions

Another very successful qubit system is a single atom. For each atom, two electron orbital states are chosen as the logic levels $|0\rangle$ and $|1\rangle$. This system has the advantage of relatively long intrinsic coherence times, as it is possible to choose electron levels for which conservation rules suppress spontaneous decay, as used in atomic clocks.

The single atom qubit suffers several challenges. First, their microscopic size and gaseous state requires that they be ionized and held in space by RF or optical laser fields, as shown in Fig. 1.4b [7]. Second, to remove scattering processes between the trapped ion and atmospheric molecules which would destroy the ions' quantum coherence, experiments must be done in ultra high vacuum. Third, the use of electron levels for which coupling to the electromagnetic field is suppressed necessitates the use of strong lasers to induce qubit state transitions. High power stable lasers are not part of a large consumer market, so ion trap labs must expend a great deal of time and effort to build lasers suitable for quantum computing. Finally, the coupling between the ions' logical states is intrinsically weak. While the ions, being charged, interact through the monopole Coulomb interaction, that interaction does not depend on the orbital state of the electrons. When an ion's electron changes orbital state, that ion's electromagnetic field changes only in higher multipole moments. With a single electron charge and subatomic displacement scales, the direct ion-ion interactions is too weak to be useful.

This last difficulty has been overcome in practice by using laser pulses to transduce the electron states to a vibrational motion of the ion within the trap, which then couples to the vibrational motion of other ions via the Coulomb force [39]. This strategy has been used to implement high accuracy two qubit logic gates [5].

The challenges found in the examples presented here can all be attributed fundamentally to the fact that the qubits are based on naturally occurring microscopic objects. Because of this, the parameters of the qubit system come from Nature rather than from our own design. In the next section we introduce a type of qubit that solves this problem.

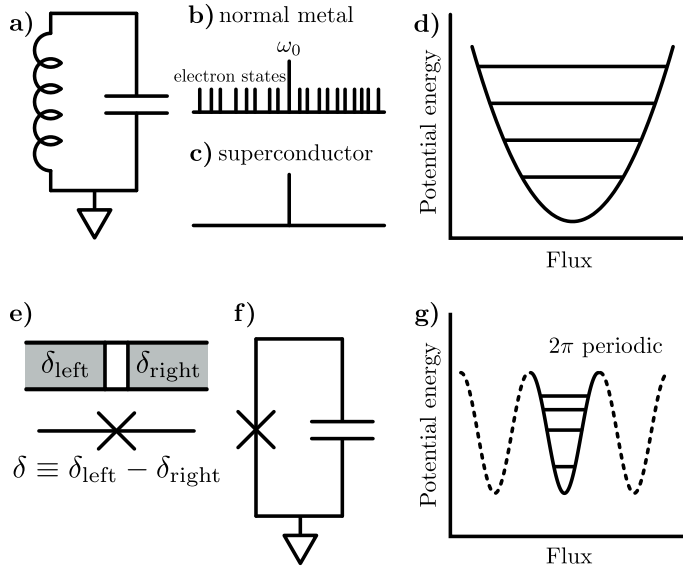


Figure 1.5: Superconducting qubits. a) A parallel LC circuit. b) The excitation spectrum of the system constructed with normal metal includes a dense set of electron excitations. These excitations interact with the circuit resonance and destroy quantum coherence. c) If the circuit is constructed with superconducting metal, the electron states vanish, leaving the circuit mode isolated and able to exhibit quantum coherence. d) The quantized mode of the LC circuit. The quadratic potential leads to equally spaced energy levels. e) A Josephson junction is formed by a thin insulating barrier interrupting two superconducting electrodes. The circuit model symbol for a Josephson junction is a cross. f) Replacing the linear inductor with a Josephson junction creates an anharmonic oscillator. g) The anharmonicity leads to unequally spaced energy levels. The lowest two levels can be used as a qubit.

1.3 Superconducting Qubits

Microscopic quantum objects like an electron spin or single atom constrain the design of an information processor because the processor inherits restrictions imposed by the fundamental physics of the microscopic system. Alternatively, we can start with an engineered system, like an electronic transistor, and try to make it quantum. This approach avoids restrictions imposed by eg. the values of fundamental constants on Nature.

1.3.1 Superconductivity allows quantum modes with engineered parameters

As discussed in section 1.2.1, the current and voltage state of a normal metal wire is not quantum because information is lost in internal scattering processes. To get rid of scattering we could use a superconductor. In a superconductor there is an energy gap above the ground state within which there are no available system excitations. As long as the superconductor is not subject to stimulation by energy near or exceeding this gap, the individual electrons remain in the superconducting condensate ground state. Therefore, processes like the one illustrated in Eq. 1.7 cannot occur and it should be possible to find quantum coherence in the macroscopic current.

Consider an LC circuit as shown in Fig. 1.5 a. From Kirchoff's laws we find the equations of motion for the charge Q on the capacitor and flux Φ in the inductor,

$$\dot{Q} = -\Phi/L \quad \dot{\Phi} = Q/C. \quad (1.13)$$

Solving these gives charge and flux oscillating at a frequency $\omega_0 = 1/\sqrt{LC}$. This mode corresponds to collective motion of the individual electrons in the metal. In a normal metal circuit there are many other degrees of freedom, such as the individual electron and phonon states. These degrees of freedom undergo constant scattering processes which prevent the macroscopic charge and flux oscillation mode from exhibiting quantum behavior, as illustrated in Fig. 1.5 b. However, if the electrons are all in the superconducting ground state, then there are no spurious microscopic processes and equation (1.13) represent the *only* dynamics in the system, as illustrated in Fig. 1.5 c. The absence of interaction with environmental degrees of freedom preserves the quantum coherence of the resonance mode, as explained in section 1.2.1. In that case we can represent the mode by a Hamiltonian for just the resonance degree of freedom

$$\hat{H} = \frac{\hat{Q}^2}{2C} + \frac{\hat{\Phi}^2}{2L} = \hbar\omega_0 (a^\dagger a + 1/2), \quad (1.14)$$

which, for the harmonic case, has a set of states spaced in frequency by $\omega_0 = 1/\sqrt{LC}$, as shown in Fig. 1.5 d. This is a remarkable idea: the collective motion of electrons in a superconducting resonant circuit should have quantum levels. This is surprising if we are used to quantum mechanics applying only to microscopic objects.

1.3.2 Superconducting circuits allow qubit engineering

The resonant system has many energy levels, and the bottom two levels could be used as a qubit. As the level spacing is determined by artificially engineered components L and C , we are at liberty to *engineer* our qubit's frequency for our convenience. Furthermore, it turns out that if we connect two circuits through a capacitor C_g , the coupling energy g normalized to their frequencies is [33]

$$\frac{g}{\hbar\sqrt{\omega_1\omega_2}} = \frac{1}{2} \frac{C_g}{\sqrt{C_1 C_2}}. \quad (1.15)$$

Here $\omega_{1,2}$ are the frequencies of the two circuits, and $C_{1,2}$ are their capacitances. The right hand side depends on no constants of Nature.⁷ As capacitors and inductors are routinely built with values ranging over many orders of magnitude, superconducting circuits provide a great deal of flexibility in designing a quantum computer. This should be contrasted against the situation with microscopic single particle qubits where intrinsic coupling strengths are constrained by constants of Nature.

1.3.3 Non-linearity: Josephson junction

The linear oscillator discussed above cannot easily be used as a qubit. In the harmonic system, driving the system into states which can carry out information processing requires measurement of complex quantities such as parity. One way to see this is to realize that an arbitrary array of linearly coupled harmonic oscillators is an analytically solvable problem. Classical computers use the nonlinear physics of the transistor to effect information processing. However, transistor physics is incompatible with the superconducting state. To build a quantum computer with superconductors we need a nonlinear superconducting element. Miraculously, there exists such an element: the Josephson tunnel junction [14]. A Josephson junction is a thin insulating barrier interrupting a superconducting wire, as shown in Fig. 1.5 e. The presence of the insulating barrier allows the superconducting condensate phases of the two electrodes to differ. We denote the phase difference as δ . Current and voltage at the junction are related to δ through the Josephson relations [14]

$$I = I_c \sin(\delta) \quad V = \frac{\Phi_0}{2\pi} \dot{\delta}. \quad (1.16)$$

Here I_c is the “critical current” of the junction and $\Phi_0 = 2 \times 10^{-15}$ Weber is the flux quantum. The critical current is related to the normal state resistance of the junction R_n and the superconducting gap Δ by the Ambegaokar-Baratoff relation

$$I_c = \frac{\pi\Delta}{2eR_n}. \quad (1.17)$$

Introducing the flux $\Phi \equiv \int V(t) dt$ and integrating the second Josephson relation gives a relationship between Φ and δ ,

$$\delta = 2\pi\Phi/\Phi_0. \quad (1.18)$$

Using Eq. (1.18), the Josephson relations become

$$I = I_c \sin(2\pi\Phi/\Phi_0) \quad V = \dot{\Phi}. \quad (1.19)$$

To lowest order in Φ/Φ_0 , the first of equations (1.19) is

$$\Phi \approx \frac{\Phi_0}{2\pi I_c} I. \quad (1.20)$$

⁷Of course, realizable capacitances are limited by the value of the electrical permittivity ϵ_0 . Still, realizable capacitance ranges over several orders of magnitude.

From the usual relation $\Phi = LI$, Eq. (1.20) gives a small signal inductance for the junction $L_{J_0} \equiv \Phi_0/2\pi I_c$. For arbitrary signals we compute the differential inductance

$$L_J \equiv V/\dot{I} = \frac{\dot{\Phi}}{2\pi I_c \dot{\Phi} \cos(2\pi\Phi/\Phi_0)/\Phi_0} = \frac{L_{J_0}}{\cos(\delta)} = \frac{L_{J_0}}{\sqrt{1 - (I/I_c)^2}}. \quad (1.21)$$

This relation shows that the Josephson junction is a nonlinear inductor, with inductance diverging to infinity as the current through the junction approaches I_c .

Integrating the work done on this nonlinear inductor gives an expression for the energy stored,

$$E = \int IV dt = \int I_c \sin(\delta) \frac{\Phi_0}{2\pi} \dot{\delta} dt = -E_J \cos(\delta) = -E_J \cos(2\pi\Phi/\Phi_0) \quad (1.22)$$

where $E_J \equiv \Phi_0 I_c / 2\pi$. Replacing the linear inductor with a Josephson junction, we get the circuit shown in Fig. 1.5 f, where the potential energy is now a cosine as shown in Fig. 1.5 g. In the cosine potential, the circuit oscillation frequency decreases with increasing amplitude. This is easily understood as a decrease in the oscillation frequency $\omega = 1/\sqrt{LC}$ as the junction inductance L increases with increasing current.

We now turn to the quantum mechanics of the nonlinear circuit. With the cosine potential from the junction, the circuit Hamiltonian becomes

$$\hat{H} = \frac{\hat{Q}^2}{2C} - E_J \cos(\hat{\delta}) = \frac{\hat{Q}^2}{2C} - E_J \cos(2\pi\hat{\Phi}/\Phi_0). \quad (1.23)$$

The energy levels of this Hamiltonian are shown in Fig. 1.5 g. Note that, unlike the case of the linear inductor with the parabolic potential, the energy levels in the junction circuit are unequally spaced. This makes it possible, by bringing two qubits' $|0\rangle \rightarrow |1\rangle$ transitions on resonance with one another, to effect useful information processing on pairs of circuits. Therefore, the circuit shown in Fig. 1.5 f can be used as a qubit.

1.3.4 Advantages of superconducting qubits

We already saw that superconducting circuits allow enormous flexibility in constructing the parameters for a quantum computer because the single qubit parameters and two-qubit couplings are determined by engineered design rather than by constants of Nature. Here we list some other important advantages.

- In order for a superconducting circuit to be used as a qubit, the spacing between its energy levels must be larger than the surrounding thermal energy scale. In other words, we need $\hbar\omega_0 \gg k_b T$. Conventional dilution refrigerators attain temperatures of ten to a few tens of mK. At $T = 20\text{mK}$ we would need a frequency of 3 GHz to keep the thermal occupation of

the qubit's excited state below a part in one thousand. This microwave frequency range is readily accessible with commercial electronic hardware. High quality tunable microwave sources available for a few tens of thousands of dollars are stable enough for use with superconducting logic gates with errors less than a part in one thousand. The commercial support in the frequency range needed for superconducting qubits is a major advantage.

- Due to the prevalence of CMOS technology, fabrication of electrical circuits is an extremely well developed industry. Even the most complicated superconducting qubit chips requiring seven layers of lithography can be made in a couple of days in an academic clean-room facility. Construction by photo-lithography also directly enables scaling to larger system sizes.
- Test and measurement instrumentation for electronics is extremely well developed. The dynamic range of standard microwave equipment such as spectrum analyzers, sources, and even arbitrary waveform generators allows the researcher to easily control and debug the superconducting qubit system. To give a sense of scale, microwave frequency DAC chips with 14 bit (42 dB) resolution are commercially available.
- The connectivity of a superconducting qubit network is subject only to the constraints of on-chip wiring. This allows for very complex connectivity, as illustrated by the DWave “chimera graph” in which some qubits are connected to up to eight other qubits [8].

1.3.5 Disadvantages - outstanding challenges

To complete the picture of superconducting qubits within the field of quantum computation, we list some of their disadvantages and outstanding challenges.

- The large size of superconducting qubits makes them susceptible to decoherence processes. A single superconducting qubit may interact with millions of material defects on the metal surfaces, and inside the tunnel junction or capacitor gaps. These processes have limited the coherence time of the phase qubit to $\sim 1 \mu\text{s}$, and have rendered the charge qubit essentially unusable.
- Superconducting qubits are not true 2-level systems. The one dimensional potentials admit higher quantum levels which can be inadvertently populated during information processing. Unwanted transitions to higher levels devastate information processing protocols, as the qubit leaves the expected space of states. In some types of qubits, such as the flux and fluxonium qubits, the nonlinearity from the Josephson junction can be large enough that this is not a problem in practice. However, in the transmon, the $|1\rangle \rightarrow |2\rangle$ transition frequency differs from the $|0\rangle \rightarrow |1\rangle$ transition frequency by only 3 to 4%. This small nonlinearity places restrictions

on the speed of quantum gates in transmon qubits, and complicates two-qubit interactions, as the unwanted $|1\rangle \rightarrow |2\rangle$ transition must be carefully avoided.

- Superconducting qubits rely on the disappearance of scattering states in the superconducting state to maintain coherence. This requires the devices be placed in a cryostat to keep the temperature below the critical temperature of the superconducting material. Furthermore, the temperature must be such that $k_b T \ll \hbar\omega_{\text{qubit}}$. With $\omega_{\text{qubit}}/2\pi \approx 4 \text{ GHz}$ to 10 GHz , this requires $T \lesssim 200 \text{ mK}$. Such low temperatures require Helium dilution refrigerators, limiting the available space for the experiment and accessibility for control wiring. The Helium dilution process relies on ^3He , which is rare and expensive.
- Unlike qubits based on individual microscopic particles, the individual qubits in a large array of superconducting qubits are not all guaranteed to be identical. Imperfections in the fabrication process of superconducting qubits leads to devices with different inductance and capacitance. In systems where the oscillation frequency of the qubits cannot be tuned *in situ*, this poses a serious challenge. Qubits with tunable frequency largely mitigate this problem.

1.4 Fault tolerance

Even in the superconducting state, the qubit oscillating mode interacts with external degrees of freedom. Charged quasiparticle excitations of the superconducting condensate can absorb quanta of energy from the qubit as they tunnel across the Josephson junction. Charged material defects, in the junction or in the qubit capacitors, feel the oscillating electric field of the qubit mode and can also absorb energy. Superconducting qubits are macroscopically large, so we do not expect that these and other decoherence processes can ever be completely eliminated.

Suppose we were to try to build a quantum computer which would work in the presence of decoherence processes. As illustrated in section 1.2.1, a single interaction even between the qubit and an external mode can destroy the coherence of the quantum state. Therefore, we would have to reduce the rate of such events to the level that the probability of a single event is of order 1 or less over the entire duration of the quantum algorithm. The numbers are not favorable. The most efficient useful algorithms require a number of qubits $n_{\text{qubits}} \approx 100$ and a number of gates $N_{\text{gates}} \propto N_{\text{qubits}}^3$. The probability that a single qubit with coherence time T_{coh} does not suffer a decoherence event is⁸

$$P = e^{-t/T_{\text{coh}}}. \quad (1.24)$$

⁸The discussion here pertains only to decoherence processes which are described as an exponential decay, ie. with a rate. Not all decoherence processes produce exponential decay, most notably the low frequency flux noise responsible for phase decoherence in superconducting qubits. Still, the essence of the present discussion remains intact.

Denoting the total algorithm time as T_{alg} , the number of gates in the algorithm N_{gates} , and the time of a single gate as T_{gate} , we find

$$\ln P = -\frac{T_{\text{alg}}}{T_{\text{coh}}} = -N_{\text{gates}} \frac{T_{\text{gate}}}{T_{\text{coh}}}. \quad (1.25)$$

To get a reasonable probability of the qubit remaining coherent, say $P = 1/2$, the coherence time to gate time ratio is

$$\frac{T_{\text{coh}}}{T_{\text{gate}}} = -\frac{N_{\text{gates}}}{\ln P} \gtrsim 10^6 \quad (1.26)$$

where in the last step we assumed $N_{\text{qubits}} = 100$ and $N_{\text{gates}} = N_{\text{qubits}}^3$. Current state of the art qubit systems achieve $T_{\text{coh}}/T_{\text{gate}} \approx 300$ [3]. Improving coherence by a factor of 10^4 is a daunting task, but even more importantly, qubit gate errors can also come from the control pulses used to generate the gates. This means that the error per gate from the control pulses must also be at the 10^{-6} level. Current state of the art for two qubit gates is a bit worse than 10^{-3} [3].

So far, we have discussed the error rate for a single qubit. However, the quantum computation is spoiled if *any* qubit suffers an error. This lowers the necessary error rate by a factor of N_{qubits} , which is at least a few hundred for useful algorithms. This puts the required error rate per qubit gate at 10^{-8} , an apparently impossibly low number. From this discussion we see that brute force improvement of qubit errors is not a viable strategy for building a quantum computer. Fortunately, there is better way.

It turns out that quantum information can be processed in way that tolerates errors. The details of how this works are beyond the scope of this thesis, but we explain the basic idea here. First, consider the state of a transistor in a classical computer. As discussed in section 1.2.1, the transistor state tolerates errors simply because it averages over the states of many electrons. In other words, the information represented by the effectively perfect transistor state is distributed over many smaller and imperfect elements. This allows feedback circuitry to stabilize the current in the transistor. In a similar way, quantum information can be distributed over an array of many imperfect qubits in such a way that faults on the individual qubits do not ruin the quantum information represented by the whole array. Several schemes exist, but we focus on a particular one called the “surface code”.

1.4.1 Surface code

In the surface code, a single qubit of quantum information is encoded into a two dimensional array of imperfect, physical qubits [12, 27]. The single qubit of information encoded in the array is called a “logical qubit”, as distinguished from the physical qubits. The array is stroboscopically measured in such a way that individual qubit errors are detected, while the logical qubit is not. In this way, the quantum state of the logical qubit can be maintained for times greatly exceeding the coherence times of the physical qubits. Error detection

and correction protocols like the surface code were a critical development in the field, as they render realistic quantum hardware useful for applications in a quantum computer.

The surface code is a cyclic protocol. The physical qubits are manipulated through unitary transformations as part of the error detection sequence, a subset of the qubits is measured, and then the processes is repeated indefinitely throughout the algorithm. For the surface code to produce a logical qubit with coherence exceeding that of the physical qubits, the error rate per qubit per surface code cycle must be on the order of 1%, much more lax than the one we found for the brute force approach. Still, to archive the 1% error per cycle threshold, the repetition rate of the protocol must be fast compared to the physical qubits' coherence times. In particular, the time of the qubit state measurement must be $T_{\text{measure}} \lesssim T_{\text{coh}}/100$, with an accuracy of at least 99%. Achieving these specifications is the main goal of the work in this thesis.

Chapter 2

Measuring a Qubit's State

In this chapter, we discuss the basic physics of state measurement in superconducting qubits. We give a physical and historical picture of state measurement so that the reader will more easily understand the motivation for the work done in this thesis, and the technical details presented in following chapters.

The chapter is divided into three parts. In the first section we explain why state measurement is generally a hard problem and list the requirements for state measurement in a quantum computer. In the second section, we discuss the basic measurement mechanisms used in several different types of superconducting qubits. In the third section, we explain the rationale behind the state measurement mechanism used in the latest superconducting qubits and describe how the work in this thesis was intended to improve upon prior techniques.

2.1 Measurement is hard

Constructing an apparatus to measure the quantum state of a superconducting qubit is inherently difficult. In order to measure the qubit state, we need to physically couple the qubit to some kind of measurement apparatus, but this introduces unwanted decoherence channels. A good measurement system must accurately distinguish the quantum states of the qubit on demand, without spoiling the fragile coherence of the state during the coherent control phase of the computation. Here we list the criteria required of a state measurement system for superconducting qubits.

1. **Accuracy:** Existing theoretical protocols for quantum fault tolerance require qubit state measurement with accuracy of at least 90% if all other parts of the computer, such as the logic gates, operate flawlessly. However, in a real system with imperfect gates, current protocols require accuracy of $\sim 99\%$. Therefore, we need to be able to distinguish the two computational states $|0\rangle$ and $|1\rangle$ with 99% accuracy.

The computational states differ by one microwave photon of energy. Microwave photons, being 10^6 times less energetic than optical photons, are

too low energy to be directly counted with high accuracy. Energy measurement is therefore not viable, and we have to find other properties of the qubit to use for state discrimination. Two obvious candidates are the circuit's charge and flux. If $|0\rangle$ and $|1\rangle$ correspond to different mean values of charge and flux, ie. $\langle \hat{Q} \rangle_0 \neq \langle \hat{Q} \rangle_1$ or $\langle \hat{\Phi} \rangle_0 \neq \langle \hat{\Phi} \rangle_1$, then we can use a charge or flux measurement to distinguish the qubit states. The charge difference between the qubit states is at most $2e$, and the flux difference is at most Φ_0 .¹ Distinguishing these weak signals with the needed accuracy requires exquisitely sensitive and highly specialized detection hardware. In order to couple to such weak signals the measurement hardware must be integrated onto the same chip as the qubits, meaning that the detector fabrication steps must be compatible with the fabrication of the superconducting qubits themselves. Despite these difficulties, charge and flux measurement with high accuracy is possible, as we will see below.

The requirement of high accuracy also means that the measurement time must be a small fraction of the qubit lifetime so that the qubit does not change state during the measurement.

2. **Fast repetition:** In order to be useful in cyclic fault tolerance protocol like the surface code, any reset time in the measurement apparatus must be short compared to the qubit life time. If it is not, then the qubits will lose coherence while the computer waits to be able to use the measurement system.
3. **Coherence:** The measurement apparatus itself must not spoil the quantum coherence of the qubit states during the coherent part of the computer's operation. The process of measuring a quantum state destroys its coherence by construction, so it is essential that the measurement process can be switched off. If it cannot, then the qubit lifetime can never exceed the measurement time. Furthermore, the measurement system must not inject noise into the qubits or load them with too much damping.²
4. **Non-demolition:** For the purpose of fault tolerance, when measuring a qubit we want to know which state it was in when the measurement was first turned on. Once we have that information, the qubit does not have actually have to be in that same state at the end of the measurement. As long as we know which state the qubit was in at the end of the measurement, we can put it into whatever other state we wish with control pulses. A measurement process in which there is a one to one correspondence between the measurement output and the final state of the measured system

¹To give an intuitive idea of these scales we can consider the voltage or current sensitivity needed to measure them. One electron charge on a capacitance of 1 pF gives a voltage of $0.16\mu\text{V}$, and larger capacitance, including parasitic capacitance, lower the voltage. One Φ_0 of flux in a 2 pH loop induces 1 mA of current, and again larger inductance lowers the current.

²Injection of noise and damping are actually fundamentally the same thing, but it is useful to think of them separately for the sake of intuitive reasoning.

is said to be “non-demolition”. A measurement system without this property leaves the qubit in an *unknown* state after measurement, in which case the qubit cannot be reliably reused.

5. **Multiplexing:** In order for a qubit measurement system to be usable in a quantum computer, it must work not only for single qubits, but for large qubit *systems*. This requirement means that the measurement apparatus should be comparable to or smaller than the qubits in size, and should not significantly increase the number of control wires needed to operate the computer.

We will keep these criteria in mind as we consider examples of qubit state measurement systems, and comment on how each example does or does not satisfy each criterion.

Note that the criteria presented above and the ensuing discussion are focused on the case of strong projective measurement as appropriate for a surface-code style fault tolerant system. Other fault tolerance strategies using continuous “weak” measurement have been proposed and are the subject of ongoing research.

2.2 Examples

This section discusses a few existing superconducting state measurement systems. The purpose of the section is to understand the practical difficulties in meeting the criteria given in the previous section, and to get a historical picture of state measurement in superconducting qubits.

2.2.1 Charge measurement

The first time resolved observation of quantum coherence in an electrical circuit was done in 1999 in a charge qubit [23]. A charge qubit consists of a superconducting island or “box” coupled to charge reservoir (ground) very weakly through a Josephson junction, as shown in Fig. 2.1. The $|0\rangle$ and $|1\rangle$ states of the qubit correspond to either zero or one extra Cooper pair having tunneled from the reservoir to the island. Because the coupling between the island and ground is so weak, the wave function of the qubit is very narrow in the charge basis, and the charge can be thought of as a well-defined classical variable. This allows the $|0\rangle$ and $|1\rangle$ states to be distinguished through charge measurement. A probe electrode is connected weakly to the island through another Josephson junction. This probe electrode is voltage biased such that when the circuit is in $|1\rangle$ with an extra Cooper pair on the island, two individual electrons can sequentially tunnel out of the island through the probe junction, changing the qubit state from $|1\rangle$ to $|0\rangle$ in the process. The tunnelling occurs stochastically with a rate set by the parameters of the probe junction and of the qubit. The slight change in island voltage when the qubit is in $|0\rangle$, combined with the probe bias voltage, blocks electron tunneling through the probe junction via the Coulomb

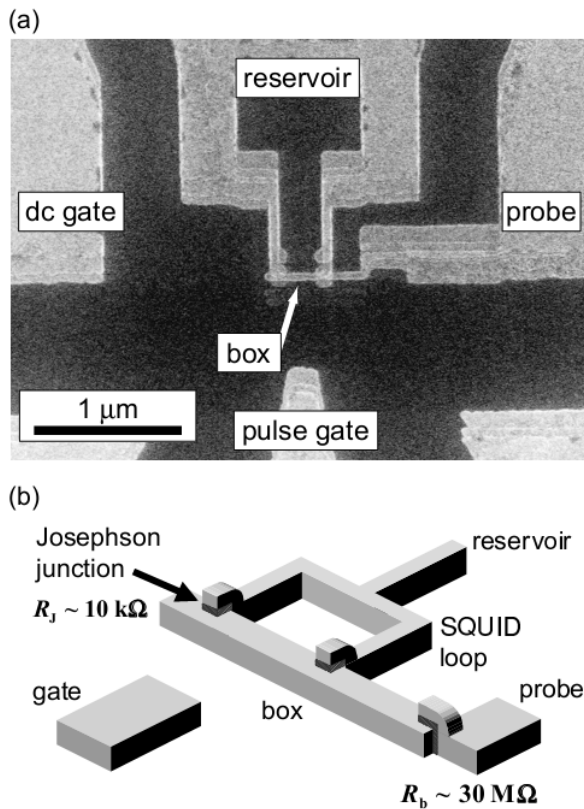


Figure 2.1: The charge qubit used in the first time resolved superconducting qubit measurements. (a) Micro-graph of the device in which can be seen the charge reservoir and superconducting island (“box”). The probe electrode on the right is used for charge based state detection. Note the extremely small scale of the device. This was needed so that the self capacitance energy would be much smaller than the junction tunneling energy, which allows charge to be a well-defined (ie. semiclassical) quantity. (b) Schematic of the device showing the geometry of the reservoir, box, and probe electrodes. The image was taken from Ref. [22].

blockade effect [22]. In this way the qubit states were discriminated based on the detection of charge tunneling through the probe junction.

This measurement system has two shortcomings. First, because the measurement worked through random tunneling of electrons out of the island, with a corresponding transition of the qubit from $|1\rangle$ to $|0\rangle$, it was by construction a decoherence channel for the qubit. The probe junction and its associated decoherence channel is always present, so the the excited state of the qubit could never live longer than the rate at which electrons tunneled out of the island through the probe junction. This means that the qubit coherence time could not exceed the measurement time. Also, the measurement required detection of an extremely weak charge signal, just two electrons. In the original experiment the authors repeated measurements many times to integrate over many two-electron detections, thus improving the signal to noise ratio enough to distinguish the two qubit states.

In a later experiment, a single electron transistor (SET) was used to detect the charges [1]. The SET is sensitive enough that the visibility of a single-shot measurements was increased to 87% and 93% for the $|0\rangle$ and $|1\rangle$ states respectively, bringing the accuracy near the threshold needed for a quantum computer. Second the tunneling process could be turned on and off with voltage biases applied to the readout circuitry, thus satisfying the decoherence criterion. The measurement circuit needed to be pulsed on for only 300 ns, while the qubit life time was observed up to 5.8 ns with the measurement off. Unfortunately, the device had a long reset time of 2 ms, thus failing the fast repetition criterion. Furthermore, a single SET was never shown to measure more than a single qubit, and multiplexed readout with a SET is thought to be prohibitively difficult [44].

A more fundamental problem is that the charge qubit itself has not been shown to permit the coherence and precise control needed for use in a quantum computer. Because the wave function is narrow in the charge basis, small noise charges near the qubit lead to random phase noise in the its quantum state, causing loss of coherence. The charge qubit is so sensitive to charge noise that practical noise levels render it unusable unless it is operated at a specific frequency at which it has a first order insensitivity to charge noise. Not only is this single frequency operation a major constraint, but the charge noise is so large that even operating at the insensitive point the charge qubit has not yet been shown to permit the degree of control and coherence in a multi-qubit system needed for a quantum computer. As such it has mostly been abandoned as a candidate for a quantum computer.

2.2.2 Flux measurement

Flux qubit

In the same year as the first time domain measurements in a charge qubit, quantum behavior was observed in a qubit where the wave function is narrow in the flux basis [20, 40]. This qubit, named the “flux qubit” uses three junctions in a superconducting loop, as shown in Fig. 2.2 a. When the circuit is biased by

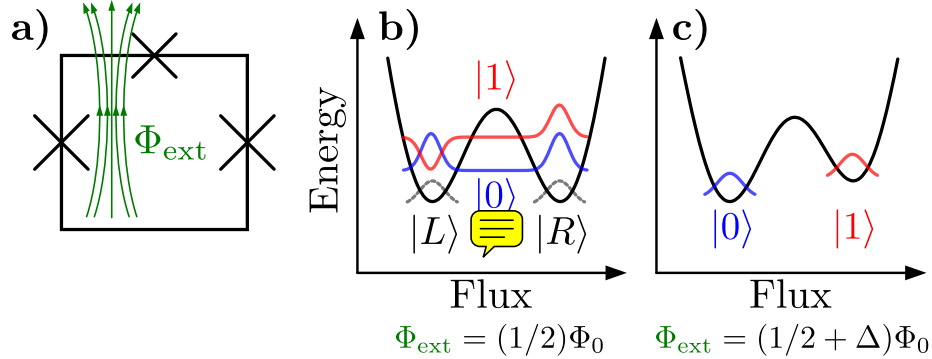


Figure 2.2: Potential energy curves and circuit diagram for the flux qubit. a) The flux qubit is a superconducting loop interrupted by three Josephson junctions. An external bias flux Φ_{ext} controls the shape of the energy potential. b) When the system is biased by an external flux of $\Phi_0/2$ the potential is symmetric. In the absence of quantum tunneling, there would be two degenerate ground states localized within the potential wells, as shown in gray. Tunneling causes these states to hybridize into symmetric and anti-symmetric state as shown in blue and red respectively. c) When the external flux bias is changed from $\Phi_0/2$ (increased or decreased) the degeneracy of the left and right states is removed, and $|0\rangle$ and $|1\rangle$ localize into the left and right wells.

an external magnetic flux equal to $\Phi_0/2$ the potential takes a symmetric double-well shape. If the energy barrier separating the two minima were infinitely large, then the system would have two degenerate ground states $|L\rangle$ and $|R\rangle$ as shown by the gray curves in Fig. 2.2 b. With the finite height of the barrier and the nonzero width of the wave functions, the left and right localized states hybridize to form one symmetric and one anti-symmetric state as illustrated by the blue and red curves. These states are the $|0\rangle$ and $|1\rangle$ states of the qubit.

The qubit states shown in Fig. 2.2 b have the same mean flux and charge (the values are zero). This degeneracy precludes discrimination between the states. As the degeneracy arises fundamentally from the reflection symmetry of the potential, changing the external bias flux breaks the symmetry, and lifts the degeneracy, as shown in Fig. 2.2 c. A small change in the bias flux causes one well to become lower in energy than the other. When this happens the hybridization of the two states within the energy wells decreases and the states become more localized. If this change is made slowly with respect to the frequency of the $|0\rangle \rightarrow |1\rangle$ transition, then the system will remain in whichever energy state it was in initially. Therefore, if the system starts out in $|0\rangle$, the lower energy state, then after the change in external flux it will be in the left well. On the other hand, if the system starts out in $|1\rangle$, then after the flux change it will be found in the right well. The horizontal axis of the plots in Fig. 2.2 is the self flux of the qubit circuit loop, so measurement of magnetic field near the loop yields a measurement of the qubit state. This strategy was used in Ref. [40].

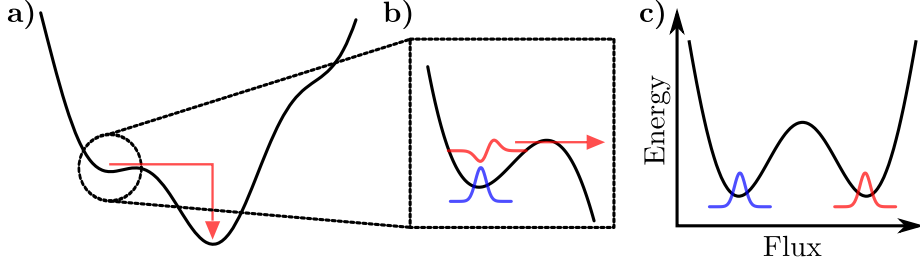


Figure 2.3: The phase qubit. a) The phase qubit is operated such that the wave function sits in an asymmetric shallow well of the potential energy. Tunneling out of this well is used as a mechanism for measurement. b) The ground (blue) and excited (red) states in the shallow well are meta-stable. By momentarily lowering the height of the potential barrier, the excited state tunnels out of the well, while the ground state remains in the well. c) Once the excited state has tunneled, external bias is used to bring the potential into a symmetric shape where the states are separated by a large flux and can be measured with a SQUID.

This measurement technique has a major advantage. The left and right wells are separated by a flux difference of nearly Φ_0 , which is a large enough flux to be detected by a superconducting quantum interference device (SQUID) magnetometer with very high signal to noise ratio. Therefore, the flux qubit state can be measured in a single shot. Although single shot measurement was not achieved in the original work of Ref. [40], it has become routine in subsequent works using SQUID based measurement.

SQUID readout has several disadvantages. Operation of a SQUID leads to generation of electrons excited into states above the superconducting gap. These excited electrons can interact with the qubit mode, so they impose a decoherence channel. Furthermore, this measurement strategy requires a dedicated SQUID for each qubit, which complicates scaling to larger systems.

Phase qubit

Another double-well qubit, the “phase qubit” was introduced in 2002 [18]. The wave functions of the phase qubit are so narrow in the flux basis that they would not normally feel enough of the anharmonic shape of the potential wells to behave with the non-linear character needed for a qubit. To recover the non-linearity, a bias (current in the original work, but flux in later versions) introduces asymmetry in the potential, making one of the wells very shallow, as shown in Fig 2.3 b. In this arrangement, the wave function feels the asymmetric potential shape enough to form unequally spaced levels. The two logical states of the qubit are the ground and first excited states of this shallow well.

To measure the state, we selectively tunnel the the excited state into the right potential well, as shown in Fig. 2.3. a short bias pulse is used to momentarily

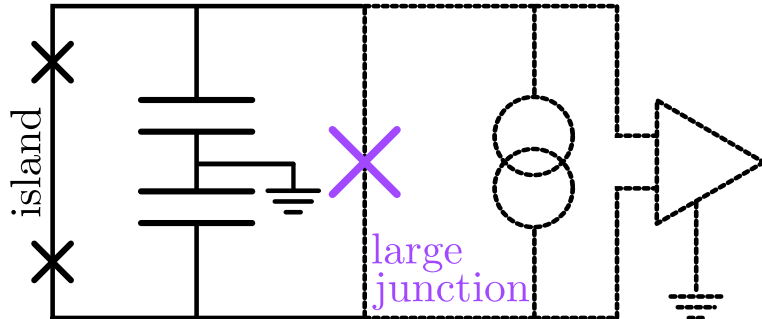


Figure 2.4: The quantronium qubit. The leftmost branch is essentially a charge qubit with two junctions connecting the island to the reservoir. The extra capacitance in the next branch reduces the quantronium’s sensitivity to change noise. The rightmost three branches, shown in dotted line, are used for measurement. With the current source off, the circuit mode is symmetric from top to bottom and does not couple into the amplifier or large junction. Turning on the current bias breaks this symmetry, and when the large junction switches to the voltage state that voltage is measured by the amplifier.

lower the height of the barrier seen in Fig. 2.3 b. This allows the excited state to tunnel out of the shallow left hand well and fall into the deep right hand well. The ground state remains in the left hand well. The bias is then changed to bring the potential into the symmetric shape shown in Fig 2.3 c where the two states can be distinguished by their now different fluxes using a SQUID.

The benefit of this measurement strategy is that the states can be distinguished with $> 90\%$ accuracy using a very fast measurement pulse. However, there are several drawbacks. The flux leads to be measured with a SQUID, which has all the problems mentioned in the discussion of the flux qubit. Additionally, the decay of the tunneled excited state to the bottom of the right hand well is a dissipative process. Emission of energy during this process has been observed to drive neighboring qubits into excited states, causing measurement cross-talk errors. Finally, practical reset times for the phase qubit are in the tens to hundreds of microseconds, which is much too long compared to the coherence times of currently available devices.

2.2.3 Inductance measurement

Also in 2002 a superconducting qubit called the “quantronium” was introduced [41]. This device has characteristics in between those of the charge and flux qubits. A circuit diagram of the quantronium is shown in Fig. 2.4. Focusing first on the part of the circuit drawn with solid line, the device is essentially a charge qubit: a superconducting island coupled to a charge reservoir through a junction, but here the single junction of the charge qubit is replaced by a nominally symmetric pair of junctions. This branch is shunted by a parallel capacitance.

The additional capacitance causes the qubit wave function to broaden in the charge basis while simultaneously narrowing in the flux basis, which reduces sensitivity to charge noise.³ Note that due to the symmetry of the circuit, the qubit mode has equal voltage on the top and bottom (points A and B in Fig. 2.4).

The quantronium uses an integrated measurement circuit, as illustrated by dotted part of Fig. 2.4. The measurement circuit consists of a large Josephson junction, a current source, and a voltage amplifier connected in parallel with the qubit. In normal operation the current bias current is set to zero, and in that case, because of the symmetry of the circuit, the qubit oscillation mode couples neither to the large junction nor to the amplifier. This prevents the readout circuit from loading the qubit with a decoherence channel.

To measure the state of the quantronium, the bias current is pulsed on. The current pulse divides between the branch with the small junctions and the branch with the large junction. The pulse height is nearly the critical current of the large junction. Depending on the state of the qubit, the inductance of the small junctions will be slightly different, and additional current may flow into the large junction, causing the total current to exceed the large junction's critical current. This causes the large junction to switch out of the superconducting state and produce a voltage pulse which is detected by the amplifier. The important feature of this system is that the readout circuitry does not couple to the qubit mode during normal operation. Only when the current source is turned on does the qubit mode couple to the readout circuit. This prevents the readout system from introducing unwanted decoherence into the qubit while the measurement system is off.

Still, this system has disadvantages. Exceeding the large junction's critical current to produce a voltage signal generates electron excitations above the superconducting gap, just like the SQUID used to measure flux qubits. Additionally, this system requires a bias current and voltage amplifier for every qubit, which would bring a large and difficult to engineer overhead into design of a quantum computer. However, as is the case with the charge qubit, the most important problem is that control of the quantum state of quantronium qubits has not been demonstrated to be accurate enough to effect the single and multiple qubit logic gates needed for a quantum computer.

Note that this system does not directly measure charge or flux. The switching of the large junction depends on the qubit state through the intrinsic inductance of the small junctions, rather than on an electric or magnetic field produced by the circuit.

2.3 The transmon qubit - RF measurement

As of this writing, the only superconducting qubit which has been demonstrated to support high accuracy control in single and two qubit logic gates is the

³Reduced charge noise incurs increased flux noise, but with the parameters used at the time this change lead to an over-all improvement in the device performance.

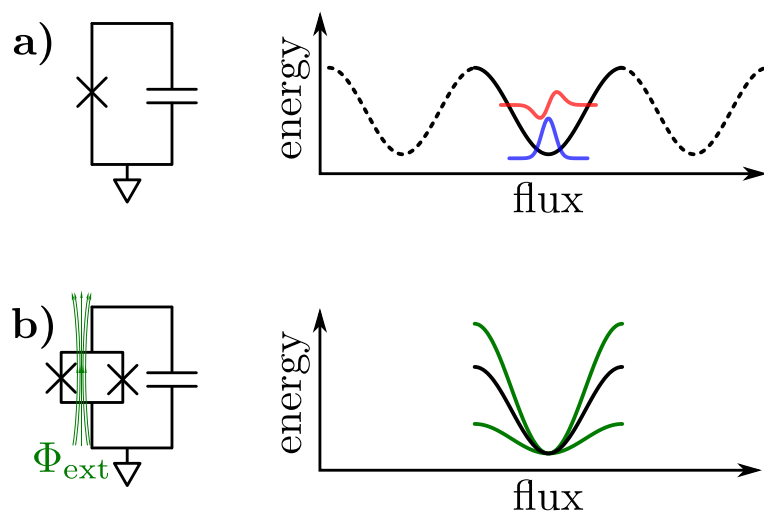


Figure 2.5: The transmon circuit and energy potential. a) The transmon is similar to a parallel LC oscillator, but with a nonlinear inductor. The potential energy has the shape of a cosine, and the large C , analogous to a large mass, prevents the wave functions from tunneling between wells. b) The single junction is replaced by a loop with a pair of junctions. External flux is used to modulate the effective critical current of the loop, which changes the height of the potential energy. This in turn causes the resonance frequency to shift.

transmon [3]. The basic transmon circuit is shown in Fig. 2.5 a. It is essentially an LC oscillator, but with a Josephson junction in place of a normal inductor to make it non-linear. This is precisely the simple circuit we considered in Chapter 1 with the Hamiltonian

$$H = \frac{Q^2}{2C} - E_J \cos(2\pi\Phi/\Phi_0), \quad [\Phi, Q] = i\hbar. \quad (2.1)$$

The first term is completely analogous to the kinetic energy of a mechanical system $T = p^2/2m$ if we think of Q as the momentum and C as the mass. Similarly, we can think of Φ as the position of the particle in a cosine shaped potential energy with height E_J . Noting that in the mechanical case $[x, p] = i\hbar$ completes the analogy. The transmon is designed with a large C to make it insensitive to charge noise. This, being equivalent to a large mass, prevents the wave function from tunneling between the minima of the cosine potential. As a result, we can consider only a single minimum, as indicated by the solid line part of the potential in Fig. 2.5 a.

In practice the single junction is replaced by a pair of junctions in a loop, as illustrated in Fig. 2.5 b. This allows the resonance frequency of the transmon to be modulated dynamically. The loop acts like a single junction, but with a critical current I_c which depends on external flux threading the loop. Because the inductance of a junction is related to the critical current by $L_J = L_{J_0}/\sqrt{1 - (I/I_c)^2}$, we can control the inductance, and therefore the resonance frequency ω_0 of the circuit, via the external flux. Another way to think about this is that the external flux changes the effective E_J of the two-junction loop, thus changing the height of the cosine potential, as illustrated in Fig. 2.5 b. This change in the shape of the potential causes the energy difference between the states to change, thus changing their resonance frequency.

The transmon is particularly difficult to measure. Like the flux qubit the wave functions are broad in the charge basis, so the states cannot be distinguished via charge detection. On the other hand, because of the symmetric shape of the potential the states all have the same mean flux. Therefore, charge-based and flux-based measurements are both impossible.

2.3.1 Qubit as a photo-detector

One measurement strategy is to transfer the transmon state into a different kind of qubit where charge or flux measurement is available. This idea, which is essentially using a qubit as a microwave photon detector, is illustrated in Fig. 2.6. The measurement process is turned on by  dynamically tuning the transmon into resonance with the detector, in this case a phase qubit. If there is a quantum of energy in the transmon, then when the transmon comes on resonance with the phase qubit, the photon begins to oscillate between the two qubits. Once the photon is completely swapped into the phase qubit, the transmon is taken off resonance to stop the interaction. The phase qubit is then measured in the normal way. If the phase qubit is measured to be in the excited state, then

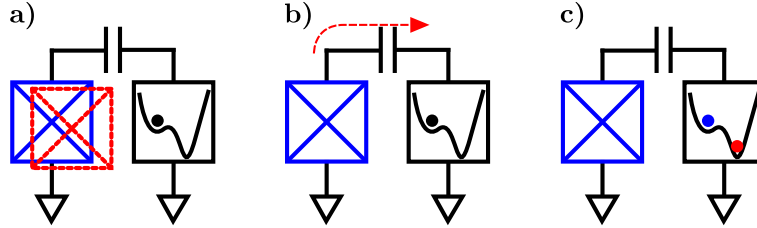


Figure 2.6: Qubit measurement by swapping the excitation into an auxiliary circuit. (a) The qubit starts in a superposition of the ground (blue) and excited (red) states. (b) The qubit is brought on resonance with the detector. If it was in the excited state, one quantum of energy is swapped into the detector, otherwise nothing happens. In either case, the qubit is left in the ground state. (c) The qubit is brought off resonance with the detector to turn the interaction off. The detector is now in one of two measurably different states corresponding to the two possible qubit states.

there must have been a photon collected from the transmon and so the initial state of the transmon is inferred by the measured state of the phase qubit.

This strategy does work, and in fact was used in the initial transmon experiments at UCSB [2]. However, it inherits all of the problems already mentioned with phase qubit measurement, most importantly the long dead time needed to reset the phase qubit.

2.3.2 Energy measurement with travelling waves

We consider briefly the notion of directly measuring the qubit energy, as it will shed light on the subsequent discussion. Suppose we allow the qubit energy to leak out from the qubit into an amplifier as a travelling wave, using a circuit as shown in Fig. 2.7 a. The qubit state would then be determined by measuring the amplitude of the wave after the amplifier by conventional means. Crucially, many qubits could be attached in parallel to the same transmission line and amplifier with the various output signals discriminated via frequency multiplexing. The problem with this solution is that the signal to noise ratio is fundamentally limited to near unity. The theoretical limit on the input referred noise power of a phase preserving linear amplifier is $P_N = (1/2)\hbar\omega B$ where B is the amplifier bandwidth [9].⁴ For a measurement of duration T , the collected noise energy would be $E_N = P_N T = (1/2)\hbar\omega B T$. To measure a pulse of length T the amplifier bandwidth must satisfy $B \gtrsim 1/T$, so $E_N \gtrsim (1/2)\hbar\omega$. This is already half as large as the maximum energy that could be collected from the qubit in a system with perfect efficiency. Therefore, the signal to noise ratio fundamentally cannot exceed 2, which is too low. The intrinsic suitability of this circuit for scaling to larger numbers of qubits suggests we find a way to fix the signal to noise ratio problem.

⁴We consider linear amplifiers because we want frequency multiplexing.

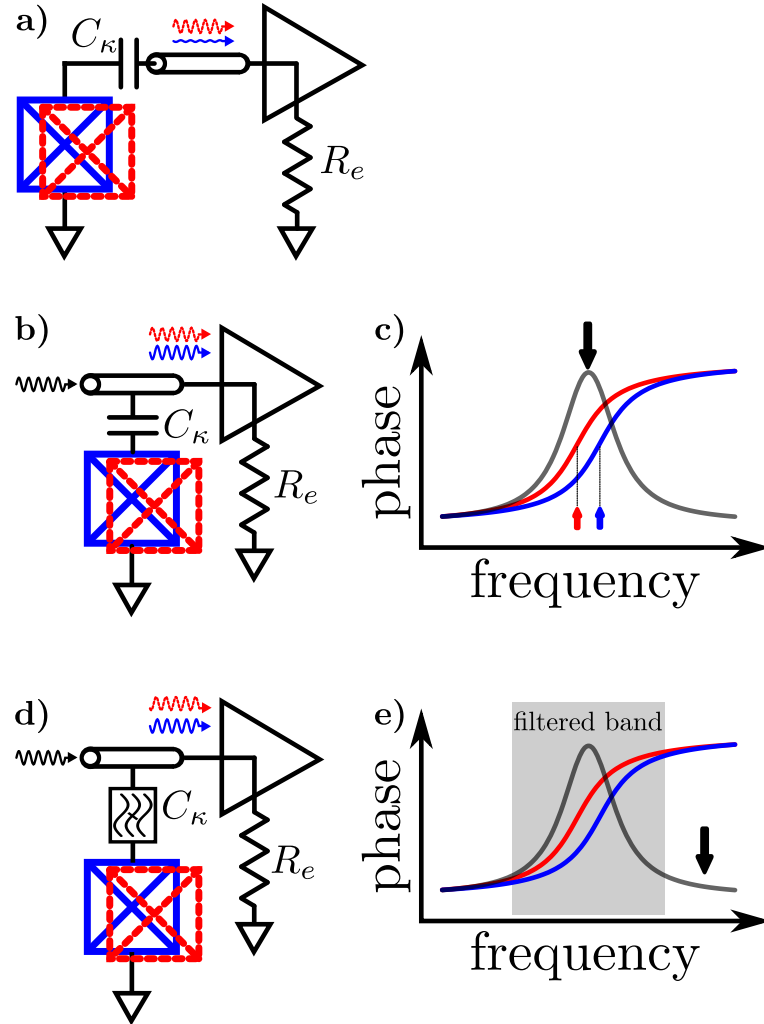


Figure 2.7: Measurement based on traveling waves. a) The qubit state is determined by the presence or absence of an outgoing wave. As the maximum measured energy is just the single photon in the qubit, the signal to noise ratio is too low. b,c) An externally supplied voltage is used to raise the signal to noise ratio. The wave acquires a qubit state dependent phase shift as it scatters from the shunt line containing the qubit. The blue and red curves indicate the phase response for the qubit in $|0\rangle$ and $|1\rangle$, respectively. The gray curve indicates the difference in these phases. The center frequencies of the qubit in the ground and excited states are indicated by the blue and red arrows, and the frequency yielding the maximum phase signal is indicated by the black arrow. d,e) A filter placed between the qubit and external resistance could raise the limit on qubit lifetime, but this leads to a smaller detectable phase shift.

2.3.3 Dispersive measurement

As we can measure neither the charge, flux, nor energy, we need to find another parameter of the qubit that differs between the two states. Because the qubit is non-linear its resonance characteristics depend on its energy state. This suggests that a spectroscopic measurement might be possible. Think of the qubit as a simple harmonic oscillator, but whose resonance frequency depends on whether it is in $|0\rangle$ or $|1\rangle$. As a probe signal applied to the circuit is swept in frequency, the phase shift acquired by that signal undergoes a sharp change across the resonance. As this resonance frequency depends on the qubit state, we can use the position of the phase shift to measure the qubit. A circuit diagram suitable for this measurement is shown in Fig. 2.7 b. The probe signal is injected into the left side of the transmission line. As it travels past the qubit and drives the qubit resonance, it picks up a phase shift which depends on the qubit state. The phase responses for the two states are plotted in Fig. 2.7 c. By probing at a frequency between the two possible qubit resonances, the phase shift difference is maximized and the qubit state could be determined.

This strategy solves the signal to noise ratio problem because the energy of the injected wave can be arbitrarily large. However, we have a coherence problem because the resistance in the external circuitry loads the qubit. In fact, the qubit lifetime imposed by this external circuitry is equal to the time it takes for the qubit to respond to the probe pulse and react with a phase shift. This means that the qubit life time during the measurement cannot significantly exceed the measurement time.

We could try to isolate the qubit from the damping of the external circuit with a filter, as illustrated in Fig. 2.7 d. The filter decouples the qubit circuit from the external circuit over a frequency range including the qubit resonance, so the qubit is not damped. However, the filter also decouples our probe signal from the qubit in that frequency band, so we would have to probe outside the band blocked by the filter. Far from the qubit resonance, the phase acquired by the probe signal is insensitive to the qubit state, as shown in Fig. 2.7 e, so the states are not well discriminated.

To isolate the qubit from damping while still allowing the probe signal to acquire a state dependent phase shift, we replace the filter in Fig 2.7 d with an auxiliary harmonic resonator, as shown in Fig. 2.8 a. The resonator frequency ω_r is detuned from the qubit by a frequency Δ . Therefore, *at the qubit frequency* the resonator is a short to ground and prevents the qubit from feeling the dissipation of the external circuitry. This blocks radiation from the qubit, and solves the coherence problem. As the qubit has different impedance in its two states, the loading it imparts on the resonator is state dependent, so the resonator frequency depends on the qubit state. We characterize the resonator frequency shift by a parameter χ , defined by $2\chi = \omega_{r,|0\rangle} - \omega_{r,|1\rangle}$, as shown in Fig. 2.8 b. We infer the qubit state by probing the system in between the two resonator frequencies and measuring the phase.

The physics of the qubit state-dependent resonator frequency shift was first demonstrated in 2004 and 2005 at Yale with charge qubits [36, 43, 42], and the

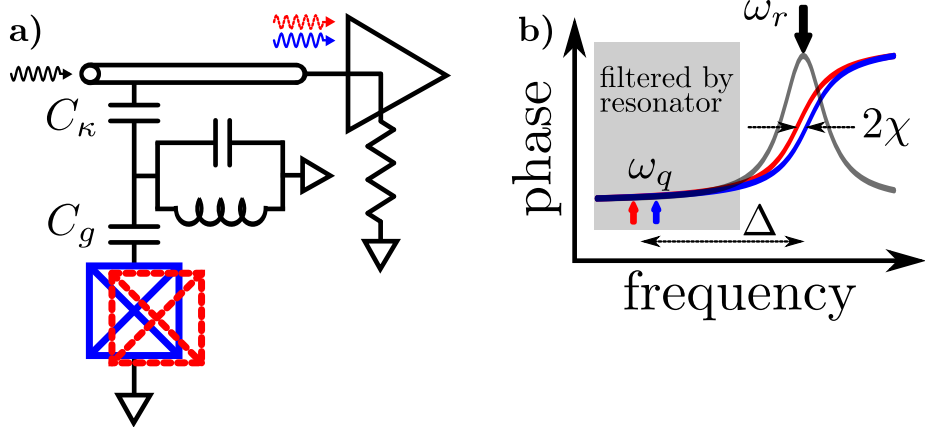


Figure 2.8: Schematic for measurement with an auxiliary resonator. a) The qubit is protected from resistance in the external circuitry by a detuned resonator which acts as a short at the qubit frequency. b) The qubit states cause the resonator frequency to shift, leading to large measureable phase shift at the resonator frequency.

shift was first used to measure qubit states in those experiments. This strategy has been named “dispersive measurement” or “dispersive readout” because it depends on the qubit state dependent dispersion of the probe signal. Using bifurcation amplifiers, dispersive measurement was shown in 2009 to yield measurement with accuracy up to 94% [17], and later experiments with transmon qubits using linear Josephson parametric amplifiers achieved accuracy up to about 94% [13].

The dispersive measurement strategy does have an important limitation. We said above that the resonator blocks the qubit from feeling the dissipation of the external circuitry, but this is true only up to a point. Even far off resonance, the resonator is not a perfect short, so the qubit is still damped to some degree. This effect is quantified by a relation between four parameters. First, we have the limit on qubit lifetime T_1 imposed by the measurement circuit. Second, we have the resonator-transmission line coupling strength characterized by the inverse ring-up time κ_r . This is set by C_κ , as shown in Fig. 2.8. Next is the the resonator-qubit coupling strength g , which is set by C_g , as shown in Fig. 2.8. Finally, we have the qubit-resonator detuning Δ . These parameters are related by [6]

$$\kappa_r T_1 \lesssim \left(\frac{\Delta}{g} \right)^2. \quad (2.2)$$

This formula expresses a tension between fast response time of the resonator κ_r and long coherence time of the qubit T_1 . For a given Δ and g , speeding up the measurement with faster κ_r leads to lower T_1 of the qubit. It turns out that to

get a large measurable phase shift, there is an additional constraint

$$\kappa_r \approx \chi = \frac{g^2}{\Delta} \quad (2.3)$$

which comes from the fact that, because the resonator is attached in parallel with the transmission line, the phase response measured in the circuit shown in Fig. 2.8 a is not actually the pure arc tangent shown in Fig. 2.8 b. Combining equations (2.2) and (2.3) yields

$$\kappa_r^2 T_1 \lesssim \Delta. \quad (2.4)$$

Suppose we have a qubit with an intrinsic energy decay time of T_1 . For 99% accurate measurement we need the entire measurement procedure to be shorter than $T_1/100$. Taking the entire measurement sequence to require a time of $10\kappa_r^{-1}$, this means we need $\kappa_r^{-1} \geq T_1/1000$. With currently available transmons at $T_1 \approx 20 - 40 \mu\text{s}$, this gives $\kappa_r^{-1} \sim 30 \text{ ns}$ and therefore requires $\Delta > \kappa_r^2 T_1 = 30 \text{ GHz}$. This large of a qubit-resonator detuning is completely impractical. With the qubit at $\sim 6 \text{ GHz}$, such a large Δ would put the resonator at such a high frequency that practical microwave engineering becomes much more difficult. For example, parasitic resonances on the micro-fabricated qubit chips become a serious problem when the signal wavelength becomes smaller than the size of the chip. A frequency of 30 GHz corresponds to a wavelength of 1 cm in vacuum (substantially less in a dielectric substrate) which is on the order of practical chip sizes. Another strategy is needed.

2.3.4 Filters

In 2010, researchers at Yale introduced the idea of on-chip filters to further protect the qubit from damping induced by environment [28]. The circuit is shown in Fig. 2.9 a. In this system the resonator is constructed from a $\lambda/2$ piece of co-planar wave guide inserted in series with the drive line. The qubit is connected in parallel with the resonator, and the filter is placed on the output of the resonator. This filter forms a notch at which energy cannot leave the resonator. By placing this notch at the qubit frequency, the qubit is protected from emitting energy. In Ref. [28], it was shown that for a given Δ , κ_r , and g , the filter increased the qubit T_1 above the limit from Eq. (2.2). However, that work did not discuss the all important speed and accuracy of the measurement.

Introduction of on-chip filters was a big step forward for measurement of superconducting qubits, because it opened the door for high speed and high accuracy measurement in transmons. However, the system used in Ref. [28] is not really suitable for experiments with multiple qubits. Because the resonator is in series with the drive line, there is no obvious way to include more than one resonator. This means that all qubits must be connected to the same resonator. In fact, experiments at Yale did use multiple qubits connected to a single resonator (although with no filter), and actually relied on this as the means by which they coupled the qubits together. However, this complicates measurement in a larger system. With N qubits connected to one resonator, unique

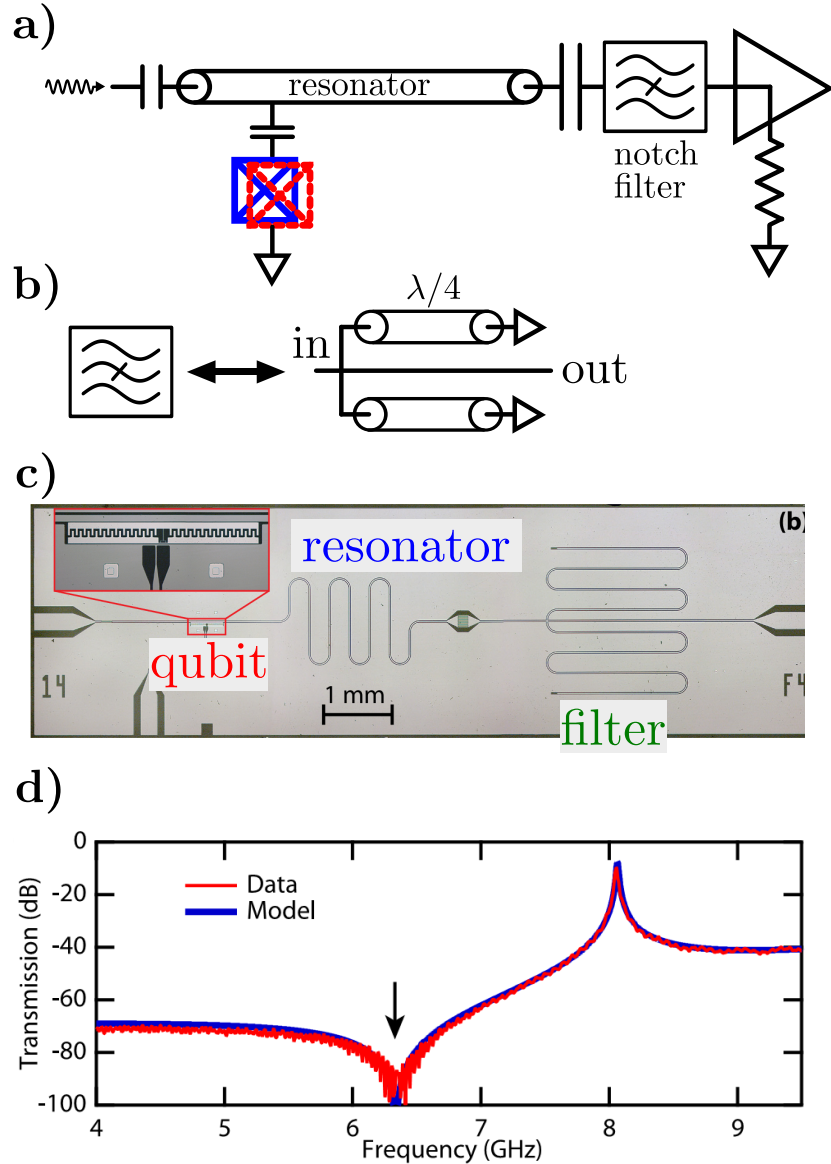


Figure 2.9: A filter used to increase the $\kappa_r T_1$ product. a) The filter is placed on the output of the resonator to prevent radiation at the qubit frequency from leaving the system. b) The filter was implemented as a symmetric pair of $\lambda/4$ stubs to ground. c) Micrograph of the Yale device. The filter is seen on the right side as two meandering co-planar wave guide resonators. d) Transmission through the system. Note the notch just above 6 GHz, which protects the qubit. The large increase in transmission at 8 GHz is the resonance frequency of the resonator.

identification of all of the possible qubit states would require us to distinguish 2^N different dispersed phases. This is a really hard problem and has never been demonstrated to work. Furthermore, the notch filter itself is not easily adapted to a multi-qubit system. The notch protects only one qubit, and is incompatible with dynamic frequency tuning of the qubits which is an essential ingredient for high accuracy logic gates [3].

This leaves us with two obvious next steps. First, we must find a filter architecture which is compatible with a multi qubit system. Second, we must study the speed and accuracy of dispersive measurement in the filtered system. Those tasks were the main objectives of the work in this thesis.

Chapter 3

Dispersive Measurement

3.1 Introduction

In the previous chapter we found, through historical survey and qualitative discussion, that dispersive measurement allows multiplexed qubit measurement while partially preserving the qubit coherence. In this chapter we analyze dispersive measurement in full quantitative detail.

In dispersive measurement, where a qubit coupled is coupled off resonance to a linear resonator, the resonator's frequency depends on the qubit's quantum state. Therefore, the qubit state is measured by probing the resonance frequency of the resonator. The analysis comes naturally in two steps. First, we develop the Hamiltonian for a qubit coupled to a resonator with large qubit-resonator detuning. From the Hamiltonian we find an equation relating the resonator frequency shift in terms of other parameters in the system, such as the qubit-resonator coupling strength and detuning. Second, we analyze the classical problem of measuring the resonator's resonance frequency through microwave scattering. Combined, these analyses show how the scattered microwave signal carries the information of the qubit state. At the end we present additional details of the dispersive measurement circuit which come into play in a practical lab setting where amplifier saturation is an important limitation.

3.2 Dispersive Hamiltonian

In this section we analyze the Hamiltonian of a qubit coupled to a linear resonator. We work in the limit where the difference Δ between the qubit and resonator frequencies is large compared to the strength of the qubit-resonator coupling g , as this is the limit in which the resonator protects the qubit T_1 .

A detailed derivation of the Hamiltonian for a resonant circuit, starting from first principles, is given in Ref. [33]. There we derive the Hamiltonian H_r for a

harmonic oscillator, and H_q for a qubit, finding

$$H_r/\hbar = \omega_r a^\dagger a \quad (3.1)$$

$$H_q/\hbar = -\omega_q (\sigma_z/2). \quad (3.2)$$

In these equations, ω_r is the resonance frequency of the resonator and ω_q is the $|0\rangle \rightarrow |1\rangle$ transition frequency of the qubit. The operators a^\dagger and a are the normal raising and lowering operators for the harmonic oscillator, and σ_z is the Pauli matrix represented as

$$\sigma_z = \begin{pmatrix} 1 & 0 \\ 0 & -1 \end{pmatrix} \quad (3.3)$$

where the qubit basis states are ordered $\{|0\rangle, |1\rangle\}$. In Ref. [57], we also derive the interaction Hamiltonian H_I which comes from the coupling between two circuits, finding

$$H_I/\hbar = g\sigma_y(-i)(a - a^\dagger). \quad (3.4)$$

where g is the coupling strength in dimensions of frequency. We expand σ_y in terms of spin raising and lowering operators,

$$\sigma_+ = \begin{pmatrix} 0 & 0 \\ 1 & 0 \end{pmatrix} \quad \sigma_- = \begin{pmatrix} 0 & 1 \\ 0 & 0 \end{pmatrix} \quad (3.5)$$

finding

$$\sigma_y = i(\sigma_+ - \sigma_-). \quad (3.6)$$

Using this form, we find

$$H_I/\hbar = g(\sigma_+a + \sigma_-a^\dagger - \sigma_+a^\dagger - \sigma_-a). \quad (3.7)$$

The second and third terms in parentheses do not conserve excitation number and are discarded.¹ We are left with

$$H_I/\hbar = g(\sigma_+a + \sigma_-a^\dagger). \quad (3.8)$$

Combining the three parts of the Hamiltonian, we find the Hamiltonian of the complete system

$$H/\hbar = (H_r + H_q + H_I)/\hbar = \omega_r a^\dagger a - \frac{\omega_q}{2}\sigma_z + g(\sigma_+a + \sigma_-a^\dagger). \quad (3.9)$$

The interaction can be simplified with a change of basis. We rotate the Hamiltonian by the unitary operator

$$U = \exp[\lambda T] \quad (3.10)$$

¹Discarding these terms is rigorously justified in the rotating frame where they acquire time evolution which is fast compared to the other terms.

where $\lambda \equiv -g/\Delta$ and $T \equiv \sigma_+a - \sigma_-a^\dagger$. In the dispersive measurement system, $\Delta \gg g$, so λ is a small dimensionless parameter. As such, we use it as an expansion parameter. Using the transformation operator U and a series expansion from Ref. [31] we can write

$$U^\dagger H U = e^{-\lambda T} H e^{\lambda T} \quad (3.11)$$

$$= H - \lambda [T, H] + \frac{\lambda^2}{2} [T, [T, H]] + \dots, \quad (3.12)$$

which is a power series in λ . We compute the relevant commutators in Eq. (3.12) with standard methods (see Ref. [31] for useful tricks). Some useful intermediate steps are

$$[T, n] = \sigma_+a + \sigma_-a^\dagger \quad (3.13)$$

$$[T, \sigma_z] = 2(\sigma_+a + \sigma_-a^\dagger) \quad (3.14)$$

$$[T, \sigma_-a^\dagger + \sigma_+a] = 2(\sigma_+\sigma_- - \sigma_zn). \quad (3.15)$$

Evaluating Eq. (3.12) to the second order in λ gives

$$\frac{U^\dagger H U}{\hbar} = \frac{H_q}{\hbar} + \frac{H_r}{\hbar} - \frac{g^2}{\Delta}\sigma_zn \quad (3.16)$$

which can be interpreted as

$$H_I/\hbar \longrightarrow -\frac{g^2}{\Delta}\sigma_zn = -\chi\sigma_zn \quad (3.17)$$

where $\chi \equiv g^2/\Delta$ is the so-called dispersive shift.

We interpret the dispersive shift χ in two different ways. Writing the system Hamiltonian as

$$H/\hbar = (\omega_r - \chi\sigma_z)n - \frac{\omega_q}{2}\sigma_z, \quad (3.18)$$

the dispersive shift appears as a qubit state dependent shift of the resonator frequency. The difference in resonator frequency for the two qubit states is 2χ . However, regrouping the terms as

$$H/\hbar = \omega_rn - \frac{\omega_q + 2\chi n}{2}\sigma_z \quad (3.19)$$

the dispersive shift appears as a resonator photon number dependent shift of the qubit frequency. In the latter case we refer to the shift as the “ac Stark effect” [43, 36].

In the preceding analysis we assumed that the qubit had only two levels. In practice, superconducting qubits have additional levels. Reference [15] find that taking the third level of the qubit into account modifies the expression for χ , yielding

$$\chi = \frac{g^2}{\Delta} \frac{1}{1 + \Delta/\eta} \quad (3.20)$$

where $\eta \equiv \omega_{21} - \omega_{10}$ is the anharmonicity of the qubit ($\eta < 0$ for a transmon). In the practical limit of $\Delta \gg \eta$, we find

$$\chi = \frac{g^2}{\Delta^2} \eta. \quad (3.21)$$

Note that $\chi \rightarrow 0$ as $\eta \rightarrow 0$, as expected for coupling of two harmonic oscillators.

3.3 Scattering

Now that we have shown that the qubit state induces a frequency shift on the resonator, it remains to show how we measure that frequency shift. In this part of the calculation we omit the qubit, taking its effect on the system into account through the resonator frequency shift. Therefore, this calculation is classical, with the quantum effect of the qubit encapsulated in the parameter χ calculated in the previous section.

We consider a resonator connected in parallel to a transmission line, as shown in Fig. 3.1. A resonator with impedance Z_r and frequency ω_r is connected in parallel through a capacitor C_κ to a transmission line. We model the resonator as a parallel LC circuit with resonance frequency $\omega_{LC} = 1/\sqrt{LC}$, internal quality factor Q_i and characteristic impedance $Z_{LC} = \sqrt{L/C}$. The shunt impedance is $Z_{in} = Z_\kappa + Z_r$ where $Z_\kappa = 1/i\omega C_\kappa$ is the impedance of the coupling capacitor, and $Z_r = Z_{LC} Q_i / (1 + iQ_i(x - 1/x))$ with $x \equiv \omega/\omega_{LC}$ is the impedance of the resonator. The shunt circuit interrupts the transmission line, creating a scattering site for traveling microwave signals in the line. A voltage wave injected into the input port with amplitude V_{in} scatters from the shunt circuit. Part of the wave reflects with amplitude $V_{in} S_{11}$ and part is transmitted with amplitude $V_{out} = V_{in} S_{21}$. In the following analysis, we show how, by measuring the amplitude and phase of the scattered signal, we can infer the resonator frequency of the resonator, and thus the state of the qubit.

The scattering parameters S_{ij} for a transmission line interrupted by a shunt circuit with admittance $Y = 1/Z_{in}$, as shown in Fig. 3.1, are [26]

$$S_{11} = \frac{-\bar{Y}}{2 + \bar{Y}} \quad (3.22)$$

$$S_{21} = \frac{2}{2 + \bar{Y}}, \quad (3.23)$$

where $\bar{Y} \equiv Z_0 Y$ and Z_0 is the characteristic impedance of the transmission line. From these equations we can solve for S_{11} in terms of S_{21} ,

$$S_{11} = S_{21} - 1. \quad (3.24)$$

The qubit state measurement is based on the fact that the output voltage wave amplitude depends on the properties, namely Q and ω_r , of the resonator. To describe this we must compute S_{21} in terms of probe frequency and the

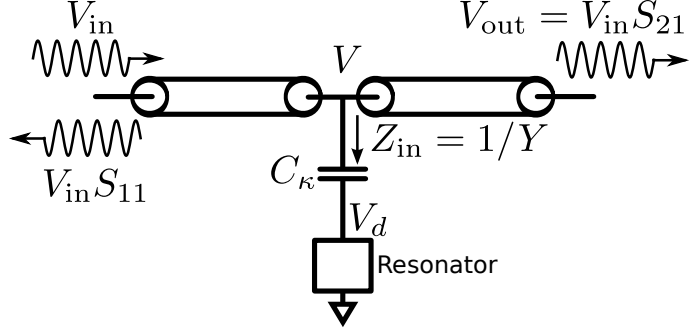


Figure 3.1: A transmission line shunted by a resonant circuit. In incoming voltage wave is partially reflected and partially transmitted by the impedance mismatch at the point where the resonator is coupled to the transmission line.

resonator parameters. Using Eq. (3.23) it can be shown that

$$S_{21} = \frac{S_{\min} + 2iQ_l\delta y}{1 + 2iQ_l\delta y} \quad (3.25)$$

$$\text{Re}S_{21} = \frac{S_{\min} + (2Q_l\delta y)^2}{1 + (2Q_l\delta y)^2} \quad (3.26)$$

$$\text{Im}S_{21} = \frac{2Q_l\delta y(1 - S_{\min})}{1 + (2Q_l\delta y)^2}, \quad (3.27)$$

where $Q_l^{-1} = Q_i^{-1} + Q_c^{-1}$, Q_c is the coupled Q of the resonator, $S_{\min} = Q_c/(Q_c + Q_i)$, and $\delta y \equiv (\omega - \omega_r)/\omega_r$ where ω_r is the resonance frequency²³. A result that will be useful later is that the imaginary part of S_{21} is extremal for $\delta y = \pm 1/2Q_l$.

The inverse transmission amplitude is a very useful quantity

$$S_{21}^{-1} = 1 + e^{i\phi} \frac{Q_i}{Q_c} \frac{1}{1 + 2iQ_i\delta y} \quad (3.28)$$

This equation comes from inverting the usual expression for S_{21} and adding a phase factor in the second term to account for possible impedance mismatches between the input and output [19]. The diameter of the circle is

$$D = 1 - S_{\min}. \quad (3.29)$$

Another useful relation is the detuning as a function of the measure transmission amplitude

$$\delta x = \frac{1}{2iQ_i} \left[e^{i\phi} \frac{Q_i}{Q_c} (S_{21}^{-1} - 1)^{-1} - 1 \right]. \quad (3.30)$$

²The frequency ω_r is near to the resonator bare resonance but slightly detuned due to the coupling capacitor and line impedance.

³See pages 114 and 115 of Dan's notebook no. 5 for details, and also Ben Mazin's thesis.

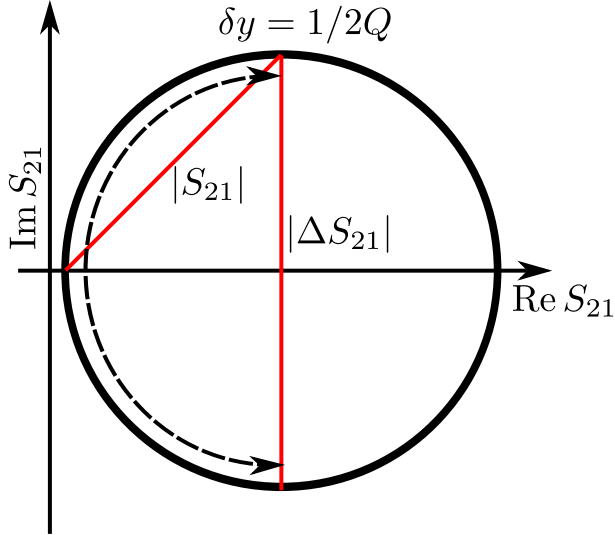


Figure 3.2: Scattering diagram for shunt resonator

3.4 Qubit measurement

Dispersive qubit measurement is based on the quantum effect that the resonator frequency depends on the qubit state. Here we assume the resonator has one of two frequencies, and explain how a classical probe signal distinguishes between those two frequencies. Let the two resonator frequencies corresponding to the qubit $|0\rangle$ and $|1\rangle$ states be denoted $\omega_{r,|0\rangle}$ and $\omega_{r,|1\rangle}$. In the previous section we calculated that these frequencies differ by $\omega_{r,|0\rangle} - \omega_{r,|1\rangle} = 2\chi$. If we probe the system at $\omega_{\text{probe}} = (\omega_{r,|0\rangle} + \omega_{r,|1\rangle})/2$, ie. between the two possible frequencies, the two possible values of S_{21} are given by Eq. (3.25) with $\delta y = \pm\chi$. In order to get the maximum visibility in the dispersed probe signal, we must choose parameters so that $S_{21}(\pm\chi)$ are at diametrically opposed points on the circle in Fig. 3.2. The top and bottom points (ie. those for which the imaginary part are extremized) are the diametrically opposed points requiring the smallest frequency separation. As noted previously, these points occur for $\delta y = \pm 1/2Q_l$ so the criterion for maximum visibility is

$$\chi = \frac{\omega_r}{2Q_l} = \frac{\kappa_r}{2}. \quad (3.31)$$

3.5 Fresnel lollipops - separation error

The phase and amplitude of the scattered signal are extracted using traditional signal processing techniques. The end result is a single value in the two dimensional IQ plane. In the absence of noise, the two possible qubit states

would correspond to two individual IQ points as indicated by the black dots in Fig. 3.3. In this case, any nonzero separation between the points would allow distinction between the qubit states. However, in the real system, both technical and quantum noise add statistical fluctuations to the extracted IQ points. The “quantum noise” is just the intrinsic width of the wave functions of the coherent microwave pulse, which carries a noise power of $\hbar\omega/2$ per unit bandwidth. A minimum additional $\hbar\omega/2$ of quantum noise is added by a phase preserving parametric amplifier [9]. Technical noise may be added by following amplifiers, such as a HEMT. Signal loss prior to the dominant amplifier stages also appears as effective added noise.

The time domain noise leads to noise in the demodulated IQ points. Instead of single points corresponding to the two qubit states, we get two dimensional Gaussian statistical distributions, as shown by the blue and red clouds in Fig. 3.3 [35, 34]. These clouds have been called “Fresnel lollipops”. Projecting the lollipops onto a line separating their centers produces a pair of one dimensional Gaussian curves. Choosing the center of the curves as the discrimination between $|0\rangle$ and $|1\rangle$, we can see that, because of the finite width σ of the curves, there will always be a nonzero probability of misidentifying the qubit state. We call this error, due to the finite separation of the curves, the “separation error”, denoted ϵ_{sep} . The separation error is computed by integrating the weight of one of the Gaussian distributions which is on the “wrong” side of the discrimination point,

$$\begin{aligned}\epsilon_{\text{sep}} &= \frac{1}{\sqrt{2\pi\sigma^2}} \int_{x=(x_0-x_1)/2}^{\infty} e^{-\frac{(x-x_0)^2}{2\sigma^2}} dx \\ &= \frac{1}{2} \operatorname{erfc} \left[\frac{|x_0 - x_1|}{2\sqrt{2}\sigma} \right],\end{aligned}\quad (3.32)$$

where the erfc function is defined as

$$\operatorname{erfc}(z) \equiv 1 - \frac{2}{\sqrt{\pi}} \int_0^z e^{-x^2} dx. \quad (3.33)$$

Defining the signal to noise ratio (SNR) of the measurement as

$$\text{SNR} \equiv \frac{(x_0 - x_1)^2}{2\sigma^2}, \quad (3.34)$$

we relate ϵ_{sep} to the SNR,

$$\epsilon_{\text{sep}} = \frac{1}{2} \operatorname{erfc} \left[\frac{\sqrt{\text{SNR}}}{2} \right]. \quad (3.35)$$

3.6 Measurement induced dephasing

As photons enter the resonator and acquire a qubit state dependent phase shift, they carry some information on the qubit state. By transferring quantum information from the qubit to the photons, the measurement process partially

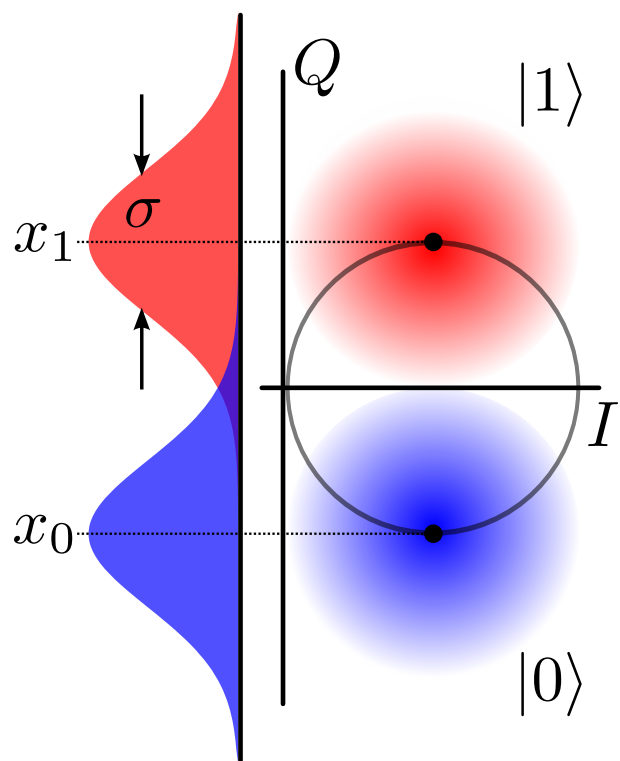


Figure 3.3: IQ clouds for the qubit states measured in the presence of noise. The clouds for $|0\rangle$ (blue) and $|1\rangle$ (red) are centered on the diametrically opposite points of the S_{21} circle. The black dots represent the points which would be found in the absence of all noise sources. The Gaussian curves show projections of the clouds onto the line connecting their centers.

collapses the qubit state [21]. In dispersive measurement, the photon's phase shift carries information about the qubit project along the z-axis of the Bloch sphere. Therefore, the partial collapse induced by the scattered photons can be understood as qubit dephasing. The dephasing is only partial because the state of the qubit cannot be unambiguously determined from a single scattered photon, as will become clear shortly.

In the following, we derive a relation between the measurement visibility and the qubit dephasing induced by the measurement process. The derivation is very general, and not constrained to a particular qubit system or measurement strategy.

The phase coherence of a state of a 2-level system is described by the off-diagonal terms in the density matrix, ρ_{10} and ρ_{01} . The diagonal terms ρ_{00} and ρ_{11} are just the probabilities $P(0)$ and $P(1)$ that the qubit is in $|0\rangle$ or $|1\rangle$, respectively. From the general construction of a density matrix, it can be shown that

$$|\rho_{10}| \leq \sqrt{\rho_{00}\rho_{11}} = \sqrt{P(0)P(1)}. \quad (3.36)$$

We now investigate the right hand side of Eq. (3.36). Suppose we measure the qubit along the z-axis with a meter which yields a single real number with value x . To quantify the amount of information about the qubit state we have learned from this measurement result, we investigate the probability, given this result, that the qubit is in $|0\rangle$. Using Bayes's theorem, we can write

$$P(0|x) = \frac{P(x|0)P(0)}{P(x)}. \quad (3.37)$$

In English, Eq. (3.37) reads “The probability that the qubit is in $|0\rangle$ given that we measured x , is equal to the probability that we would measure x if the qubit were in $|0\rangle$, times the probability that the qubit is in $|0\rangle$, divided by the probability that we would measure x .” We write a similar equation for $P(1|x)$,

$$P(1|x) = \frac{P(x|1)P(1)}{P(x)}. \quad (3.38)$$

Suppose we are given a qubit in the state $(|0\rangle + |1\rangle)/\sqrt{2}$. Then $P(0) = P(1) = 1/2$. Combining these results we can rewrite the right hand side of Eq. (3.36) as

$$I(x) \equiv \sqrt{\frac{P(x|0)P(x|1)}{P(x)^2}} = \frac{\sqrt{P(x|0)P(x|1)}}{2P(x)}. \quad (3.39)$$

The coherence of the qubit is limited by the total information contained in the scattered photon. To recover this information, we must average over all possible detector values x ,

$$|\rho_{10}| \leq \int_{x=-\infty}^{\infty} I(x)P(x) dx = \int_{x=-\infty}^{\infty} \frac{1}{2} \sqrt{P(x|0)P(x|1)} dx. \quad (3.40)$$

In the dispersive measurement system with linear amplifiers, the measured voltages are Gaussian distributed, with the $|0\rangle$ and $|1\rangle$ having different means,

$$P(x|0) = \frac{1}{\sqrt{2\pi\sigma^2}} \exp\left[\frac{-(x-x_0)^2}{2\sigma^2}\right] \quad P(x|1) = \frac{1}{\sqrt{2\pi\sigma^2}} \exp\left[\frac{-(x-x_1)^2}{2\sigma^2}\right]. \quad (3.41)$$

Plugging these expressions into Eq. (3.40) yields

$$\begin{aligned} |\rho_{10}| &\leq \int_{x=-\infty}^{\infty} \frac{1}{2} \frac{1}{\sqrt{2\pi\sigma^2}} \exp\left[\frac{-(x-x_0)^2 - (x-x_1)^2}{4\sigma^2}\right] dx \\ &\leq \frac{1}{2} \exp\left[-\frac{(x_0-x_1)^2}{8\sigma^2}\right] \end{aligned} \quad (3.42)$$

$$\leq \frac{1}{2} \exp\left[-\frac{\text{SNR}}{4}\right]. \quad (3.43)$$

In the last line we used Eq. (3.34) for the definition of SNR. Equation (3.43) provides the quantitative link between the measurement SNR and qubit phase decoherence. As scattered photons are collected, the separation $x_0 - x_1$ increases and the upper bound on ρ_{10} decreases.⁴ In other words, increased visibility between the qubit states decreases phase coherence.

3.7 Resonator energy to output power ratio

In this section we derive an equation relating the energy in the measurement resonator to the power leaving the system. This is an important quantity as output power is a limited resource due to the finite saturation power of quantum limited amplifiers.

3.7.1 Resonator internal energy

Now that we have a formula for S_{21} in terms of the resonator properties we would like to relate it to the resonator's internal energy. To do this we must compute the voltage V_d at the resonator's driving node. This voltage can be found by voltage division; V_d is just V divided by the coupling capacitor and the resonator impedances,

$$V_d = V \frac{Z_r}{Z_\kappa + Z_r} = V \frac{Z_{\text{in}} - Z_\kappa}{Z_{\text{in}}}. \quad (3.44)$$

The voltage V at the shunt node is given by the sum of the incoming, reflected, and outgoing voltage amplitudes

$$V = V_{\text{in}} (1 + S_{11} + S_{21}). \quad (3.45)$$

⁴Or, if the data is normalized to a constant value of $x_0 - x_1$, the widths σ of the Gaussian curves decreases.

Using Eq. (3.24) this simplifies to

$$V = 2V_{\text{in}}S_{21}, \quad (3.46)$$

which finally yields

$$V_d = 2V_{\text{in}}S_{21} \frac{Z_{\text{in}} - Z_{\kappa}}{Z_{\text{in}}}. \quad (3.47)$$

The energy in the resonator is

$$E_{\text{res}} = \frac{1}{2}C|V_d|^2 = 2C|V_{\text{in}}S_{21}|^2 \left| \frac{Z_{\text{in}} - Z_{\kappa}}{Z_{\text{in}}} \right|^2 \quad (3.48)$$

3.7.2 Output power

The voltage wave amplitude travelling to the readout amplifier is by definition $V_{\text{in}}S_{21}$. The power going into the amplifier is therefore

$$P_{\text{out}} = \frac{1}{2}|V_{\text{in}}S_{21}|^2/Z_0. \quad (3.49)$$

3.7.3 Ratio

The ratio of resonator energy to output power is

$$\frac{E_{\text{res}}}{P_{\text{out}}} = 4Z_0C \left| 1 - \frac{Z_{\kappa}}{Z_{\text{in}}} \right|^2. \quad (3.50)$$

From Eq. (3.25) we can write $Z_0/Z_{\text{in}} = 2(S_{21}^{-1} - 1)$. Substituting this and using $C = 1/\omega_r Z_{LC}$ we get

$$\frac{E_{\text{res}}}{P_{\text{out}}} = \frac{4}{\omega_r} \frac{Z_0}{Z_{LC}} \left| 1 - \frac{2Z_{\kappa}}{Z_0} (S_{21}^{-1} - 1) \right|^2. \quad (3.51)$$

Equation (3.51) relates the resonator energy to the output power. However, as written it is not directly useful as it involves the impedance of the coupling capacitor Z_{κ} which is not an experimentally measurable parameter. We replace it with the coupling quality factor Q_c of the resonator via [30]

$$\frac{1}{C_{\kappa}} = \omega_r \sqrt{Q_c R_e Z_{LC}}, \quad (3.52)$$

where R_e is the resistance external to C_{κ} (in this case $Z_0/2$ because the input and output lines form parallel resistances). Substituting Eq. (3.52) into Eq. (3.51) we arrive at

$$\frac{E_{\text{res}}}{P_{\text{out}}} = \frac{4}{r_{LC}\omega_r} \left| 1 + i2\frac{\omega_r}{\omega} \sqrt{Q_c r_e r_{LC}} (S_{21}^{-1} - 1) \right|^2, \quad (3.53)$$

where we have defined r_{LC} and r_e by the equations $Z_{LC} \equiv r_{LC}Z_0$ and $R_e \equiv r_e Z_0$.

In the optimal visibility where $S_{21} \approx \frac{1}{2}(1 \pm i)$ we find

$$\begin{aligned}\frac{E_{\text{res}}}{P_{\text{out}}} &= \frac{4}{r_{LC}\omega_r} \left| 1 + i2\frac{\omega_r}{\omega} \sqrt{Q_c r_e r_{LC}} (\pm i) \right|^2 \\ &\approx 16 \frac{Q_c r_e}{\omega_r} \\ &\approx 16 \frac{r_e}{\kappa_r}\end{aligned}\tag{3.54}$$

where we've assumed $\omega \approx \omega_r$ and $Q_c \gg 1$. For comparison, a resonator in free ring-down has $E_{\text{res}}/P_{\text{out}} = 1/\kappa$. In the driven circuit studied here, for a given output power, the resonator internal energy is $16 r_e$ times larger than in the free ring-down case.

Chapter 4

Bandpass Filter

4.1 Analysis

4.1.1 Analytic treatment

In this section we derive an analytic expression for the $\kappa_r T_1$ product in the filtered measurement system. Starting from the definition of the quality factor for the qubit and relate it to the quality factor of the filter. We will find that the relation involves the ratio of the qubit and filter voltages, which we compute using voltage division. An alternative method is to compute the complex admittance Y_e presented to the qubit by the measurement circuit, and find the qubit T_1 using $T_1 = C_q/\text{Re}Y(\omega_q)$ [11]. The approach used here should give the reader a more intuitive understanding of how the filter works.

An equivalent lumped model for the circuit is shown in Fig. 4.1 a. We begin by writing down the definition of the quality factor of the qubit:

$$Q_q \equiv \frac{\text{energy stored in qubit}}{\text{energy lost per radian of qubit oscillation}}. \quad (4.1)$$

The energy lost per radian of oscillation can be re-expressed in terms of the qubit frequency and the power loss

$$\text{energy loss per radian} = \frac{dE}{d\text{rad}} = \frac{dE}{dt} \frac{dt}{d\text{rad}} = \frac{P}{\omega_q} \quad (4.2)$$

where P is the power loss and ω_q is the qubit oscillation frequency. Substituting Eq. (4.2) into Eq. (4.1) gives

$$Q_q = \frac{E_q \omega_q}{P} \quad (4.3)$$

where here E_q denotes the energy stored in the qubit.

If we assume that the circuit elements are lossless, then the only channel by which energy can leave the system is through the filter's coupling to the external

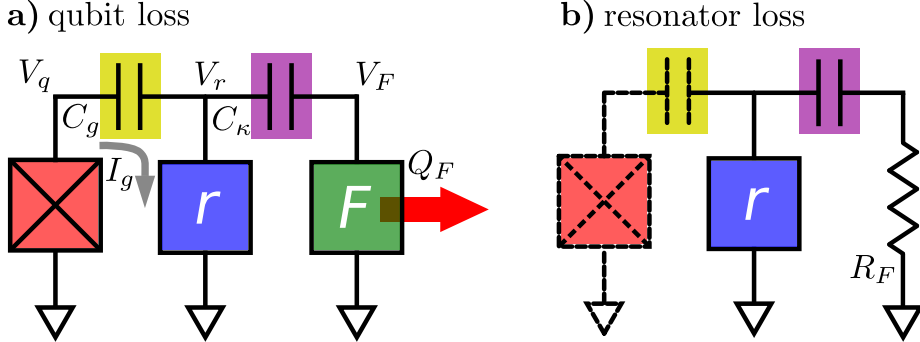


Figure 4.1: Lumped element model of the qubit and measurement circuit. a) The circuit is a ladder of alternating coupling capacitors and shunt resonators to ground. The only path by which energy can leave the system is through the finite internal quality factor Q_F of the filter, as indicated by the red arrow. At the qubit frequency, the impedance of the coupling capacitors is greater than the impedance of the resonators. This means that all of the current flowing through eg. C_g goes to ground through resonator r . b) To understand the quality factor of the resonator Q_r , we neglect the qubit which is assumed to be lossless. The damping of the resonator therefore comes entirely from the loss of the filter. Near resonance the filter impedance is a pure resistance.

measurement circuitry. The energy lost this way is characterized by the quality factor of the filter Q_F

$$Q_F \equiv \frac{\text{energy stored in filter}}{\text{energy lost per radian of filter oscillation}} = \frac{E_F \omega_F}{P} \quad (4.4)$$

where here the second equality follows from the same reasoning that lead to Eq. (4.3). Setting the power loss in Eq. (4.3) equal to the power loss in Eq. (4.4) gives

$$Q_q = Q_F \frac{E_q \omega_q}{E_F \omega_F} = Q_F \frac{\omega_q}{\omega_F} \frac{C_q}{C_F} \left| \frac{V_q}{V_F} \right|^2 \quad (4.5)$$

where we have taken $E_q = \frac{1}{2} C_q |V_q|^2$ and $E_F = \frac{1}{2} C_F |V_F|^2$, and V_q and V_F are the voltage amplitudes at the qubit and filter as shown in Fig. 4.1 a.

To compute the ratio V_q/V_F we use voltage division. The analysis is based on the crucial observation that to compute the damping of the qubit we must analyse the circuit *at the qubit frequency*. Because the qubit is off resonance from the measurement resonator and the coupling between the qubit and resonator is weak, the measurement resonator's impedance Z_r is lower than the impedance of the coupling capacitor, ie. $Z_r \ll Z_g$. By similar reasoning $Z_r \ll Z_\kappa$. Therefore, with voltage V_q across the qubit, we have a current $I_g = V_q/Z_g$ flowing through C_g (see Fig. 4.1 a) and most of that current goes to ground through the resonator. This gives $V_r = I_g Z_r = V_q Z_r / Z_g$. Using similar arguments to work through the

next stage of the circuit we arrive at

$$\frac{V_q}{V_F} = \frac{Z_g Z_\kappa}{Z_r Z_F}. \quad (4.6)$$

Note the shunt impedances in the denominator and the coupling impedances in the numerator.

Next we compute Z_r and Z_F in terms of their characteristic resonance impedances. The impedance of a lossless, parallel, single pole resonance is

$$\frac{1}{Z} = i\omega C + \frac{1}{i\omega L} = \frac{i}{Z^0} \frac{2\delta x + \delta x^2}{1 + \delta x} \approx \frac{i2\delta x}{Z^0} \quad (4.7)$$

where $\delta x \equiv (\omega - \omega_r)/\omega_r$, ω_r is the resonance frequency, and Z^0 is the characteristic impedance of the resonance ($Z^0 = \sqrt{L/C}$ for a parallel LC resonance). Inserting Eq. (4.7) into Eq. (4.6) we get

$$\left| \frac{V_q}{V_F} \right| = \frac{|Z_g| |Z_\kappa|}{Z_r^0 Z_F^0} \left(\frac{2\delta x + \delta x^2}{1 + \delta x} \right)^2 \quad (4.8)$$

where here $\delta_x \equiv (\omega_q - \omega_r)/\omega_r$, ω_r is the measurement resonator frequency, and we assume the measurement resonator is on resonance with the filter. Inserting Eq. (4.8) into Eq. (4.5) yields

$$Q_q = Q_F \frac{\omega_q}{\omega_r} \frac{C_q}{C_F} \left(\frac{|Z_g| |Z_\kappa|}{Z_r^0 Z_F^0} \right)^2 \left(\frac{2\delta x + \delta x^2}{1 + \delta x} \right)^4. \quad (4.9)$$

Equation (4.9) expresses Q_q in terms of the impedances of the couplers. While this can in principle be used as a design formula, it would be more convenient to replace the information contained in Z_κ with an expression involving Q_r . To do this we consider the circuit at measurement frequency. With the measurement resonator and filter assumed to be on resonance the filter impedance is nearly a pure resistance $R_F = Q_F Z_F^0$, as indicated in Fig. 4.1 b. As we assume the qubit is lossless, R_F sets Q_r . Following reasoning similar to what lead to Eq. (4.9) we find

$$Q_r = \frac{|Z_\kappa|^2}{R_F Z_r^0} = \frac{|Z_\kappa|^2}{Q_F Z_F^0 Z_r^0}. \quad (4.10)$$

Substituting Eq. (4.10) into Eq. (4.9) yields

$$Q_q = Q_r Q_F^2 \left(\frac{C_q}{C_g} \right)^2 \left(\frac{Z_q^0}{Z_r^0} \right) \left(\frac{2\delta x + \delta x^2}{1 + \delta_x} \right)^4 \quad (4.11)$$

and using $Q_r = \omega_r \kappa_r$ and $Q_q = \omega_q T_1$ we find

$$\kappa_r T_1 = Q_F^2 \left(\frac{\omega_r}{\omega_q} \right) \left(\frac{C_q}{C_g} \right)^2 \left(\frac{Z_q^0}{Z_r^0} \right) \left(\frac{2\delta x + \delta x^2}{1 + \delta_x} \right)^4. \quad (4.12)$$

Equation (4.12) is our basic result giving the $\kappa_r T_1$ product for a filtered measurement system. As it expresses the product in terms of hardware parameters it is most useful when choosing values for the actual hardware and for constructing numerical simulations in circuit modelling programs.

In practice the resonant circuits are implemented as distributed transmission line resonators. In this case it is convenient to eliminate the characteristic resonance impedances in favor of the characteristic impedance of the line. For a $\lambda/4$ transmission line resonator, the resonance Z^0 impedance is related to the line impedance Z_0 by

$$Z^0 = (4/\pi)Z_0 \quad (4.13)$$

which turns Eq. (4.12) into

$$\kappa_r T_1 = \frac{\pi}{4} Q_F^2 \left(\frac{\omega_r}{\omega_q} \right) \left(\frac{C_q}{C_g} \right)^2 \left(\frac{Z_q^0}{Z_0} \right) \left(\frac{2\delta x + \delta x^2}{1 + \delta x} \right)^4. \quad (4.14)$$

We used Eq. (4.14) as our design formula.

Equation (4.12) expresses $\kappa_r T_1$ in terms of circuit hardware parameters. For an equation expressed in terms of implementation-independent parameters, we need to eliminate C_g in favor of a coupling strength. The equation which does this is [33]

$$g_e = \frac{1}{2} \frac{C_g}{\sqrt{C_q C_r}} \hbar \sqrt{\omega_q \omega_r}. \quad (4.15)$$

The subscript e reminds us that this coupling strength has dimensions of energy. It is convenient to work with a coupling strength which has dimensions of (angular) frequency

$$g \equiv \frac{g_e}{\hbar} = \frac{1}{2} \frac{C_g}{\sqrt{C_q C_r}} \sqrt{\omega_q \omega_r}. \quad (4.16)$$

Using Eq. (4.16) and keeping the leading order in δx we can re-express Eq. (4.12) as

$$\kappa_r T_1 = \left(\frac{\Delta}{g} \right)^2 \left(\frac{\omega_r}{\omega_q} \right) \left(\frac{\Delta}{\omega_r/2Q_F} \right)^2 \quad (4.17)$$

where $\Delta \equiv \omega_q - \omega_r$. The first factor, $(\Delta/g)^2$ is the $\kappa_r T_1$ product for a single pole (ie. no filter) system. The second factor is of order one. The final factor is understood as the isolation provided by the filter: $\omega_r/2Q_F$ is the half width at half max of the filter (recall that we assume $\omega_r = \omega_F$), so $\Delta/(\omega_r/2Q_F)$ is the qubit-filter detuning in units of half-widths. This factor substantially raises the $\kappa_r T_1$ product. For $\omega_q = 6$ GHz, $\omega_r = 7$ GHz, and $Q_F = 30$ we find

$$\left(\frac{\omega_r}{\omega_q} \right) \left(\frac{\Delta}{\omega_r/2Q_F} \right)^2 = 85, \quad (4.18)$$

almost two orders of magnitude improvement over the un-filtered case.

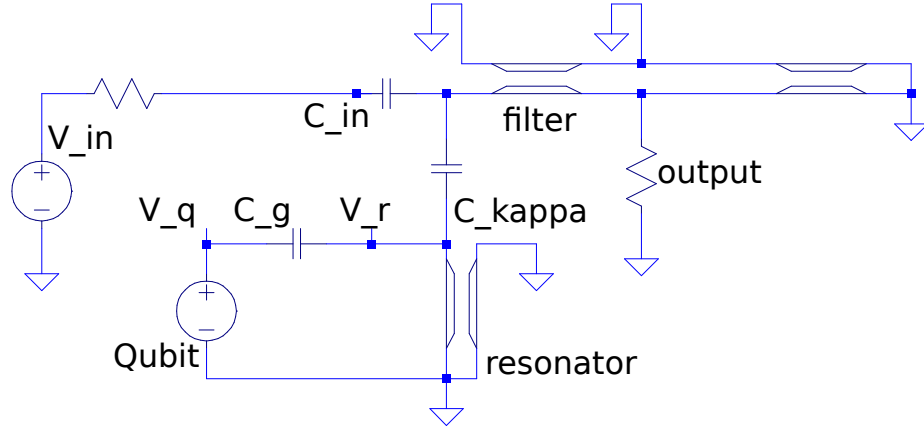


Figure 4.2: Screen capture of the SPICE model. The qubit is replaced by a voltage source which is activated with an ac signal of amplitude V_s at variable frequency ω . The current I_s through the source is probed and the admittance of the external circuit computed as $Y_e(\omega) = I_s/V_s$.

4.1.2 Numeric treatment

To verify the analysis we compared Eq. (4.14) against numerical simulation of the measurement circuit using the LTSPICE¹ circuit simulation package. Figure 4.2 shows a diagram of the model. We determine the quality factor of the qubit Q_q in two steps. First we replace the qubit with a voltage source V_s at frequency ω and probe the resulting current I_s . The ratio I_s/V_s is the admittance $Y_e(\omega)$ of the external measurement circuitry as seen by the qubit. We then use the fact that, for the transmon qubit, the matrix elements are nearly those of a harmonic oscillator. For a harmonic system, the coherent states are eigenvectors of the annihilation operator a , so loss processes are always in the correspondence limit. We can therefore compute the damping of the qubit using the classical equation [11]

$$Q_q = \omega C_q / \text{Re} Y_e(\omega). \quad (4.19)$$

The LTSPICE package easily simulates a given circuit over a range of frequencies, but has somewhat limited capabilities for iterating over circuit element values. In order to facilitate the design process we have written a driver for LTSPICE in python. This driver allows the user to programmatically import an existing net list (eg. one produced by a graphical front-end), override parameter values, and produce a new updated net list which is then analyzed by SPICE. Combined with a python module for parsing the resulting simulation data, this driver allowed us to easily iterate over several design parameters and analyze the results in a powerful programming environment.

¹www.linear.com/design-tools/software

4.1.3 Discussion

The results of the numerical simulation are compared with the analytic theory in Fig. 4.3. The expected T_1 of the qubit is plotted against the qubit-resonator detuning Δ for a few values of κ_r and $Q_F = 30$. Good agreement between the theory and numerics appears for $|\Delta| \approx 1\text{ GHz}$ to 0.5 GHz . For detunings below -1.5 GHz the analytic formula exceeds the numerics by approximately a factor of 2. This is probably due to our imperfect assumption that the coupling impedances greatly exceed the resonator impedances. When $|\Delta|$ is on the order of g the qubit and resonator modes hybridize. In this regime the analytic and numerical treatments are both expected to fail because Eq. (4.1) and Eq. (4.19) both implicitly assume that the qubit mode is well defined apart from the rest of the measurement circuit. This failure is manifest in the plots near $\Delta = 0$ where the predicted qubit T_1 becomes smaller than κ_r . This is not physical, as the system cannot lose energy faster than the bare leakage rate of the resonator κ_r .

The predictions shown in Fig 4.3 indicate that we should be able to preserve the qubit coherence with very aggressive resonator ring-up times. The curve for $\kappa_r^{-1} = 11\text{ ns}$ has a T_1 limit of $100\text{ }\mu\text{s}$ at $|\Delta| = 1\text{ GHz}$ and $1000\text{ }\mu\text{s}$ at $|\Delta| = 1.5\text{ GHz}$. These are modest detuning values typical of real experiments. Current best T_1 values for planar transmon qubits are near $60\text{ }\mu\text{s}$ with typical values around $20\text{--}40\text{ }\mu\text{s}$. With the measurement circuit bringing in a decoherence channel at $1000\text{ }\mu\text{s}$ a qubit with internal T_1 of $60\text{ }\mu\text{s}$ would be degraded by only 5%.

Because the T_1 imposed by the measurement circuit varies by several orders of magnitude with varying Δ , it should be possible to use the measurement circuit as a reset. By dynamically tuning the qubit close to the measurement resonator and filter, the T_1 of the would be lowered, forcing the qubit to go to $|0\rangle$ with high probability after several decay time constants. This could be particularly useful in removing “leakage” processes in which the qubit has erroneously gone to state $|2\rangle$.

4.2 Circuit parameters

From our analysis of the qubit damping imposed by the readout circuit in the previous section, and from our analysis of the scattering parameters in Ch. 3 we can now choose parameters for the device. From Fig. 4.3 we find that resonators quality factors of $Q_r \in [500, 1000, 1500, 3000]$ should give well preserved qubit T_1 for $|\Delta| \gtrsim 1\text{ GHz}$. Each Q_r corresponds to $\kappa_r = \omega_r/Q_r$. For each Q_r the value of χ required for a large IQ plane separation between $|0\rangle$ and $|1\rangle$ is determined according to

$$\chi = \omega_r/2Q_r \quad (4.20)$$

(see Eq. (3.31)). The qubit-resonator coupling strength g is then determined from Eq. (3.20)

$$g = \sqrt{\chi\Delta(1 + (\Delta/\eta))} \quad (4.21)$$

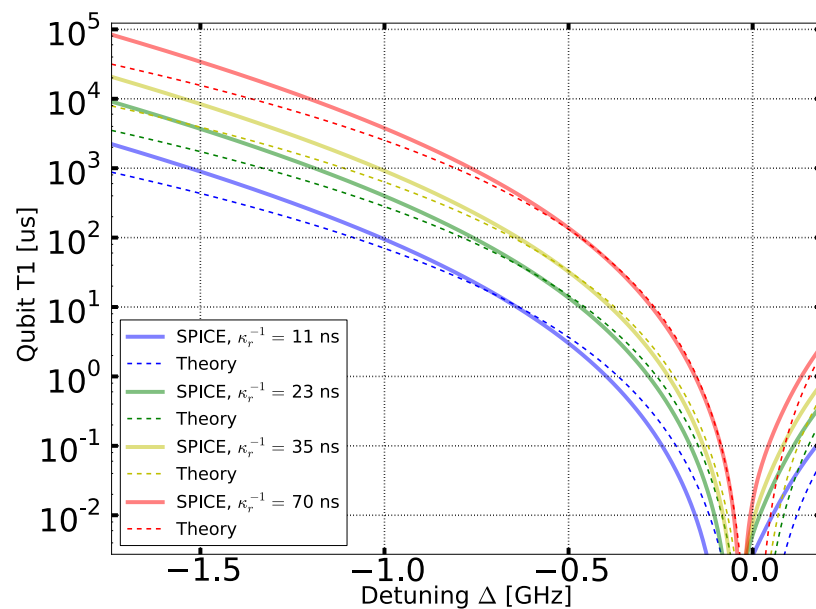


Figure 4.3: Qubit T_1 imposed by the measurement circuit versus qubit-resonator detuning for several values of the resonator decay time. The filter quality factor is $Q_F = 30$.

where $\eta/2\pi \equiv (\omega_{21} - \omega_{10})/2\pi \approx 200$ MHz is the anharmonicity of the qubit. In order to actually build a device with the specified χ , g , and κ_r , we need to know the values of C_g and C_κ . From Appendix D we have

$$C_g = 2g\sqrt{\frac{C_r C_q}{\omega_r \omega_q}} \quad (4.22)$$

where $C_q = 85$ fF is the qubit capacitance and $C_r = \pi/4\omega_r Z_0$ is the effective capacitance of the measurement resonator. The value of C_κ is determined by rearranging Eq. (4.10) as

$$C_\kappa = \sqrt{\frac{C_r}{\omega_r Q_F Q_r Z_F^0}} \quad (4.23)$$

where $Z_F = 4Z_0/\pi$ is the effective capacitance of the filter resonator.

Using these design equations we found four sets of parameters as shown in Table 4.1. The value of κ_r was varied to test the relation between measurement speed and the measurement circuit imposed limit on qubit T_1 .

	$\omega_r/2\pi$ [GHz]	Q_r	κ_r^{-1} [ns]	$\chi/2\pi$ [MHz]	$g/2\pi$ [MHz]	C_g [fF]	C_κ [fF]
Qubit 1	6.805	500	12	6.8	157	8.7	3.0
Qubit 2	6.765	1000	23	3.4	105	5.9	2.1
Qubit 3	6.735	1500	35	2.2	83	4.6	1.7
Qubit 4	6.705	3000	71	1.1	56	3.2	1.2

Table 4.1: Coupling parameters and circuit element parameters for four qubits.

4.3 Device

In this section we describe the physical implementation of the bandpass filter including details of how the chosen circuit parameters were realized on the physical chip.

4.3.1 Layout

A micrograph of the device is shown in Fig. 4.4. The device has four qubit-resonator pairs all coupled in parallel to a common filter. The filter is implemented as a $\lambda/4$ coplanar waveguide resonator embedded into the feed line. The feed line is interrupted on one side with a capacitor forming a voltage antinode, and is shorted to ground on the other side forming a voltage node. The resulting standing wave mode is used as the filter resonance. The measurement resonators are coupled in parallel to a single common filter, and each measurement resonator is capacitively coupled to a qubit.

4.3.2 Filter

The filter is implemented as a $\lambda/4$ coplanar waveguide resonator. The voltage node is formed by connecting the waveguide to ground. The voltage antinode is formed at signal input point (port 1 in Fig. 4.4) where the filter connects to the feed line through a capacitor.

Length

The length of the filter is related to the desired frequency by

$$l = \frac{\lambda}{4} = \frac{\pi v}{2\omega_F} = \frac{\pi c}{2\omega_F \sqrt{\epsilon_{\text{eff}}}} \quad (4.24)$$

where c is the speed of light in vacuum and ϵ_{eff} is the relative relative dielectric constant of the waveguide. For a coplanar waveguide with trace and gap widths much smaller than the thickness of the substrate, we have $\epsilon_{\text{eff}} = (1 + \epsilon_s)/2$ where ϵ_s is the relative dielectric constant of the substrate. In our experiment we used sapphire substrate with $\epsilon_s = 10.4$ giving $\epsilon_{\text{eff}} = 5.7$. For a filter frequency of $\omega_F/2\pi = 6.75$ GHz this gives $l = 4,654 \mu\text{m}$.

Input capacitance

The value of the input capacitance C_{in} is determined by the amount by which we allow the input line to load the filter. The loaded quality factor Q_l of a resonant mode of frequency ω_0 and self capacitance C connected to a resistor environment R_e through a coupling capacitor C_c is

$$Q_l = \frac{C}{\omega_0 R_e C_c^2}. \quad (4.25)$$

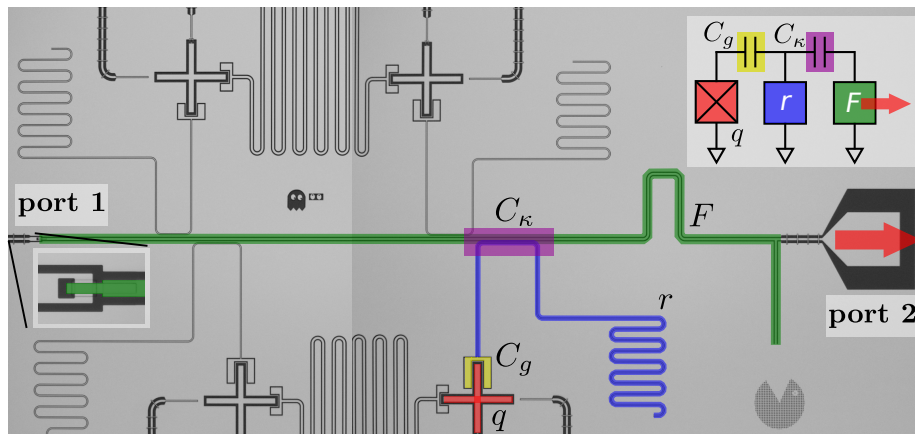


Figure 4.4: Micrograph of the device. The false color corresponds to the colors used in the lumped element model, shown in the top right inset. Signals enter the system through a feed line at port 1. The filter F is formed by a standing wave resonator embedded into the feed line. The feed line is interrupted by a capacitance (left inset) at one end and shorted to ground on the other, forming a $\lambda/4$ resonance. Signals injected at port 1 are mostly reflected by the weak input capacitance. The transmitted energy rings up the filter resonance. Energy leaves the filter through a tap near the shorted end at port 2. The red arrow indicates the path by which energy leaves the filter through a wire bond (not shown) and enters the external detection hardware, including a parametric and HEMT amplifier. The measurement resonators r are connected to the filter via capacitance C_κ formed by the proximity of the filter and resonator traces. The resonator couples to the qubit q through an inter-digitated capacitor C_g . Note that the design allows for an independent resonator for each qubit while allowing several resonators to share a single filter. Note also the filter requires near zero additional on-chip area.

For the filter we rename the parameters $\omega_0 \rightarrow \omega_F$, $C_c \rightarrow C_{\text{in}}$, and $Q_l \rightarrow Q_{\text{in}}$. Using the effective capacitance of our $\lambda/4$ filter resonator $C = \pi/4\omega_F Z_0$, assuming that $R_e = Z_0$, and solving for C_{in} gives

$$C_{\text{in}} = \sqrt{\frac{\pi}{4\omega_F^2 Z_0^2 Q_{\text{in}}}}. \quad (4.26)$$

In our device we used $\omega_F/2\pi = 6.75$ GHz, $Q_{\text{in}} = 40 \times Q_F = 1200$, and $Z_0 = 50\Omega$, which gives $C_{\text{in}} = 12$ fF.

This capacitance was implemented as a parallel plate SiO₂ dielectric capacitor, as shown in Fig. 4.5 a. The dielectric thickness was $t = 200$ nm. With the relative permittivity of SiO₂ of 3.9, this required a plate area of $A = Ct/3.9\epsilon_0 = 70 \mu\text{m}^2$, which is a modest and readily achievable size. Most importantly, this small size avoids the problem of large ground plane cuts which would be needed if we were to implement C_{in} as an interdigitated capacitor.

The SiO₂ has a relatively large loss tangent, making it unsuitable for use in the qubit or measurement resonator. With $\tan \delta \approx 3 \times 10^{-4}$, and corresponding $Q_{\text{SiO}_2} \approx 3,000$ [25], a resonance using SiO₂ dielectric capacitors would have $T_1 \approx 80$ ns at 6 GHz. However, this is not an issue for the filter. The output circuitry strongly loads the filter, in our case giving $Q_F \sim 30$. With $Q_F \ll Q_{\text{SiO}_2}$ the dissipation from the dielectric is much smaller than the photon loss rate through the output circuit. Therefore, the SiO₂ in the filter's input capacitor contributes a negligible fraction of the total loss presented to the qubit, and absorbs a negligible fraction of the dispersed measurement photons.

Input capacitor electrical length

Because of the finite impedance of the input capacitor, the voltage antinode point is not actually a true $\lambda/4$ distance from the voltage node. In other words, the capacitor adds electrical length to the waveguide. This effect must be counterbalanced by modifying the waveguide's geometric length. To compute the necessary adjustment we treat the capacitor as an effective length of transmission line by writing

$$\phi_c = 2\omega_F d_c/v \quad (4.27)$$

where d_c is the effective length of the capacitor, v is the propagation speed in the waveguide, and ϕ_c is the phase shift incurred by reflection from the capacitor. See Fig. 4.5 b for an illustration. The phase shift is computed as

$$\phi_c = \angle \left(\frac{Z_L - Z_0}{Z_L + Z_0} \right) \quad (4.28)$$

where $Z_L = 1/i\omega C_{\text{in}} + Z_0$ is the series impedance of the capacitor and feed line loading the filter resonance, and Z_0 is the characteristic impedance of the line (we assume the filter and feed line characteristic impedances are equal). Combining these results yields

$$d_c = \frac{c}{2\omega_F \sqrt{\epsilon_{\text{eff}}}} \angle \left(\frac{Z_L - Z_0}{Z_L + Z_0} \right) \quad (4.29)$$

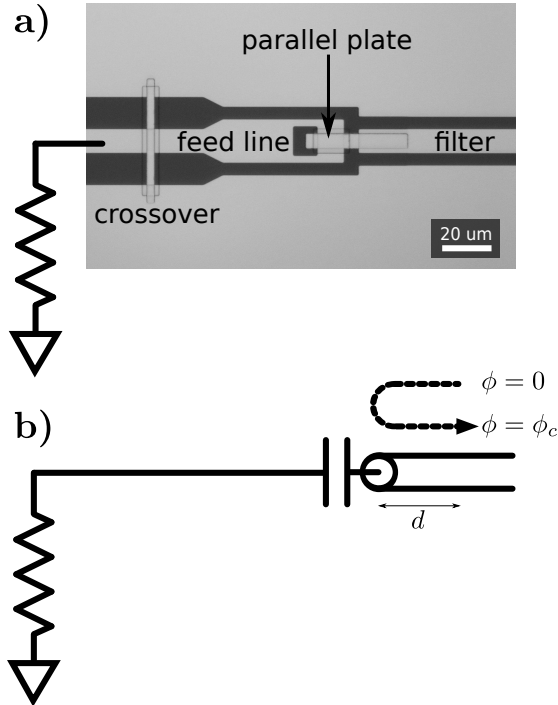


Figure 4.5: Input capacitor for the filter. a) Micrograph of the device. The feed line comes in from the left and the filter coplanar waveguide resonator is on the right. A thin film of SiO_2 separates the connecting aluminum strip on the feed line side. A hole in the feed line renders the overlap area insensitive to optical lithography misalignment. The connecting strip contacts the filter resonator directly. b) Circuit model. A wave reflecting from the input capacitor acquires a phase shift which effectively increases the length of the filter.

which is the length by which the geometric length of the line must be reduced to maintain a resonance frequency of ω_F .

Using this and the previously chosen value $C_{\text{in}} = 12 \text{ fF}$ we compute the effective length of the capacitor to be $d_c = 75 \mu\text{m}$. This length must be subtracted from the geometric length of the filter coplanar waveguide.

Output tap point - Q_F

The dispersed signals exit the filter through a tap off wire connected to the filter near its voltage node. The position of the tap determines the rate at which energy leaves the filter, thus setting Q_F , as we now explain. The voltage profile of the resonant mode in the distributed resonator has a cosine shape $V \propto \sin(\pi x/2l)$ where $x = 0$ is the voltage node at the shorted end and $x = l$ is the voltage antinode at the open end. If the tap were placed at $x = 0$ where the

voltage is zero it would carry no energy away from the filter and the coupling Q induced by the tap would be infinity. If the tap were placed at the voltage antinode at $x = l$ it would feel the maximum of the filter voltage and would be accurately modeled as a shunt resistor in a lumped element equivalent circuit of the filter. Placing the tap at a distance x from the voltage node reduces the power dissipated by R_e by a factor of the square of the relative voltage, $\sin(\pi x/2l)^2$, yielding

$$Q_F = Q_F|_{x=l} / \sin(\pi x/2l)^2. \quad (4.30)$$

where $Q_F|_{x=l}$ is the quality factor we would compute from a lumped element model.

In the lumped element model the loaded Q is given simply by $Q_F|_{x=l} = R_e/Z_F^0$ where R_e is the resistance of the circuit external to the tap, $Z_F^0 = 4Z_0/\pi$ is the characteristic impedance of the filter mode, and Z_0 is the filter transmission line characteristic impedance. Combining this with Eq. (4.30) in the case $R_e = Z_0$ gives

$$Q_F = \frac{\pi/4}{\sin(\pi x/2l)^2} \approx \frac{(l/x)^2}{\pi}. \quad (4.31)$$

We designed for $Q_F = 30$ to get a filter bandwidth of ~ 200 MHz, giving $x = 0.1 \times l$.

Bond pad inductance

Proper flow of return currents is essential to the design of the filter resonator. In Figure 4.6 we show the shorted end of the filter with the tap off through which the signal leaves the filter and enters an amplification chain. Part of the current return path is interrupted by the wire bond pad as shown in the figure. The large perimeter of the bond pad would introduce inductance into the return path and shift the frequency of the filter resonance. To correct this we used SiO₂ dielectric crossovers to tie the ground planes on either side of the tap off path together, thus shorting the inductance presented by the bond pad.

Summary

Here we summarize the steps in the design of the filter:

1. From the desired frequency ω_F compute the geometric length according to

$$l = \pi c / (2\omega_F \sqrt{\epsilon_{\text{eff}}}).$$

2. Choose a loaded quality factor Q_F to get the desired filter bandwidth $\Delta\omega_F$, according to $Q_F = \omega_F / \Delta\omega_F$.

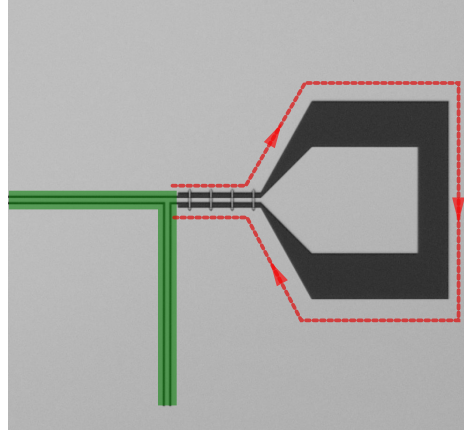


Figure 4.6: Micrograph of the filter tap off point and bond pad. Without crossovers, part of the current return path would flow around the wire bond pad, as shown by the dotted line. The large perimeter of the bond pad would introduce inductance into the return path of filter current and shift the frequency of the filter. Dielectric crossovers connect the ground planes on either side of the tap off path, thus shorting the inductance of the bond pad.

3. Choose an input capacitance C_{in} by requiring that the loading from the input Q_{in} is much ($100\times$) larger than Q_F . The capacitance is determined by

$$C_{\text{in}} = \sqrt{\frac{\pi}{4\omega_F^2 Z_0^2 Q_{\text{in}}}}$$

4. Compute the electrical length of the input capacitor according to

$$d_c = \frac{c}{2\omega_F \sqrt{\epsilon_{\text{eff}}}} \angle \left(\frac{Z_L - Z_0}{Z_L + Z_0} \right)$$

and adjust the geometric length by this amount.

5. Choose the output tap point x according to

$$Q_F = \frac{\pi/4}{\cos(\pi x/2l)^2}$$

and ensure that crossovers are used to connect the ground planes on either side of the tap.

4.3.3 Measurement resonators

The measurement resonators, like the filter, were implemented as $\lambda/4$ coplanar waveguide resonators. In this section we explain how we designed the coupling between the measurement resonators and qubits, and between the measurement resonators and the filter.

Qubit-resonator coupling: claw coupler

The resonators were capacitively coupled to the qubits. Dielectric parallel plate capacitors like the one used for the filter input capacitor could not be used, as the loss tangent of SiO₂ of $\sim 3 \times 10^{-4}$ [25], would limit the qubit T_1 . Instead, we used interdigitated capacitors as shown in Fig. 4.7, which we have nicknamed the “claw”. The claw not only couples the resonator to the qubit, but also forms a large capacitance to ground. This capacitance to ground changes the resonator’s effective length similarly to the filter input capacitor, although the effect is somewhat more complex as the claw also adds significant geometric length.

With no reliable means to analytically compute the effect, we instead used the Sonnet² numerical electromagnetic simulation package to find the phase shift incurred by reflection from the claw. The coupling capacitance C_g between the qubit and resonator, and the phase incurred by reflection from the claw was found as a function of frequency and claw length L . The results of the simulation were fit with second order polynomial curves as given in Tables 4.2 and 4.3.

Here we summarize the design of the claw couplers:

1. From the desired coupling strength g the value of C_g is chosen from Eq. (4.22).
2. Use the data from Table 4.2 to find the appropriate length L of the claw.
3. Use the data from Table 4.3 to find the phase shift imposed by the claw. This phase is then converted to an effective length in the same way as was done for the filter.
4. Adjust the resonator length to account for the phase shift.

Resonator-filter coupling: parallel line coupler

The capacitive coupling between the measurement resonators and filter was implemented by allowing their center traces to run parallel over a length w to allow in-plane, as shown in Fig. 4.8. The measurement resonator and filter traces are separated by a strip of ground plane of width x to keep the ground plane equipotential. The parameters x and w were adjusted to get the desired coupling capacitance C_κ . This capacitance was computed numerically using Sonnet in a procedure entirely similar to that described above for the resonator-qubit coupling. The results of the Sonnet simulation are summarized in Table 4.4.

The coupling capacitance C_κ was determined by the desired ring-up rate of the resonator κ_r . From Eq. (4.10) we find

$$\kappa_r = \left(\frac{4}{\pi} \right)^2 \omega_r^3 Q_F Z_0^2 C_\kappa^2 \longrightarrow C_\kappa = \frac{\pi}{4} \sqrt{\frac{\kappa_r}{Q_F Z_0^2 \omega_r^3}} \quad (4.32)$$

where we’ve used $Q_r = \omega_r / \kappa_r$. For $\kappa_r^{-1} = 50$ ns and $Q_F = 30$ we find $C_\kappa = 1.47$ fF.

²www.sonnetsoftware.com

Frequency [GHz]	p_0	p_1	p_2
4.8	-0.7610256	23.42786129	-30.03751643
5.0	-0.75985036	23.40431259	-30.03256152
6.705	-0.74027938	23.11730508	-29.92148358
6.735	-0.73999725	23.11213134	-29.91986705
6.765	-0.73971394	23.10693518	-29.91824295
6.805	-0.73933434	23.09997203	-29.91606597

Table 4.2: Claw length L as a function of qubit-resonator coupling capacitance C_g . For each frequency, the claw length and capacitance are related according to $L/\mu\text{m} = \sum_{n=0}^2 p_n (C_g/\text{fF})^n$.

Frequency [GHz]	p_0	p_1	p_2
4.8	1.52E-007	-1.24E-003	-8.51E-002
5.0	1.61E-007	-1.29E-003	-8.87E-002
6.705	2.47E-007	-1.74E-003	-1.19E-001
6.735	2.49E-007	-1.74E-003	-1.19E-001
6.765	2.50E-007	-1.75E-003	-1.20E-001
6.805	2.53E-007	-1.76E-003	-1.21E-001

Table 4.3: Phase shift ϕ as a function of claw length L . For each frequency the phase shift and claw length are related by $\phi/\text{rad} = \sum_{n=0}^2 p_n (L/\mu\text{m})^n$.

x [μm]	p_0	p_1	p_2
2	0.00367265	64.6536	-53.9095
5	0.0169587	101.302	-61.7247
8	0.0382334	143.915	-68.7105

Table 4.4: Coupling arm length w as a function of capacitance C_κ for several values of the width x of the ground plane strip. For each value of x , w is related to C_κ according to $w/\mu\text{m} = \sum_{n=0}^2 p_n (C_\kappa/\text{fF})^n$.

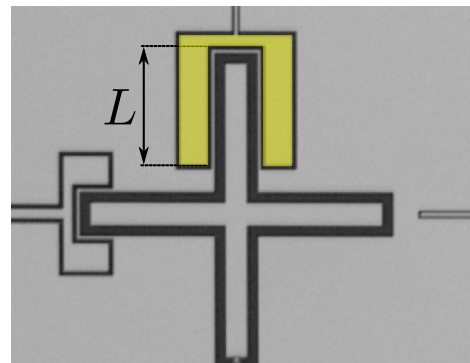


Figure 4.7: The interdigitated capacitor connecting the measurement resonator and qubit. Note the thin wire connecting the ground plane on either side of the topmost qubit finger.

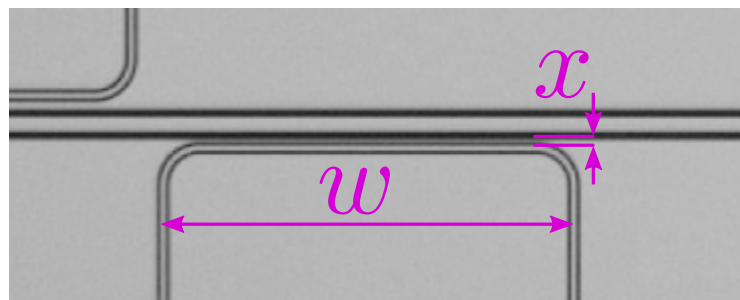


Figure 4.8: Coupling between a measurement resonator and the filter.

4.3.4 Mode shape coupling factor

Because the voltage profile in a distributed resonator is not constant, the capacitances coupling the measurement resonators required an additional adjustment. Each capacitance was multiplied by

$$[\cos(\pi x_r/2l_r) \cos(\pi x_F/2l_F)]^{-1}$$

where x_r is the distance of the coupler from the measurement resonator voltage antinode, and x_F is the distance of the coupler from the filter voltage antinode.

4.3.5 Parameters

Using the results contained in Tables 4.2, 4.3, and 4.4 we converted the values of C_g and C_κ from Table 4.1 to physical dimensions for use in the fabricated device.

4.4 Fabrication

The device was made of thin film aluminum film deposited on a sapphire substrate. Silicon dioxide was used a dielectric layer for the filter input capacitor and for wiring crossovers used to connect the ground planes. The Josephson junctions were made of an Al/AlO_x/Al tri-layer. The fabrication process is summarized in the following steps:

1. Control lines and resonators are defined.
 - (a) Approximately 100 nm of aluminum is deposited on a 3 inch sapphire wafer via electron beam evaporation.
 - (b) A pattern defining the measurement resonators, filter, input/output lines, and qubit control lines is etched into the film using optical lithography and chemical etching in an inductively coupled plasma (ICP) etcher with BCl₃/Cl₂.
2. Dielectric crossovers are formed to bridge the ground planes on either side of the measurement input and output lines, and the qubit control lines.
 - (a) A 200 nm thick layer of silicon dioxide is deposited through an optically defined photoresist mask to form the insulating layer of the crossovers in a lift-off procedure.
 - (b) The underlying aluminum film is ion milled to remove the oxide layer. A new aluminum layer is deposited through a photoresist mask to form the crossover wires via lift-off.
3. The cross shape of the transmon qubit is etched into the base aluminum layer via the same method used to define the control lines and resonators.

4. An alignment mark pattern is formed with electron beam evaporated gold via lift-off.
5. The Josephson junctions are formed using double angle shadow mask evaporation. The shadow mask is formed via electron beam lithography. This step uses the previously defined gold alignment marks to align the electron beam pattern with the optical patterns from previous steps. The base layer is ion milled prior to the junction deposition to remove the oxide.

Chapter 5

Experimental Setup and methods

In this chapter we present the experimental apparatus used to test dispersive measurement with the bandpass filter. In the first section we show a complete schematic of the apparatus and describe how the measurement signal is brought into and out of the qubit chip. In the next section we discuss the details of generation of the measurement signals. In the final section we discuss details of detection of the measurement signals.

5.1 Wiring

A custom microwave processing system was used to generate and detect the measurement pulses. A simplified diagram of the experimental setup shown in Fig. 5.1 serves as the main reference for our discussion.

5.1.1 General view

The microwave probe signals were generated with a custom designed 1 Gs/s arbitrary waveform generator (AWG) and IQ mixer at room temperature. The generated signal contains one frequency component for each measurement resonator being probed. The signal travels through several stages of attenuation at 4 K and 40 mK which dissipate thermal and technical noise. When the measurement pulse arrives at the chip most of it is reflected from the input capacitor, and a small portion is transmitted into the bandpass filter. Once inside the filter, each frequency component of the transmitted signal scatters from its corresponding measurement resonator, acquiring a qubit state dependent phase and amplitude shift. The dispersed signal leaves the chip through the filter tap-off path (red arrow in Fig. 4.4) and enters a series of filters and switches at 40 mK before it is amplified by a parametric amplifier (paramp). The signal is

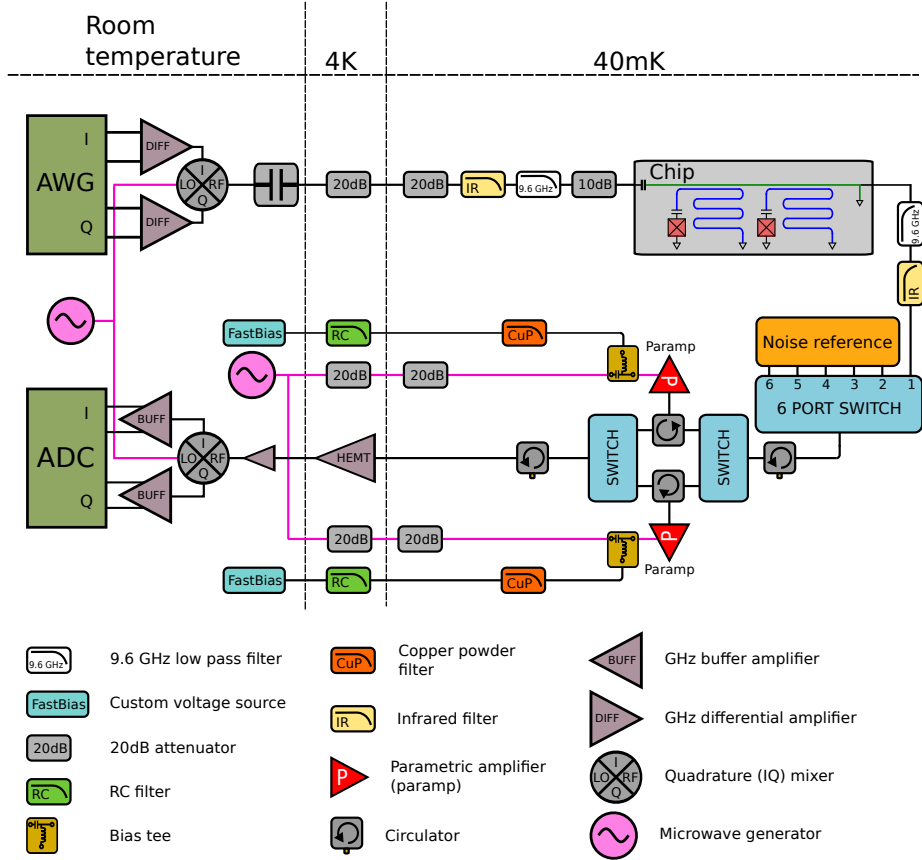


Figure 5.1: Schematic of the measurement system.

then further amplified by a high electron mobility transistor (HEMT) amplifier at 4K before it is brought up to room temperature, further amplified, and detected by a custom designed GHz analog to digital converter (ADC).

5.1.2 Input line

Several stages of attenuation and filtering are used on the signal input path to ensure that thermal and technical noise is blocked from entering the qubit chip.

Review of thermal noise

The thermal noise of a resistor R , at temperature T follows the Plank distribution¹

$$S_V^p(f, T) = \frac{2Rhf}{e^{hf/k_bT} - 1}. \quad (5.1)$$

The superscript p in S^p reminds us that this is a “physicist’s” spectral density defined for both positive and negative frequencies. For $k_bT \gg hf$ we expand in powers of hf/k_bT , finding $S_V^p(f, T) \approx 2R(k_bT - hf/2)$. Multiplying by a factor of 2 to convert to a single sided “engineer’s” spectral density, and dropping the small constant $-hf/2$ we find $S_V^e \approx 4Rk_bT$, which is the usual Johnson noise formula.

Line attenuation and filters

The qubit, measurement resonator, and filter resonances are all in the 5 GHz to 7 GHz range. For this frequency range, $T_{\text{eff}} \equiv hf/k_b$ is in the range 240 mK to 335 mK. Therefore, the parts of the apparatus at 295 K (room temperature) and 4 K are deep in the $k_bT \gg hf$ limit, and we can analyze their noise properties using the Johnson noise formula. In this limit, the thermal noise power scales linearly with T . Therefore, in order to reduce noise coming from a high temperature stage at T_{high} to the level of a lower temperature stage at T_{low} , we attenuate the line by a factor of $T_{\text{high}}/T_{\text{low}}$. Accordingly, we attenuate by a factor of 20 dB ($\times 100$) in between the room temperature and 4 K stages, as shown in Fig. 5.1.

The Johnson noise formula is invalid at the 40 mK stage where $hf \gtrsim k_bT$. In this limit, the thermal noise power scales as $\exp[-hf/k_bT]$. This scaling is stronger than the linear scaling in the Johnson limit. Consequently, the factor of 100 reduction in temperature going from 4 K to 40 mK requires more than 20 dB of attenuation in the line.

A simple way to understand this is to consider the ratio of thermal noise power from sources at two temperatures for a fixed frequency $f = 6$ GHz. Defining a reduced temperature as $x \equiv k_bT/hf$, we write the Planck power distribution as

$$S_V(T) \propto \frac{1}{e^{1/x} - 1}. \quad (5.2)$$

The ratio of the noise power for a source at temperature αT to the noise power from a source at temperature T is

$$\frac{S_V(\alpha T)}{S_V(T)} = \frac{e^{1/\alpha x} - 1}{e^{1/x} - 1}. \quad (5.3)$$

This function is plotted for the case $T = 4$ K ($x = 13.8$) and $f = 6$ GHz in Fig. 5.2. In going from 4 K ($\alpha = 1$) to 40 mK ($\alpha = 10^{-2}$), the thermal noise drops by 5 orders of magnitude, as opposed to 2 orders predicted by the Johnson

¹Note that these spectral densities are all written in terms of the root mean square (RMS) of the voltage fluctuations.

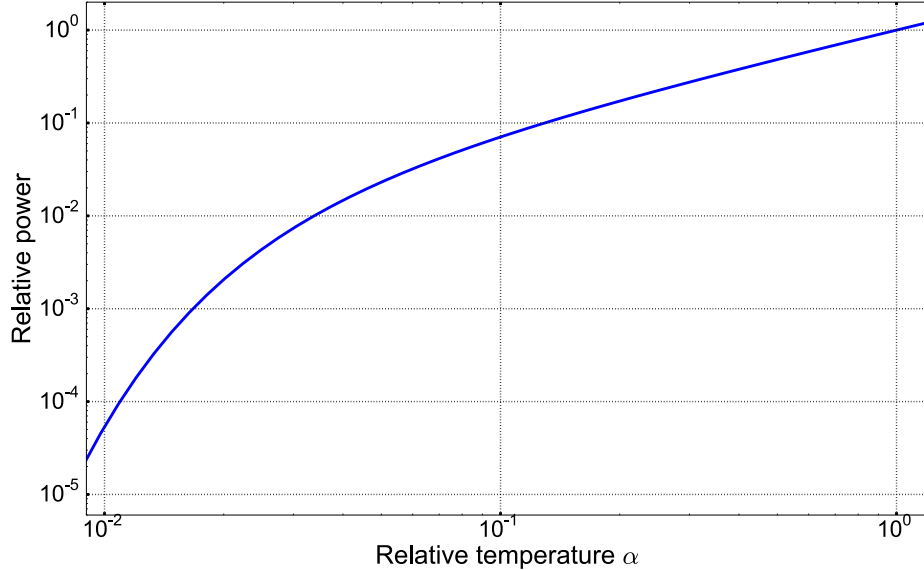


Figure 5.2: Ratio of voltage noise spectral density $S_V(\alpha T)/S_V(T)$ for $T = 4\text{ K}$ and $f = 6\text{ GHz}$.

formula. We accounted for this by using 30 dB line attenuation, plus another 20 dB of isolation from the filter's input capacitor.

In order to remove noise at higher frequencies, we added a 9.6 GHz low pass reflective filter. Additionally, an infra-red (IR) filter was used to absorb high frequency radiation propagating down the coaxial transmission line to prevent generation of quasiparticles in the superconductor [4].

Ground loops

An inner DC block placed just after the AWG was crucial to the setup. Without this block, a ground loop introduced kHz frequency signals into the paramp, modulating its gain. The block broke this ground loop and stabilized the paramp gain. We also found that care was needed in breaking the grounds between the computer controlling the six port switch and the rest of the apparatus. In the initial setup, the digital communication line between the computer and the switch control box had the inner and outer conductors broken at different points, almost two meters apart. This created a large capacitance which allowed transmission of noise from the computer to the control box. This was fixed by adding a low pass filter where the control box lines entered the cryostat.

5.1.3 Output line

Immediately upon exiting the chip, the measurement signal passes through another reflective low pass filter and IR filter. No attenuator was used here because

loss of measurement photons degrades the quality of the measurement.² The IR filter introduces ~ 2 dB of loss.

The output signal next went through a Radiall R573423600 six port microwave switch. This allowed us to switch *in-situ* the input to the parametric amplifier. Switching to calibrated noise sources allowed us to check the noise properties of the paramp. The signal next passed through a Radiall R572433000 two port switch which allowed us to select between two paramps. This was done because one of the amplifiers used a new design which was not fully tested and we wanted to have the second amplifier as a fall-back. The new design turned out to work extremely well and was critical to the success of the experiment. The signal next entered a circulator which directed it to the paramp where it was amplified and reflected. The circulator directs the reflected signal toward the second two port switch. Because the directivity of the circulator is imperfect, some of the reflected amplified signal and noise goes backwards toward the chip. To eliminate this backward signal, another circulator configured as an isolator was included between the six port switch and the first two port switch. After leaving the paramp the signal goes through a second two port switch, another circulator configured as an isolator, and then entered a Low Noise Factory HEMT. The purpose of the paramp was to amplify the measurement signal above the input referred noise of the HEMT, which in this experiment was approximately 2.5 K. The unusually low noise of the HEMT was a major advantage as it lowered the requirement on the paramp gain. After amplification by the HEMT the signal travelled out of the cryostat to room temperature amplifiers which increased the signal level enough to drive an IQ mixer. The I and Q components generated by the IQ mixer were buffered by custom designed GHz op-amp buffer amplifiers which drove two inputs of a custom Gs/s ADC.

5.2 Signal generation

The measurement signals were produced by a custom FPGA controlled 1 Gs/s arbitrary waveform generator (AWG). The two channels of the AWG drove the I and Q ports of a Marki IQ mixer. With a cosine signal $\cos(\delta\omega t + \phi)$ on the I channel, and $\sin(\delta\omega t + \phi)$ on the Q channel, the radio frequency (RF) signal leaving the RF port of the mixer is

$$\cos([\omega_c + \delta\omega]t + \phi) \quad (5.4)$$

where ω_c is the carrier frequency at several GHz [29]. We probe multiple measurement resonators simultaneously by superimposing IQ sinusoids to generate a signal with multiple frequency components. The 1 Gs/s AWG has a usable bandwidth of 500 MHz due to the Nyquist criterion. Combined with the IQ mixer, this allows for a usable RF bandwidth of $\Delta\omega/2\pi = 1$ GHz centered around ω_c . In practice, the AWG outputs are filtered by absorptive Gaussian low pass filters to remove harmonic created by the shape of the AWG digital samples. This limits the usable bandwidth to $\Delta\omega/2\pi \approx 600$ GHz.

²This point is discussed quantitatively in section 3.6.

5.3 Signal detection

The dispersed frequency components coming from the chip and subsequent amplifiers are, like the drive signal, of the form

$$s(t) = \cos [(\omega_c + \delta\omega)t + \phi], \quad (5.5)$$

where ω_c is the frequency of the carrier, $\delta\omega$ is detuning of the measurement signal from the carrier, and ϕ is the phase of the signal which includes the phase shift caused by dispersion from the measurement resonator. After demodulation in the IQ mixer, the I and Q signals are [29]

$$I(t) = \cos (\delta\omega t + \phi), \quad Q(t) = \sin (\delta\omega t + \phi). \quad (5.6)$$

These low frequency signals were digitized by the ADC to

$$I_n = \cos (\delta\omega t_n + \phi), \quad Q_n = \sin (\delta\omega t_n + \phi). \quad (5.7)$$

where $t_n = n/f_s$ and $f_s = 1/500$ ns is the sampling frequency of the ADC.³ The sampled signals I_n and Q_n are treated as the real and imaginary parts of a complex number

$$z_n \equiv I_n + iQ_n = \exp (i [\delta\omega t_n + \phi]). \quad (5.8)$$

The complex signal z_n is multiplied by $\exp (-i\delta\omega t_n)$ to produce

$$z'_n \equiv z_n \exp (-i\delta\omega t_n) = \exp (i\phi). \quad (5.9)$$

Finally, z'_n is integrated over the duration of the pulse. The integration acts as a low pass filter, which increases the signal to noise ratio. The end result is a single point in the two-dimensional plane, whose phase is the same (up to constant rotations coming from digital and analog time delays) as the phase of the original analog signal. In this way, the phase of the dispersed signal is measured and the corresponding qubit state inferred.

³The sampling frequency is 1 GHz, but time-adjacent samples are summed together in the FPGA to use less resources in the following processing stages.

Chapter 6

Results

In this chapter we present the results of the experiment. We focus first on detailed characterization of a single qubit measurement channel, and then present data in which several qubits were measured simultaneously.

6.1 Characterization

6.1.1 Resonator frequencies

We first measured the frequencies of the four resonators on the chip. Using a vector network analyzer we probed the system with a variable frequency microwave tone and measured the transmitted amplitude and phase S_{21} . Results are shown in Fig. 6.1. The four dips in transmission correspond to the four resonators, and the broad peaked structure comes from the bandpass filter. In an initial run with a test chip we found the filter bandwidth to be ~ 200 MHz at 6.5 GHz, giving $Q_F \approx 32$, very close to the target value of 30. In the final iteration, the addition of crossovers near the output bond pad placed the filter frequency at 6.8 GHz, much closer to the target value 6.75 GHz.

The resonator parameters are summarized in Table 6.1. Three of the resonator frequencies were within 32 MHz of the target values, and the spacings were within 6 MHz of the target values. The resonator for Q_3 however was 113 MHz too high. We do not know the reason for this error but it was likely a mistake in the computer file defining the geometry of the photo-lithography mask for the chip, or a physical defect in the resonator causing a short to ground, which reduced the resonator's electrical length and raised its frequency.

6.1.2 Coupling strength - g

Further characterization required use of the qubit, so we had to roughly tune up the measurement system. We placed the measurement probe frequency at $\omega_{\text{probe}} = \omega_{r,|0\rangle}$, ie. the frequency of the measurement resonator with the qubit in the ground state. While this choice of probe frequency is not optimal, but

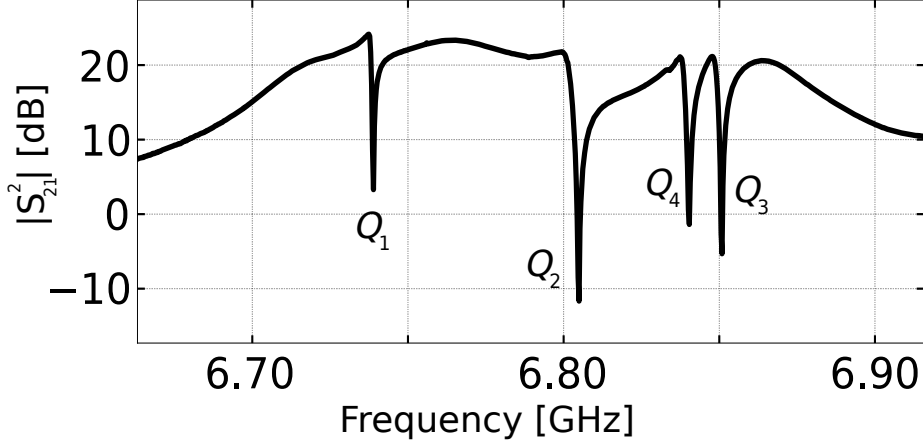


Figure 6.1: Transmission through the measurement circuit. Transmitted power is plotted with an arbitrary vertical offset associated with all of the various attenuation and amplification factors in the system which were not calibrated. Four transmission dips appear at the measurement resonators. Q_3 was significantly far away from its target frequency. The broadly peaked background comes from the bandpass filter.

it yields enough separation in the IQ plane to calibrate control pulses on the qubit.

We next measured the qubit-resonator coupling strengths g . Because of the large detuning between the qubit and resonator we could not directly measure g through a time resolved rate of photon swap between the qubit and resonator. Instead, we used the dispersive physics discussed in Chapter 3, specifically Eq. (3.20), which connects g with the dispersive shift χ ,

$$g = \sqrt{\chi\Delta(1 + \Delta/\eta)}. \quad (6.1)$$

Here $\Delta \equiv \omega_{10} - \omega_r$ is the qubit-resonator detuning, and $\eta \equiv \omega_{21} - \omega_{10}$ is the anharmonicity of the qubit. We measure the qubit frequencies ω_{10} and ω_{21} and the qubit anharmonicity via spectroscopy and then compute Δ and η . We then measured χ by performing spectroscopy of the resonator after the qubit was prepared in $|0\rangle$ or $|1\rangle$. In either case we observe a dip in transmission at the resonance frequency $\omega_{r,|0\rangle}$ or $\omega_{r,|1\rangle}$, as shown in Fig. 6.2. This provides a measure of χ through the relation $2\chi = \omega_{r,|1\rangle} - \omega_{r,|0\rangle}$, from which we compute g via Eq. (6.1). The coupling strengths measured in this way are given in Table 6.1.

6.1.3 Resonator transient response rate - κ_r

We next measured the strength of the resonator-environment coupling, characterized by the leakage rates κ_r . From the qubit-resonator coupling term in the

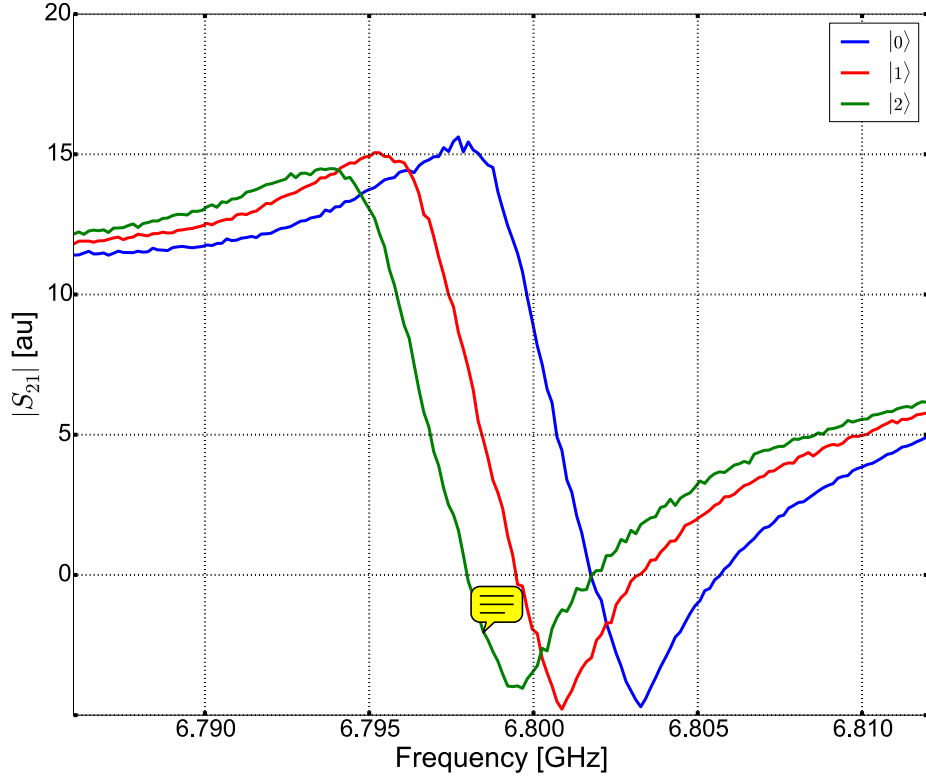


Figure 6.2: Transmission through the measurement circuit for three qubit states. Asymmetry in the resonance dips comes from impedance mismatch in the input and output of the measurement circuit.

	$\omega_r/2\pi$ [GHz]	$g/2\pi$ [MHz]	$1/\kappa_r$ [ns]
Q_1	6.835 (6.805)	100 (146)	19 (12)
Q_2	6.789 (6.765)	86 (102)	37 (23)
Q_3	6.848 (6.735)	76 (84)	50 (35)
Q_4	6.737 (6.705)	50 (59)	147 (71)

Table 6.1: Parameters for the four qubits. Each was designed with a different target κ_r in order to test the tradeoff between damping and measurement speed. Target design values are given in parentheses. Disparity between target and measured values probably comes from errors in predicting in-plane capacitances between structures.

dispersive Hamiltonian (Eq. (3.19)) we find that the resonator photons shift the qubit frequency by

$$\delta\omega_{10} = -2\chi n \quad (6.2)$$

where n is the number of photons in the resonator. Because the qubit frequency shift is proportional to the photon number, a measurement of the decay time of $\delta\omega_{10}$ yields a measurement of the time decay constant for n , which is κ_r by definition.

We measured the time decay constant κ_r with a ring-down technique. The pulse sequence is shown in Fig. 6.3 a. With the qubit in $|0\rangle$ we drive photons into the resonator with a stimulation pulse at the measurement frequency. During this pulse, photons accumulate in the resonator, raising n and shifting ω_{10} according to Eq. (6.2). The resonator drive pulse is turned off and the resonator is allowed to freely ring down. As the resonator photon number $n(t)$ changes dynamically during the sequence, the ac Stark shifted qubit frequency also changes as $\delta\omega_{10}(t) = -2\chi n(t)$. To measure $\omega_{10}(t)$ at each point in time, we apply a π -pulse to the qubit at variable time τ and with variable frequency ω_{probe} . At each value of τ , the π -pulse only excites the qubit if $\omega_{\text{probe}} \approx \omega_{10}(t)$. At the end of the sequence, we measure the qubit state by again probing the resonator, thus measuring the probability that the qubit was excited by the π -pulse. This yields a measurement of $\omega_{10}(t)$, as shown in Fig. 6.3 b. Through Eq. (6.2) and using the previously measured value of χ , we convert the measured ω_{10} to $n(t)$, generating a plot of resonator photon occupation versus time during the measurement pulse, as shown in Fig. 6.3 c. The value of κ_r is extracted by fitting the free decay part of the data. Note that conversion from $\delta\omega_{10}(t) \rightarrow n(t)$ is not necessary for the extraction of κ_r , as the relevant decay time can be extracted directly from $\omega_{10}(t)$. We present the $n(t)$ as an accompaniment to the $\delta\omega_{10}(t)$ data shown in Fig. 6.3 b, and because it will be useful later in our discussion of qubit state transitions induced by the measurement photons.

Values of κ_r for each resonator are given in Table 6.1. The measured values of κ_r were approximately 50% lower than the target values. This discrepancy has not been understood for our chip. A subsequent chip using a $\lambda/2$ bandpass filter based on the work described here had a similar error in which the values of κ_r were lower than the design values. It will be important to understand this divergence in the future.

6.2 Photon number calibration

In the previous section, we showed how to measure the resonator photon number using the ac Stark shift. We used Eq. 6.2 to convert a time resolved measurement of $\delta\omega_{10}$ to a time resolved measurement of n . We also need a calibration between resonator drive *amplitude* and the steady state value of n . This can be thought of as measuring the $t = 100$ ns point of Fig. 6.3 c as we vary the amplitude of the measurement resonator drive pulse. Therefore, the pulse sequence is essentially the same as shown in Fig. 6.3 a, with two differences.

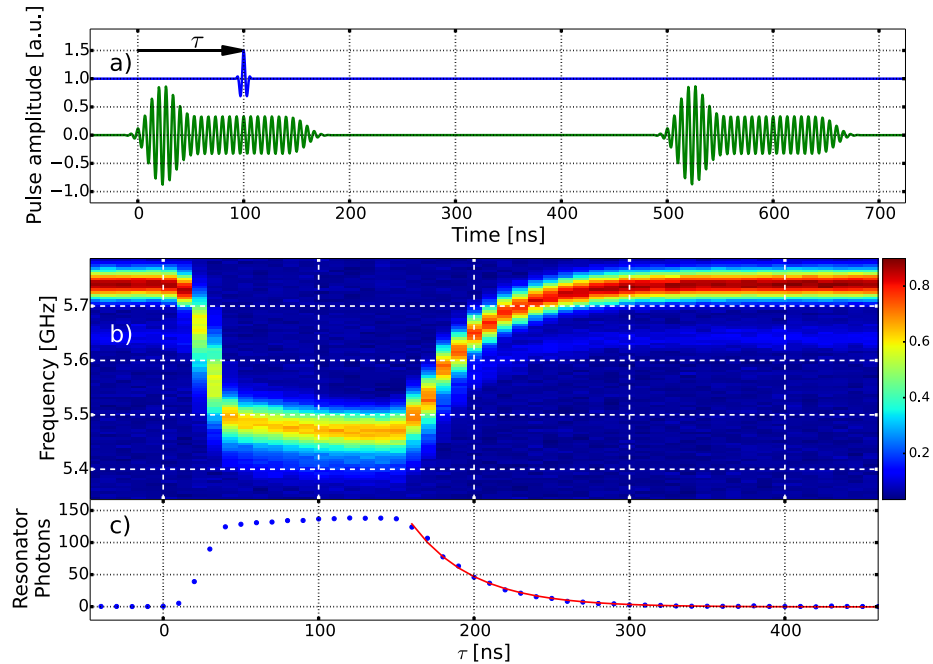


Figure 6.3: Resonator photon occupation during the measurement pulse. a) The control sequence applied to the I port of the IQ mixer used to control the resonator and qubit. We apply two measurement pulses (green) to the resonator. Note the emphasis at the beginning of the pulse which acts to ring up the resonator faster than the ring-up time $1/\kappa_r$. During the first pulse, we apply a π -pulse (blue) to the qubit at a variable time τ and frequency. Only when ω_{probe} matches the qubit frequency is the qubit excited. The second measurement pulse checks whether or not the qubit was excited by the π -pulse. b) Probability (color scale) of qubit excitation versus time and frequency of π -pulse. The curve of high qubit probability provides a measure of the qubit frequency as a function of time during the measurement pulse. c) Qubit frequency converted to resonator photon occupation via Eq.(6.2). The red curve is an exponential fit to the decay.

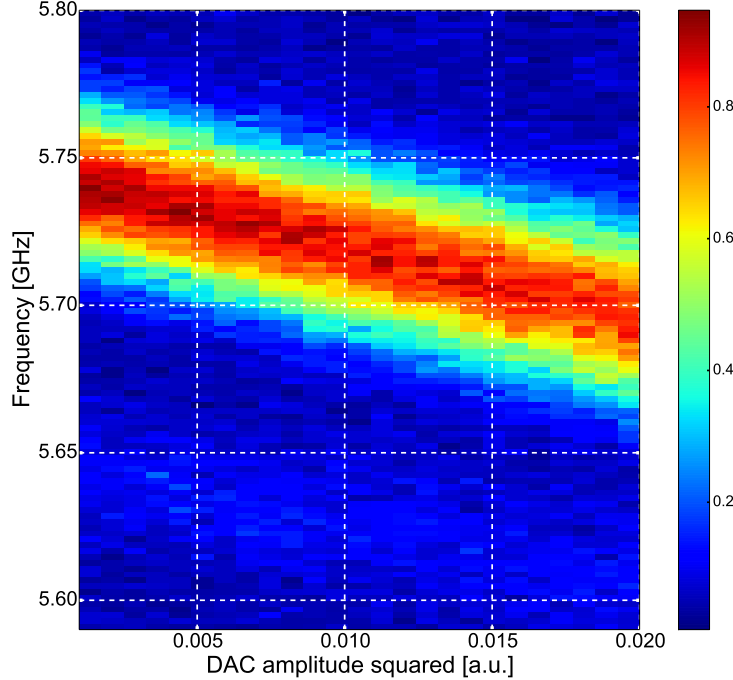


Figure 6.4: AC Stark shift measured via qubit detuning during measurement.

1. The π -pulse placed at a fixed τ , in the steady state part of the resonator ring up.
2. We vary the resonator drive pulse amplitude.

This yields a measurement of the qubit frequency as a function of resonator drive amplitude, as shown in Fig. 6.4. Assuming that the resonator internal energy is proportional to the square of the amplitude of the drive signal, we have

$$\frac{\delta\omega_{10}}{2\chi} = n = mA^2. \quad (6.3)$$

With the value of χ previously, we measure the dependence of $\delta\omega_{10}$ on the drive amplitude and extract m . In subsequent experiments we mapped drive amplitude to resonator photon number via $n = mA^2$.

6.3 Stimulated qubit transitions

The visibility of the qubit state measurement increases as we collect more scattered photons. Therefore, probing the measurement circuit with a higher power

pulse should lead to better measurement visibility. However, at large numbers the resonator photons induce qubit transitions between the $|0\rangle$ and $|1\rangle$ states [13, 38]. To determine how hard we could drive the measurement system without disrupting the qubit, we measured the qubit state transitions as a function of resonator drive power. We prepared the qubit in either $|0\rangle$ or $|1\rangle$ and then applied a measurement pulse with variable power. We then allowed the resonator to ring down, and finally probed the resonator with a measurement pulse to determine the state of the qubit. The pulse sequence is illustrated in Fig. 6.5 a. In this way we measured the probability of a qubit transition from initial states $\{|0\rangle, |1\rangle\}$ to final states $\{|0\rangle, |1\rangle, |2\rangle\}$ as a function of the driving DAC amplitude. We then converted the DAC amplitude to resonator photon number using the ac Stark shift calibration.

We observe a sharp onset of stimulated qubit state transitions at sufficiently high photon numbers, as shown in Fig. 6.5 b. As shown in Fig 6.5 b, $|1\rangle \rightarrow |0\rangle$ transitions set in abruptly at $n \gtrsim 100$. The complementary transition, $|0\rangle \rightarrow |1\rangle$ sets in at $n \gtrsim 175$. Note also that we observed transitions to $|2\rangle$ from both initial states.

At low photon numbers, the probabilities for no transition, such as $|0\rangle \rightarrow |0\rangle$, are not 1. The main contributing factor to this is that when idle, the qubits are not perfectly in the ground state. We observe between 4% and 8% idle $|1\rangle$ population, which means that the $|0\rangle \rightarrow |0\rangle$ probability will be no greater than 0.92-0.96. This same effect raises the $|1\rangle \rightarrow |0\rangle$ at low photon numbers: if the qubit is erroneously prepared in $|1\rangle$, then a π -pulse intended to prepare $|1\rangle$ instead puts the qubit in $|0\rangle$. This process manifests as a nonzero probability for $|1\rangle \rightarrow |0\rangle$ at low photon number.

We used these data to choose the maximum usable photon number. As a rule of thumb, we kept the photon number at 1/2 the value of the sharp onset of qubit state transitions. The exact value depended on the values of g for each qubit, and the operating value of Δ . Later, in our analysis of the time dependent measurement fidelity, we will see that the fidelity numbers themselves place a strong bound on the probability of stimulated qubit transitions, providing further indication that our experiments were done at values of n which preserved the qubit state.

6.3.1 Comparison with theory

In the dispersive Hamiltonian given in Eq. (3.17), the photon number operator n couples only to the qubit σ_z . Therefore, resonator photons should not induce upward or downward transitions of the qubit state. Our treatment of the dispersive limit assumes $g/\Delta \ll 1$, but ignores the additional dimensionless factor of n itself. This suggests that at large values of n , our lowest order expansion becomes insufficient and other terms involving qubit transitions via σ_x or σ_y may appear. We do not give a full account of this physics, but comment on how the critical n found in our data relates to rough theoretical predictions. The dispersive Hamiltonian is an expansion to first order in $(g/\Delta)^2$. Therefore, we might expect qubit transitions for $n > (\Delta/g)^2$. In the literature, the critical

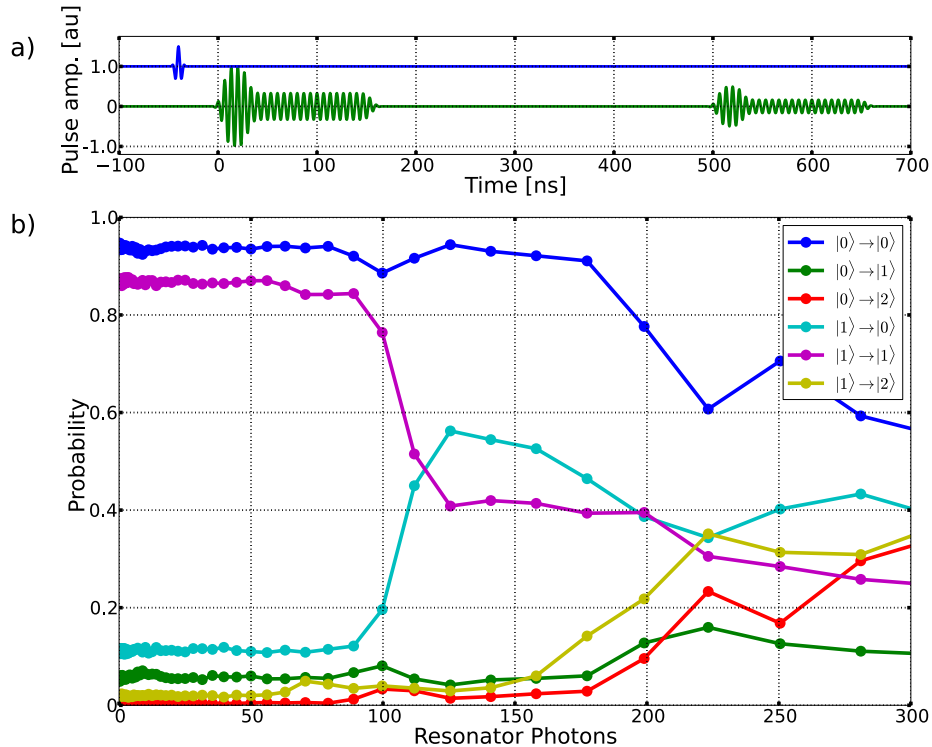


Figure 6.5: Qubit transitions stimulated by the measurement pulse. a) Pulse sequence. The qubit is prepared into the $|0\rangle$ ($|1\rangle$) state with an idle (π -pulse) as shown in blue. We then drive the measurement resonator with a variable power pulse, as shown in green. This pulse can induce qubit state transitions. After a ring-down period, we probe the measurement resonator with a low power pulse to measure the state of the qubit. b) Probabilities for the final state of the qubit for initial states $|0\rangle$ or $|1\rangle$. Each curve labelled $|i\rangle \rightarrow |f\rangle$ gives the probability that the qubit prepared in state $|i\rangle$ is measured at the end of the sequence to be in state $|f\rangle$.

photon number is defined as $n_{\text{crit}} \equiv (\Delta/g)^2/4$. In the present experiment we have $n_{\text{crit}} \approx 30$. Interestingly, we do not observe stimulated transitions until $n \approx 3 n_{\text{crit}}$.

To our knowledge, neither the precise photon number at which qubit transitions are induced, nor even the sharp onset with increasing n has been understood in the theoretical literature. Characterization and theoretical understanding of this effect would be a natural continuation of the present work.

6.4 Coherence

The bandpass filter was designed to increase the $\kappa_r T_1$ product. In Section 6.1.3 we saw κ_r values as fast as 1/19 ns. It remains to see that the qubit T_1 was preserved. We measured each qubit's T_1 over a range of frequencies, finding typical values between 10 μ s and 12 μ s over a range of qubit frequencies giving $\Delta > 800$ MHz. A full data set for qubit 2 is shown in Fig. 6.6. Without the filter, we expect a T_1 limit of $(\Delta/g)^2/\kappa_r = 3.2$ μ s at $\Delta = 800$ MHz. As the measured T_1 values exceed that limit, we know that the filter successfully protected the qubit. Of course, the qubit T_1 does not reach the upper limit allowed by the filter. This was intentional, as we do not want the measurement circuit imposing additional decoherence of the qubit. In other words, the qubit T_1 was dominated by loss channels other than the measurement circuit.

6.5 Time dependence and accuracy

In this section we present the measurement accuracy and its dependence on integration time. The results presented here are the main results of the thesis.

6.5.1 State preparation - heralding

We found that the qubits had 5%-8% probability to be in the excited state when idling. To remove this initialization error from characterization of the measurement process, we use heralding [13]. Each pulse sequence begins with a measurement pulse, and only those experimental repetitions in which this first measurement pulse yields $|0\rangle$ are kept. In this way, we effectively force the qubit into $|0\rangle$ at the start of each pulse sequence. This heralding process brought the $|0\rangle$ preparation probability to $> 99.3\%$, as we will see below.

6.5.2 Fidelity at fixed measurement time

Preparing the qubit into either $|0\rangle$ or $|1\rangle$, we inject a measurement pulse and digitize the scattered wave. We kept trials for which demodulation of the heralding pulse yielded $|0\rangle$. We then demodulated the measurement signal for 140 ns, beginning at the start of the measurement pulse when there were nearly zero photons in the resonator. This yielded two sets of IQ points, one for $|0\rangle$ and one for $|1\rangle$ as shown in Fig. 6.7. As predicted in Ch. 3, the demodulated IQ

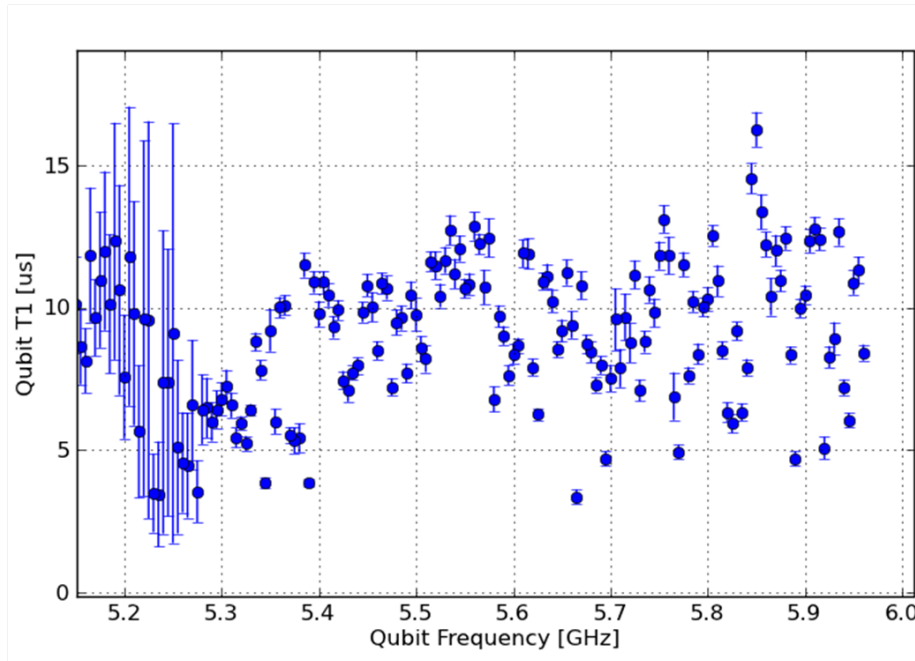


Figure 6.6: Energy decay time T_1 versus frequency for qubit Q_2 . With the measurement resonator frequency above the qubit, the lack of downward trend in T_1 with increasing qubit frequency indicates that the measurement circuit does not dominate the qubit damping. The T_1 values are distributed around $10\ \mu\text{s}$, which is several times larger than the Purcell limit predicted in the absence of the filter. The dip and wild variation in T_1 5.2 GHz come from coupling to a resonator bus which was not used in this experiment.

points form two dimensional Gaussian distributions. The finite separation and width of the distributions means that, with a single IQ measurement, we have a probability of erroneously identifying the qubit state. We characterize the error in two ways: first using just the intrinsic signal to noise ratio of the dispersed photons, and second including non-ideal behavior of the qubit.

Separation error

We first characterize errors from the intrinsic signal to noise ratio of the dispersed photons. This is captured by the separation error ϵ_{sep} defined in Ch. 3. Projecting the two dimensional IQ distributions onto the line connecting their centers produces a pair of one dimensional Gaussian distributions, as shown in the inset of Fig. 6.7. We find that the distributions are well fit by parabolas on the log scale, indicating good Gaussian shape. From the fits, we compute ϵ_{sep} using Eq. (3.32). Here, we found $\epsilon_{\text{sep}} = 0.2\%$.

State errors

In the histogram shown in the inset of Fig. 6.7, we can see bins with counts greatly exceeding the parabolic fit. For example, there are far more red counts at $x = -1$ than predicted by the red fit line. These counts come from repetitions in which the qubit undergoes a state transition event before or during the measurement pulse. A simple example is a qubit which undergoes a T_1 decay event near the beginning of the measurement pulse. After the T_1 decay, the qubit is in $|0\rangle$, so the measured IQ point may be deep within the $|0\rangle$ cloud, but because that qubit was prepared as $|1\rangle$, we mark it as red. Other sources of this type of error are $|0\rangle \rightarrow |1\rangle$ qubit transitions, improperly prepared states due to the finite accuracy of the heralding measurement pulse, and transitions induced by the measurement pulse itself. We define the “state errors” $\epsilon_{|0\rangle}$ ($\epsilon_{|1\rangle}$) as the probability that a qubit nominally prepared in $|0\rangle$ ($|1\rangle$) is incorrectly identified. We find $\epsilon_{|0\rangle} = 0.7\%$ and $\epsilon_{|1\rangle} = 1.3\%$. These state errors are just at the $\sim 1\%$ threshold needed for the surface code. Larger qubit T_1 values, accessible through use of MBE grown aluminum films [19] would improve $\epsilon_{|1\rangle}$.

6.5.3 Time dependence

While separation fidelity is improved by collecting more scattered photons, this requires longer measurement and thus incurs more qubit errors. To fully characterize this trade-off, we varied the upper limit of the time integration used in extracting the IQ points, thus building a time series of $|0\rangle$ and $|1\rangle$ IQ clouds. We plot the data in three dimensions, with time on the z-axis and with each x-y plane representing an IQ plane at a single time. An example with the qubit prepared in $|0\rangle$, $|1\rangle$, and $|2\rangle$ is shown in Fig. 6.8. Each thread in the plot corresponds to a single repetition of the experiment, ie. a single measurement event. At the beginning of the measurement pulse $t = 0$, the branches for the three prepared states are indistinguishable. At the beginning of the pulse, photons

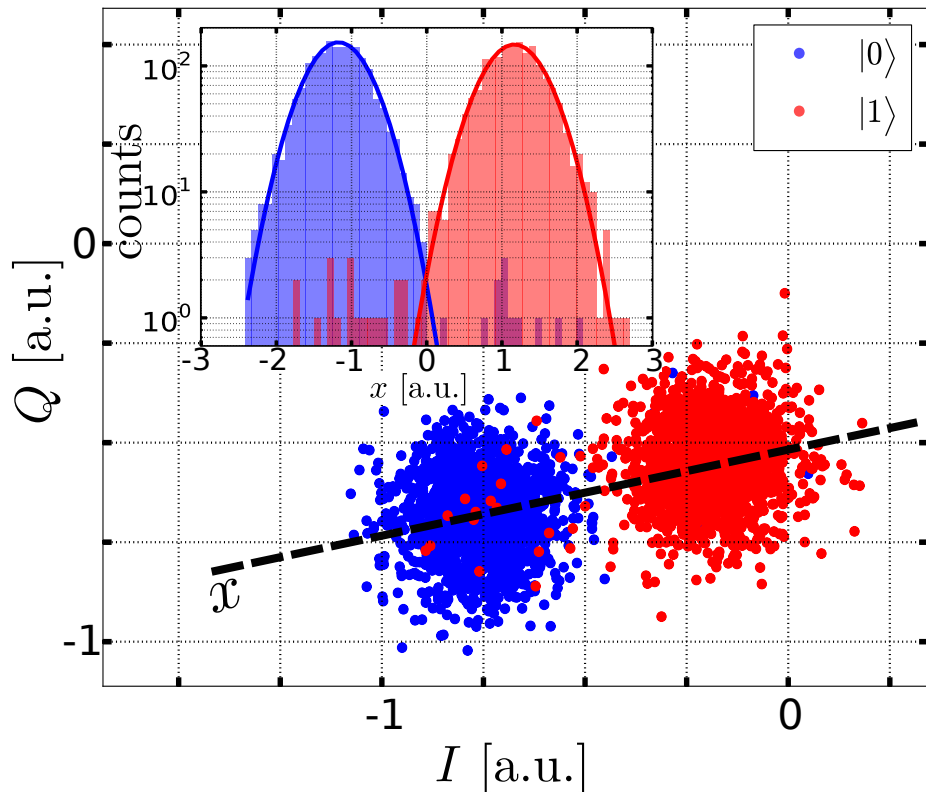


Figure 6.7: Measurement events for one qubit after 140 ns pulse integration. Points in the wrong cluster are due to unwanted qubit state transitions. The appearance of more red points in the blue cluster than blue points in the red cluster is partially an artefact of the plot, and partially due to the fact that the qubit undergoes more downward transitions than upward transitions. The inset shows histograms of the IQ points projected onto the line connecting the centers of the $|0\rangle$ and $|1\rangle$ clouds. Heavy lines are Gaussian fits to the histograms are used for computing the separation error.

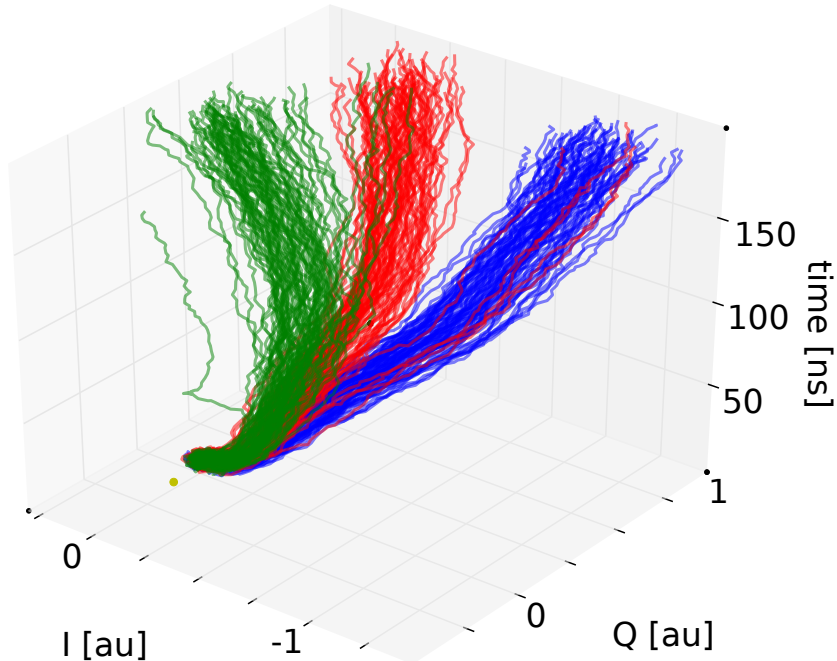


Figure 6.8: IQ trajectories during integration of the measurement pulse, showing approximately 150 separate measurements. The three branches correspond to the qubit prepared in the $|0\rangle$ (blue), $|1\rangle$ (red), or $|2\rangle$ (green) states. Note the green threads which jump to the red branch part way through the measurement, which represent $|2\rangle \rightarrow |1\rangle$ qubit transitions.

begin to be collected, but the resonator has not yet rung up, so the photons are not phase shifted. During this time, the branches all move away from their starting position but remain clustered. Once the resonator has rung up, the scattered photons carry information about the qubit state, and the branches begin to separate. Integrating more signal and noise increases the separation and the widths of the branches.

Next, we find the time dependent separation and state errors. For each time slice during the measurement we construct IQ clouds as in Fig. 6.7. Once we recorded the time domain traces $I(t)$ and $Q(t)$, we extracted the time dependent separation error $\epsilon_{\text{sep}}(t)$ at each t in the same way as described above. We then used the separation $\delta(t) \equiv |\langle I(t) \rangle - \langle Q(t) \rangle|$ as an optimal weighting window to re-integrate the data. In other words, once we knew $\delta(t)$ we multiplied $I(t)$ and $Q(t)$ by $\delta(t)$ and re-integrated. This emphasized the data where the IQ clouds for each state are better separated. From the re-integrated data we extract ϵ_{sep} , $\epsilon_{|0\rangle}$, and $\epsilon_{|1\rangle}$. We wish to build a multiplexed system capable of measuring

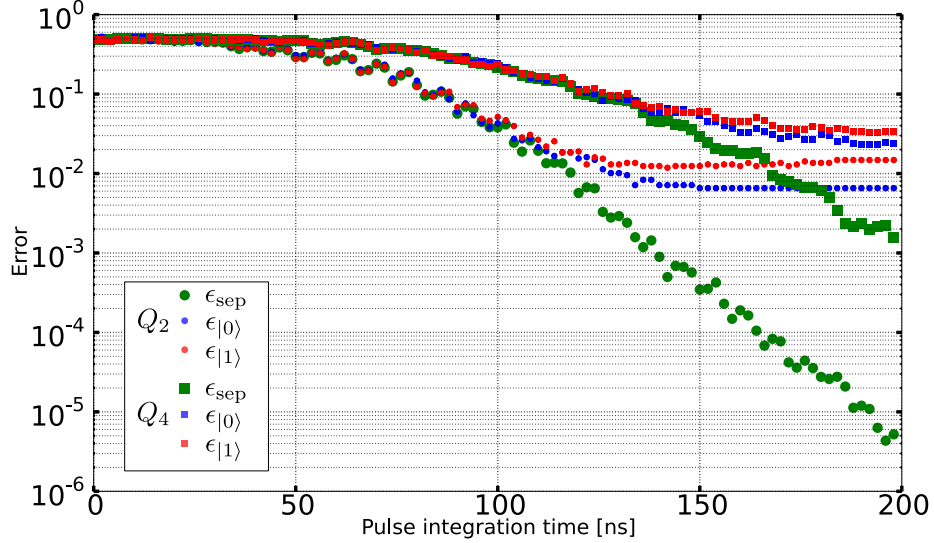


Figure 6.9: Time dependence of measurement errors for qubits Q_2 (circles) and qubit Q_4 (squares) measured simultaneously. Green points indicate the separation error ϵ_{sep} , while the blue and red points represent $\epsilon_{|0\rangle}$ and $\epsilon_{|1\rangle}$ respectively. The data in Fig. 6.7 came from the $t = 140$ ns point for Q_2 .

several qubits simultaneously, so we performed the experiment on two qubits, Q_2 and Q_4 at the same time, as shown in Fig. 6.9.

We focus first on the data for qubit Q_2 . The separation error changes slowly with time for the first 50 ns while the resonator rings up. As shown in Fig. 6.3, the resonator photon occupation reaches the maximum value after approximately 50 ns. As the resonator photon number increases, the slope of $\epsilon_{\text{sep}}(t)$ increases until attaining a constant value at about 125 ns of approximately one decade per 25 ns. The constant slope on the semi-log scale is consistent with Eq. (3.35).

The state errors decrease along with the separation error for the first 100 ns, and then begin to saturate. The saturation is explained by two deleterious qubit state transition processes. We have measured that, in equilibrium, the qubits experience upward $|0\rangle \rightarrow |1\rangle$ transitions with a rate of $\Gamma_\uparrow \approx 1/100 \mu\text{s}$, which result in excited state populations of 5% to 8%. These transitions lead to state preparation errors; with 500 ns between the heralding and final measurements, we expect 0.5% re-population of the excited state before the start of the final measurement. This nearly explains the saturation of $\epsilon_{|0\rangle}$ at 99.3%. The second error process is the usual qubit energy relaxation; a qubit transition before the halfway point of the measurement leads to an error. With a measurement time of 140 ns and $T_1 = 10 \mu\text{s}$ we expect an extra 0.7% loss in excited state population, yielding an expected limit of 98.8%. This agrees well with the measured $\epsilon_{|1\rangle}$ saturation at 98.7%.

The separation fidelity for Q_4 is qualitatively similar to the data for Q_2 , but with slower approach to the constant slope region. Qubit Q_4 is slower because it has $\kappa_r^{-1} = 147$ ns, which is slower for Q_2 where $\kappa_r^{-1} = 37$ ns.

These data demonstrate the viability of multiplexed, dispersive state measurement. In particular, the qubit with fast κ_r approaches 99% accuracy for the state errors in this multiplexed measurement.

As the more aggressive κ_r used in qubit Q_2 did not produce a measurable suppression in T_1 , future designs should use even faster values of κ_r . The qubit with the most aggressive κ_r in the present experiment, Q_1 , could not be carefully characterized because of the error which placed Q_3 's measurement resonator too close in frequency to Q_1 's measurement resonator.

6.5.4 Multiplexed measurement

We measured all four qubits simultaneously, as shown in Fig. 6.10. Three of the four qubits, Q_1 , Q_2 , and Q_3 , reached $\epsilon_{\text{sep}} < 1\%$ within 200 ns. The fourth device, Q_4 , which had the most conservative $\kappa_r T_1$ product, reached $\epsilon_{\text{sep}} = 1\%$ in 266 ns. In order to prevent saturation of the parametric amplifier while simultaneously measuring all four devices, we reduced the drive powers relative to the two qubit case discussed previously. This lead to lower SNR and accordingly required longer integration time, which is why the time for eg. Q_2 to reach $\epsilon_{\text{sep}} = 1\%$ is longer here than in Fig. 6.9.

For qubits Q_2 and Q_4 the performance is nearly as good as for the two qubit case. The small degradation of performance comes from increased qubit transitions during the longer measurement time. Qubits Q_1 and Q_3 show higher $\epsilon_{|1\rangle}$. As shown in the inset of Fig. 6.1 the measurement resonators for qubits Q_1 and Q_3 are closely spaced in frequency (13 MHz). This close spacing adversely affects the frequency discrimination step of the measurement via spectral leakage, leading to increased measurement error. This is seen in Fig. 6.10 where the $\epsilon_{\text{sep}}(t)$ for Q_3 does not follow a line on the semi-log plot. More importantly, the measurement photons induce large qubit frequency shifts (200 MHz to 300 MHz) via the ac Stark effect, as shown in Fig. 6.3. This causes the qubits to cross through resonance with material defects and lose $|1\rangle$ population. This was the main cause of the poor $\epsilon_{|1\rangle}$ on Q_1 . We were able to mostly work around this problem with careful choice of operating frequency in qubits Q_2 , Q_3 , and Q_4 , but limited total available frequency space led to degraded performance in Q_1 which was tuned up last. This problem would be substantially mitigated in devices constructed with epitaxial Al films grown on plasma cleaned substrates as, this was shown to significantly reduce the number and coupling strengths of the defects [19].

6.6 Measurement efficiency

If scattered photons are lost through absorption, or if the parametric or HEMT amplifiers add noise to the scattered signal, the measurement performance de-

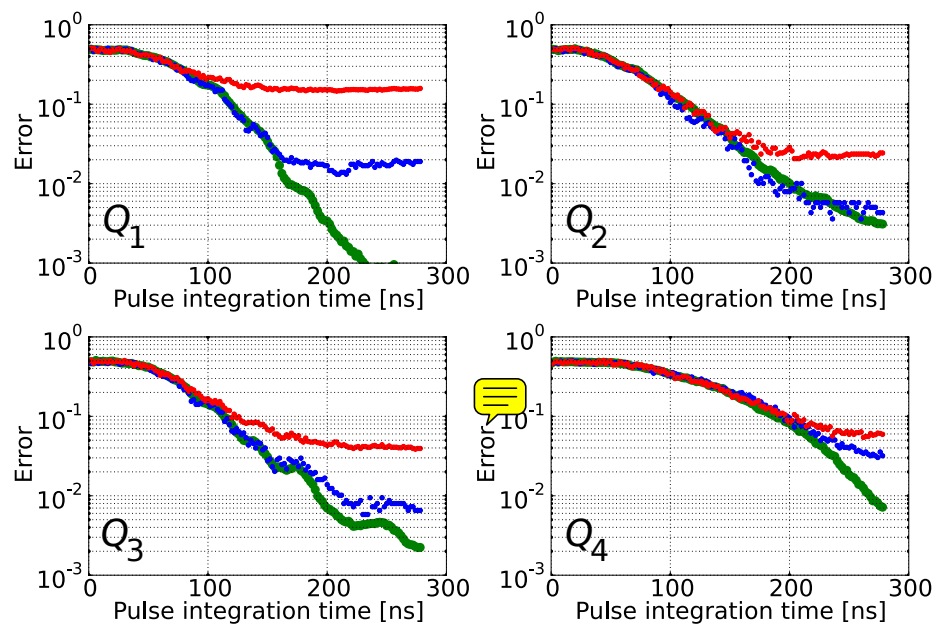


Figure 6.10: Simultaneous measurement of four qubits. Separation (green) and state (blue and red) fidelities are shown similarly to Fig. 6.9. Ripples on qubits Q_1 and Q_3 were caused by spectral leakage.

grades. We characterized these imperfections by comparing the effect of the measurement photons on the qubit against the resulting measurement visibility.

In Chapter 3 we found a relation between the measurement SNR, and the associated qubit dephasing. For a given measurement pulse power, if the measurement visibility is less than that predicted by Eq. (3.43), we would conclude that some of the scattered photons must have been lost, or additional noise must have been injected into the processing chain. In one experiment, we measured the photon induced qubit dephasing via Ramsey fringes, where we added a variable power measurement pulse between the usual two π -pulses in the standard Ramsey sequence. This measurement pulse dephases the qubit and lowers the visibility of the Ramsey fringes. We record the resulting fringe visibility as a function of measurement pulse power. In a second experiment, we prepare the qubit in either $|0\rangle$ or $|1\rangle$ and then apply a measurement pulse, recording the SNR as a function of pulse power. We then convert SNR to an upper bound on phase coherence via Eq. (3.43).

We extract the system efficiency by comparing the directly measured Ramsey visibility against the quantum limit implied from the second experiment, as shown in Fig. 6.11. We found that the Ramsey visibility curve is shifted 9 dB to the left of the quantum limit curve, indicating that our measurement system has a quantum efficiency of $\eta = -9 \text{ dB} \approx 12\%$.

Quantum efficiency less than 1 comes from photon loss and/or added noise, so we attempt to budget this -9 dB efficiency in terms of lossy hardware elements and known noise sources in the experiment. At least 3 dB efficiency loss comes from the parametric amplifier, as a phase insensitive parametric amplifier adds an input referred noise of $\hbar\omega_r/2$ noise power per unit bandwidth [9]. The photon states themselves carry $\hbar\omega_r/2$ quantum noise power per unit bandwidth, so the parametric amplifier degrades the signal to noise ratio by at least a factor of 2 = 3 dB.

The remaining 6 dB must come from a combination of other noise sources and photon loss. Referring back to the diagram of the experimental apparatus shown in Fig. 5.1, we find a large number of microwave elements, each of which contributes some loss. The IR filter itself is known to have approximately 2 dB loss at our measurement frequencies near 7 GHz. The three circulators are expected to contribute a total of ~ 1 dB loss. The dispersed signal makes roughly 20 trips through SMA connectors. With 0.03 dB specified insertion loss per SMA connector, assuming the insertion loss really is a loss, the connectors contribute at least another 0.5 dB loss. The HEMT amplifier adds noise. We operated with parametric amplifier gain near 16 dB, which results in an effective output noise temperature of $T = 10^{16/10} h\nu/k_b \approx 13$ Kelvin. This is about 5 times higher than the HEMT noise temperature of ~ 2.5 Kelvin, resulting in another 1 dB of noise added by the HEMT.

With these considerations we have approximately 1.5 dB loss or added noise unaccounted for, which corresponds to 70% efficiency. This extra efficiency loss could be carefully studied in further experiments.

Without precise measurements of the loss of each hardware element, it is difficult to estimate the uncertainty of the numbers discussed above. However,

the SMA connectors deserve special attention. The insertion loss of an SMA connector does not necessarily come from a dissipative processes; non-zero reflections from the input contribute to insertion loss. Therefore, our assumption that the collective insertion losses of the 20 SMA connectors add together is not necessarily well founded. Ignoring the SMA connector insertion loss, we compute 2.0 dB loss or added noise unaccounted for.

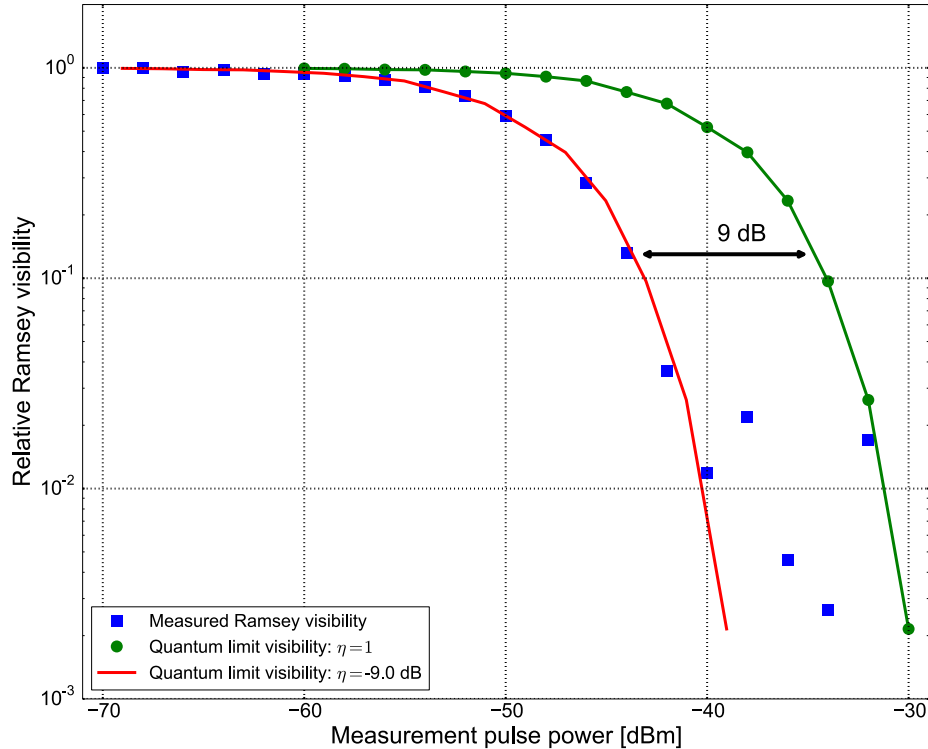


Figure 6.11: Quantum efficiency of the measurement system. Performing a standard Ramsey fringe sequence, but with a measure pulse in between the $\pi/2$ -pulses, we measure the relative fringe visibility as a function of measure pulse power (blue squares). The fringe visibility data becomes noisy at visibilities $< 3\%$. We also measure the distinguishability between the qubit states versus measure pulse power, and convert to a quantum limit on Ramsey fringe visibility via Eq. (3.43) (green circles). The comparison between these curves is clarified by re-plotting the quantum limit shifted by 9 dB (red line), which goes through the Ramsey visibility points.

Appendix A

Quantum Mechanics Reference

A.1 Commutators

A.1.1 Products

$$[A, BC] = ABC - BCA \quad (\text{A.1})$$

$$= ABC - BAC + BAC - BCA \quad (\text{A.2})$$

$$= [A, B]C + B[A, C]. \quad (\text{A.3})$$

This can be remembered by noting that $[A, \cdot]$ is like a derivative with respect to A .

A.1.2 Translation by an operator

A very common expression involves the translation of an operator A by another operator B . The translation can be expressed as a sum

$$e^A B e^{-A} = \sum_{n=0}^{\infty} \frac{1}{n!} \underbrace{[A, [A, [A, \dots [A, B]]]]}_{n \text{ times}}. \quad (\text{A.4})$$

We can also derive a differential equation that helps in evaluating this sort of expression. Define

$$\mathcal{O}(\lambda) = e^{\lambda A} B e^{-\lambda A}. \quad (\text{A.5})$$

Differentiating both sides with respect to λ gives

$$\frac{d\mathcal{O}}{d\lambda} = [A, \mathcal{O}(\lambda)]. \quad (\text{A.6})$$

It is sometimes useful to solve equation (A.6) and then set $\lambda = 1$ instead of evaluating (A.4) directly.

A.1.3 Baker-Campbell-Hausdorff

The BCH formula provides a summation representation of the product of two exponentiated operators,

$$e^A e^B = e^{A+B+\frac{1}{2}[A,B]+\frac{1}{12}([A,[A,B]]-[B,[A,B]])+\dots}. \quad (\text{A.7})$$

A.1.4 Conjugate Variables

Two operators α and β are “conjugate” if they have the commutator

$$[\alpha, \beta] = \eta \quad (\text{A.8})$$

where η is a complex number. If an operator A is normal ordered (all α 's to the left of all β 's) then we have the following extremely useful formulae,

$$[\alpha, A] = \eta \frac{\partial A}{\partial \beta} \quad \text{and} \quad [\beta, A] = -\eta \frac{\partial A}{\partial \alpha} \quad (\text{A.9})$$

Conjugate variables also have a very simple translation property

$$e^{i\hat{\alpha}} \hat{\beta} e^{-i\hat{\alpha}} = \hat{\beta} + i\eta. \quad (\text{A.10})$$

A.2 Pauli operators

A.2.1 Representation

The Pauli operators can be represented as

$$\sigma_x = \begin{pmatrix} 0 & 1 \\ 1 & 0 \end{pmatrix} \quad (\text{A.11})$$

$$\sigma_y = \begin{pmatrix} 0 & -i \\ i & 0 \end{pmatrix} \quad (\text{A.12})$$

$$\sigma_z = \begin{pmatrix} 1 & 0 \\ 0 & -1 \end{pmatrix} \quad (\text{A.13})$$

A.2.2 Products and commutators

The Pauli operators anticommute

$$\sigma_i \sigma_j = -\sigma_j \sigma_i \quad (i \neq j) \quad (\text{A.14})$$

and have a convenient product property

$$\sigma_i \sigma_j = i \epsilon_{ijk} \sigma_k. \quad (\text{A.15})$$

From the product and anticommutation follows the commutation relation

$$[\sigma_i, \sigma_j] = 2i \epsilon_{ijk} \sigma_k. \quad (\text{A.16})$$

A.2.3 Translation

The problem of translating one Pauli operator by another arises frequently when analyzing qubit systems. We wish to evaluate

$$S(Q) = e^{-iQ\sigma_i} \sigma_j e^{iQ\sigma_i}. \quad (\text{A.17})$$

We use the differential equation (A.6) with $A = -iQ\sigma_i$ to get

$$\frac{dS}{dQ} = i[S(Q), \sigma_i]. \quad (\text{A.18})$$

We postulate the solution

$$S(Q) = \alpha(Q)\sigma_j + \beta(Q)\sigma_k. \quad (\text{A.19})$$

First work out the commutator $i[S(Q), \sigma_i]$

$$\begin{aligned} i[S(Q), \sigma_i] &= i[\alpha\sigma_j + \beta\sigma_k, \sigma_i] \\ &= i(-2i\alpha\sigma_k + 2i\beta\sigma_j) \\ &= 2\alpha\sigma_k - 2\beta\sigma_j. \end{aligned}$$

Equating the right hand side with the explicit derivative of S yields

$$\dot{\alpha}(Q) = -2\beta(Q) \quad \dot{\beta}(Q) = 2\alpha(Q)$$

with solution

$$\alpha(Q) = \cos(2Q) \quad \beta(Q) = \sin(2Q).$$

Therefore

$$e^{-iQ\sigma_i} \sigma_j e^{iQ\sigma_i} = \cos(2Q) \sigma_j + \sin(2Q) \sigma_k. \quad (\text{A.20})$$

A.3 Rotating Frame

The basic qubit Hamiltonian is

$$H_q/\hbar = -\frac{\omega_q}{2}\sigma_z \quad (\text{A.21})$$

A quantum state under this Hamiltonian precesses around the Z axis. In the lab we are used to thinking about a rotating frame in which this precession is absent. We now show how do we do this mathematically.

In the Schrodinger picture the time evolution operator for a Hamiltonian H_0 is

$$T = \exp\left[-\frac{i}{\hbar}H_0t\right]. \quad (\text{A.22})$$

Intuitively, we should just apply the inverse of this evolution to the Schrodinger state vector in order to remove the precession. We can then define a state in the rotating frame as

$$|\Psi'(t)\rangle = R|\Psi(t)\rangle \quad (\text{A.23})$$

where $R = T^\dagger$. Computing the time evolution of this new state we get

$$i\hbar\partial_t|\Psi'(t)\rangle = i\hbar\dot{R}|\Psi(t)\rangle + Ri\hbar\partial_t|\Psi(t)\rangle \quad (\text{A.24})$$

$$= i\hbar\dot{R}R^\dagger|\Psi'(t)\rangle + RH_0R^\dagger|\Psi'(t)\rangle \quad (\text{A.25})$$

$$= \left(i\hbar\dot{R}R^\dagger + RH_0R^\dagger \right) |\Psi'(t)\rangle. \quad (\text{A.26})$$

This can be interpreted as a Schrodinger equation for a system with Hamiltonian

$$H'_0 = i\hbar\dot{R}R^\dagger + RH_0R^\dagger. \quad (\text{A.27})$$

Note that this result is correct for *any* R , not necessarily inverse of the Schrodinger evolution operator.

In the case that $R = T^\dagger$ the resulting Hamiltonian is particularly simple, as expected

$$H'_0 = i\hbar(iH_0/\hbar)RR^\dagger + H_0 \quad (\text{A.28})$$

$$= 0. \quad (\text{A.29})$$

Here we used the fact that R , like T is unitary, and that $\partial_t T = -i(H_0/\hbar)T$. The point is that if we rotate the frame at the same rate as the Hamiltonian was rotating the states, the effective Hamiltonian becomes zero.

An extremely important fact to note is that if we take the rotation operator R to be the inverse of the time translation operator induced by the original Hamiltonian, then the effect on any other perturbation or coupling terms V is $V \rightarrow RVR^\dagger = T^\dagger VT$, which is identical to the transformation found in the interaction picture.

Appendix B

Quantum Oscillator Reference

In this appendix we list basic results of the quantum harmonic oscillator. Although this problem is treated in many textbooks, some useful formulae, such as the zero point fluctuations, and useful derivatives with respect to the raising and lowering operators, are frequently neglected.

B.1 General Form

The general form of the Hamiltonian for a harmonic oscillator is

$$H = \frac{1}{2}\alpha u^2 + \frac{1}{2}\beta v^2 \quad [u, v] = i\gamma. \quad (\text{B.1})$$

Using dimensionless operators

$$X \equiv \frac{1}{\sqrt{\gamma}} \left(\frac{\alpha}{\beta} \right)^{1/4} u \quad \text{and} \quad Y \equiv \frac{1}{\sqrt{\gamma}} \left(\frac{\beta}{\alpha} \right)^{1/4} v \quad (\text{B.2})$$

we get a new form of the Hamiltonian

$$H = \gamma \sqrt{\alpha\beta} \frac{1}{2} [X^2 + Y^2] \quad [X, Y] = i. \quad (\text{B.3})$$

We also introduce raising and lowering operators a and a^\dagger defined by the following equations

$$\begin{aligned} a &= \frac{1}{\sqrt{2}}(X + iY) & a^\dagger &= \frac{1}{\sqrt{2}}(X - iY) \\ X &= \frac{1}{\sqrt{2}}(a + a^\dagger) & Y &= \frac{-i}{\sqrt{2}}(a - a^\dagger) \end{aligned} \quad (\text{B.4})$$

with commutator

$$[a, a^\dagger] = 1. \quad (\text{B.5})$$

Writing down the expression for $a^\dagger a$ and expanding it in terms of the X and Y operators, we find

$$\begin{aligned} \gamma\sqrt{\alpha\beta}(a^\dagger a) &= \gamma\sqrt{\alpha\beta}\frac{1}{2}(X - iY)(X + iY) \\ &= \gamma\sqrt{\alpha\beta}\frac{1}{2}(X^2 + iXY - iYX + Y^2) \\ &= \gamma\sqrt{\alpha\beta}\frac{1}{2}(X^2 + Y^2 + i[X, Y]) \\ &= \gamma\sqrt{\alpha\beta}\frac{1}{2}(X^2 + Y^2 - 1) \\ &= H - \frac{1}{2}\gamma\sqrt{\alpha\beta} \\ \text{so } H &= (a^\dagger a + \frac{1}{2})\gamma\sqrt{\alpha\beta}. \end{aligned}$$

It will be shown below from Heisenberg's equations of motion that

$$\hbar\omega = \gamma\sqrt{\alpha\beta} \quad (\text{B.6})$$

which means that the Hamiltonian can be written as

$$H = \hbar\omega \left(a^\dagger a + \frac{1}{2} \right). \quad (\text{B.7})$$

B.1.1 Zero point fluctuation

It's now easy to compute that

$$\langle u^2 \rangle_0 = \frac{1}{2}\gamma\sqrt{\beta/\alpha} \quad \langle v^2 \rangle_0 = \frac{1}{2}\gamma\sqrt{\alpha/\beta} \quad (\text{B.8})$$

and

$$\langle X^2 \rangle_0 = \langle Y^2 \rangle_0 = 1/2 \quad (\text{B.9})$$

Defining $u_{\text{zpf}}^2 \equiv \langle u^2 \rangle_0$ we have

$$X = \frac{1}{\sqrt{2}} \frac{u}{u_{\text{zpf}}} \quad Y = \frac{1}{\sqrt{2}} \frac{v}{v_{\text{zpf}}} \quad (\text{B.10})$$

B.2 Algebra

From the commutator $[a, a^\dagger] = 1$ it follows that [31]

$$[a, T] = \frac{\partial T}{\partial a^\dagger} \quad [a^\dagger, T] = -\frac{\partial T}{\partial a} \quad (\text{B.11})$$

as long as T is written in normal order form (all a^\dagger operators to the left of all a operators). This is extremely useful when computing dynamics in the Heisenberg or interaction picture, as will be shown in the next section.

B.3 Equations of Motion

The Heisenberg equation of motion for the a operator is

$$\begin{aligned} i\hbar d_t a &= [a, H] \\ &= \gamma\sqrt{\alpha\beta}[a, a^\dagger a + \frac{1}{2}] \\ &= \gamma\sqrt{\alpha\beta}\frac{\partial(aa^\dagger)}{\partial a^\dagger} \\ &= \gamma\sqrt{\alpha\beta}a \end{aligned}$$

giving

$$\dot{a} = -i\frac{\gamma\sqrt{\alpha\beta}}{\hbar}a. \quad (\text{B.12})$$

Solving this simple differential equation yields

$$a(t) = a(0) \exp[-i\omega t] \quad \text{and} \quad a^\dagger(t) = a^\dagger(0) \exp[i\omega t]. \quad (\text{B.13})$$

where $\omega \equiv \gamma\sqrt{\alpha\beta}/\hbar$ as claimed above. Note that the evolution of a in the phase plane is *clockwise*, ie. the phasor convention we inherit from Schrodinger's (Heisenberg's) equation has a $-i$. This is important interpreting the meaning of positive and negative energy in a quantum calculation.

Appendix C

IQ Mixer

C.1 Modulation

When an IQ mixer is used for modulation (up-conversion) a carrier tone is put into the LO port, and modulating signals are put into the I and Q ports. The input tone $\cos(\Omega t)$ is multiplied by the I channel, a quarter cycle phase shifted copy of the tone $-\sin(\Omega t)$ is multiplied by the Q channel, and then both results are summed and put out the RF port.

Consider a case where $I = \cos(\omega t + \phi)$ and $Q = \sin(\omega t + \phi)$. The output of the device is then

$$\begin{aligned} s(t) &= \cos(\Omega t) \cos(\omega t + \phi) - \sin(\Omega t) \sin(\omega t + \phi) \\ &= \frac{1}{2} [\cos([\Omega + \omega]t + \phi) + \cos([\Omega - \omega]t - \phi) \dots \\ &\quad + \cos([\Omega + \omega]t + \phi) - \cos([\Omega - \omega]t - \phi)] \\ &= \cos([\Omega + \omega]t + \phi) \end{aligned} \tag{C.1}$$

Think of the incoming I and Q channels as coordinates in an IQ plane. In this picture the inputs we chose form a counter-clockwise rotating circle with frequency ω and phase ϕ . As we've computed, this counter-clockwise rotating circle produces a positively detuned sideband at the output of the mixer. The rotation rate of the input IQ signal translates directly to the detuning of the output signal away from the carrier, and the phase of the input circle translates directly to the phase of the output signal. In fact this observation leads us to a really convenient way to remember this result. If we treat the IQ plane as a complex number plane, then the trajectory of our counter-clockwise moving point can be written simply as

$$z_{IQ}(t) = \exp[i(\omega t + \phi)] \tag{C.2}$$

Then, to recover the output signal, we just multiply by $\exp[i\Omega t]$ and take the

real part,

$$z(t) \exp[i\Omega t] = \exp[i(\omega t + \phi)] \exp[i\Omega t] \quad (\text{C.3})$$

$$z(t) \exp[i\Omega t] = \exp[i(\Omega + \omega)t + i\phi] \quad (\text{C.4})$$

$$\operatorname{Re}(z(t) \exp[i\Omega t]) = \cos[(\Omega + \omega)t + \phi] \quad (\text{C.5})$$

From equation (C.1) you can see that if we reverse the orientation of our rotating signal by setting $Q = -\sin(\omega t + \phi)$, the output would have been negatively detuned, and would have had a negative phase shift. This is consistent with our complex representation: the clockwise rotating signal $\cos[\omega t + \phi] - \sin[\omega t + \phi]$ has complex representation $z(t) = \exp[-i(\omega t + \phi)]$. Multiplying by $\exp[i\Omega t]$ and taking the real part gives $\cos[(\omega - \omega)t - \phi]$, which is the correct real signal.

In summary, if we view the inputs to the I and Q ports of an IQ mixer as real and imaginary coordinates, then the map between the input and the output signals is

$$\exp[i(\omega t + \phi)] \rightarrow \cos[(\Omega + \omega)t + \phi] \quad (\text{C.6})$$

C.2 Demodulation to baseband

Consider a high frequency signal $s(t) = \cos[(\Omega + \omega)t + \phi]$ coming into the RF port of an IQ mixer. Into the LO port we put $\cos(\Omega t + \delta)$. If we filter away the high frequency part of the outputs, the output of the I port is

$$\begin{aligned} I(t) &= \cos[(\Omega + \omega)t + \phi] \cos[\Omega t + \delta] \\ &= \frac{1}{2} (\cos[(2\Omega + \omega)t + \phi + \delta] + \cos[\omega t + \phi - \delta]) \\ &= \frac{1}{2} \cos[\omega t + \phi - \delta] \end{aligned} \quad (\text{C.7})$$

Similarly the Q port output is

$$\begin{aligned} Q(t) &= \cos[(\Omega + \omega)t + \phi] (-1) \sin[\Omega t + \delta] \\ &= \frac{1}{2} (\sin[(2\Omega + \omega)t + \phi + \delta] + \sin[\omega t + \phi - \delta]) \\ &= \frac{1}{2} \sin[\omega t + \phi - \delta] \end{aligned} \quad (\text{C.8})$$

These signals can be thought of as the real and imaginary parts of a complex signal

$$z(t) = \exp[i(\omega t + \phi - \delta)] \quad (\text{C.9})$$

$$I(t) = \frac{1}{2} \operatorname{Re} z(t) \quad Q(t) = \frac{1}{2} \operatorname{Im} z(t) \quad (\text{C.10})$$

Note that the phase of the complex signal is the difference between the phase of the high frequency signal and the phase of the local oscillator. Conveniently,

we we think of the incoming high frequency signal as the real part of a complex signal

$$z_{\text{hf}} = \text{Re} \exp [i(\Omega + \omega)t + \phi] \quad (\text{C.11})$$

and the action of the demodulating IQ mixer, plus the low pass filtering, can then be written as multiplication by $\exp[-i(\Omega t + \delta)]$.

In summary, when a high frequency signal at frequency $\Omega + \omega$ and phase ϕ is demodulated by an IQ mixer with an LO signal of frequency Ω and phase δ , the I and Q outputs are given by the real and imaginary parts of

$$\begin{aligned} z(t)_{\text{demod}} &= \underbrace{\exp[-i(\Omega t + \delta)]}_{\text{effect of mixer}} \underbrace{\exp[i(\Omega + \omega)t + i\phi]}_{\text{incoming signal}} \\ &= \exp[i(\omega t + \phi - \delta)] \end{aligned}$$

C.3 Demodulation to DC

Now that we have baseband I and Q signals we want to extract the phase and amplitude of the original high frequency signal. Symbolically what we would like to do is multiply our complex baseband signal by $\exp[-i\omega t]$ and integrate. The result would be a complex number $A \exp[i(\phi - \delta)]$ with amplitude proportional amplitude of the original signal. Of course, we can't produce complex numbers in real life, but if we work out the real and imaginary parts we can figure out how to emulate the complex algebra by effecting two separate real signal processes.

First express the complex representation of the IF signal in terms of $I(t)$ and $Q(t)$

$$z(t) = I(t) + iQ(t). \quad (\text{C.12})$$

Multiplying by the desired exponential gives

$$\begin{aligned} z(t) \exp(-i\omega t) &= \\ &\quad I(t) \cos(\omega t) + Q(t) \sin(\omega t) \\ &\quad + i[-I(t) \sin(\omega t) + Q(t) \cos(\omega t)] \end{aligned} \quad (\text{C.13})$$

From this expression we can see that the final I and Q coordinates are given by

$$I = \sum I(t) \cos(\omega t) + Q(t) \sin(\omega t) \quad (\text{C.14})$$

$$Q = \sum Q(t) \cos(\omega t) - I(t) \sin(\omega t) \quad (\text{C.15})$$

There are thus four integrals that have to be done in the FPGA board to compute the IQ result. Note that since each signal is multiplied and summed with either sine or cosine the data flow can be greatly simplified in the software. In other words, there are four integrals to do, but only two digital functions to generate ¹.

¹In fact we can use the same lookup table to generate the sine and cosine by offsetting one quarter cycle in the table

C.4 Demodulation Mixer Imbalance

What happens if the demodulating mixer has imbalance in the power coming from the I and Q ports? In that case we would get something like

$$I(t) = C \cos(\omega t) \quad Q(t) = S \sin(\omega t) \quad (\text{C.16})$$

with $C \neq S$. These cannot be represented as the real and imaginary parts of a single exponential. They can be written as the real and imaginary parts of

$$A_1 \exp[\omega t] + A_2 \exp[-\omega t] \quad (\text{C.17})$$

as long as

$$A_1 + A_2 = C \quad A_1 - A_2 = S \quad (\text{C.18})$$

This means that in a system with imbalanced I and Q ports we will measure false peaks at frequencies mirrored about the carrier from the real signal.

Appendix D

Formal Theory of Superconducting Qubits

D.1 Introduction - Parallel LC

Consider a parallel LC circuit as shown in Fig. D.1. From Kirchoff's laws the equation of motion can be found to be

$$\ddot{\Phi} + \omega_0^2 \Phi = 0 \quad (\text{D.1})$$

where $\omega_0 = 1/\sqrt{LC}$. This equation of motion is reproduced by the Lagrangian¹

$$L = \frac{1}{2}C\dot{\Phi}^2 - \frac{1}{2L}\Phi^2 \quad (\text{D.2})$$

where Φ is the flux through the inductor. The momentum conjugate to the flux Φ is

$$p = \frac{\partial L}{\partial \dot{\Phi}} = C\dot{\Phi}. \quad (\text{D.3})$$

Since $\dot{\Phi}$ is just the voltage across the LC circuit, the canonical momentum p is just the charge Q on the capacitor. Therefore, Φ and Q are so-called canonically conjugate variables.

The Hamiltonian of the system is

$$H = p\dot{\Phi} - L = \frac{Q^2}{2C} + \frac{\Phi^2}{2L}. \quad (\text{D.4})$$

If the circuit is sufficiently decoupled from noisy environmental degrees of freedom, it behaves quantum mechanically and we should think of Φ and Q as operators. Since they are canonically conjugate we have $[\Phi, Q] = i\hbar$. Equation (D.4) and the commutation relation provide the complete starting point for the study of the LC oscillator in quantum mechanics.

¹Lagrange's equation of motion is $\frac{d}{dt} \left(\frac{\partial L}{\partial \dot{\Phi}} \right) - \frac{\partial L}{\partial \Phi} = 0$.

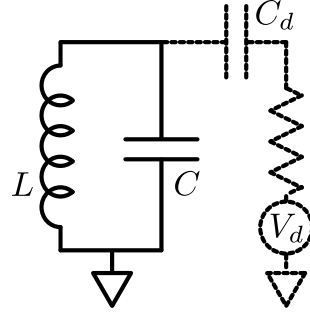


Figure D.1: A parallel LC circuit. The main circuit is shown in solid line, while the driving circuit is shown in dotted line.

D.2 Driving

Next we understand how to represent driving signals applied to the circuit. We attach a driving voltage source to our parallel LC through a capacitor C_d , as shown by the dotted elements in Fig. D.1. Before doing any formal calculation we predict should expect that this will change the effective capacitance of the LC circuit. The main capacitor C is now shunted by the series combination of the coupling capacitor C_d , and the resistance of the voltage source. Assuming the impedance of the coupling capacitor $Z_{C_d} = 1/\omega C_d$ is much larger than the voltage source resistance we can treat the driving circuit as a capacitance C_d to ground. This capacitance adds to the main circuit capacitance, leading to an effective capacitance of $C + C_d$.

Denoting the time dependent driving voltage by $V_d(t)$ and ignoring for now the resistance of the source, we work out Kirchoff's equation of motion for the driven system, resulting in

$$\frac{1}{1 + C/C_d} \dot{V}_d = \ddot{\Phi} + \frac{\omega_0^2}{1 + C_d/C} \Phi. \quad (\text{D.5})$$

This is totally sensible: the drive strength increases as C_d increases, and the resonance frequency of the LC mode has shifted due to the new capacitance. It turns out that you get this equation of motion from the following Lagrangian

$$L = \frac{1}{2} C \dot{\Phi}^2 - \frac{1}{2L} \Phi^2 + \frac{1}{2} C_d \left(\dot{\Phi} - V_d \right)^2 \quad (\text{D.6})$$

For the sake of identifying canonical coordinates consider the case $V_d = 0$. Doing this gives canonical variables

$$\Phi \quad \text{and} \quad p = \frac{\partial L}{\partial \dot{\Phi}} = (C + C_d) \dot{\Phi} \equiv Q \quad (\text{D.7})$$

just as before, except that now the capacitance associated to the momentum Q

is $C_\Sigma = C + C_d$ instead of just C . The Hamiltonian is

$$H = \frac{Q^2}{2C_\Sigma} + \frac{\Phi^2}{2L} \quad (\text{D.8})$$

Now we consider what happens when the drive turns on. The term added to the Lagrangian by the drive is

$$L_d = \frac{1}{2}C_d V_d^2 - C_d \dot{\Phi} V_d(t). \quad (\text{D.9})$$

The first term is of no consequence as it does not involve the dynamical variables. The second term couples the drive to the momentum Q . This is clear if we express the driving Lagrangian in terms of a Hamiltonian

$$H_d = C_d \dot{\Phi} V_d(t) \quad (\text{D.10})$$

$$= \frac{1}{1 + C/C_d} Q V_d(t). \quad (\text{D.11})$$

From [32] we find that we can re-express Q as

$$Q = -iQ_{\text{zpf}}(a - a^\dagger) \quad (\text{D.12})$$

with $Q_{\text{zpf}} \equiv \sqrt{\hbar/2Z_0}$ and $Z_0 \equiv \sqrt{L/C_\Sigma}$. Inserting this into the driving Hamiltonian, and taking $V_d(t) = V_0 f(t)$ gives

$$H_d = \frac{-iQ_{\text{zpf}}}{1 + C/C_d} V_0 f(t)(a - a^\dagger). \quad (\text{D.13})$$

In a two level approximation for a qubit $(a - a^\dagger) \rightarrow i\sigma_y$ and the driving Hamiltonian is

$$H_d = \frac{Q_{\text{zpf}}}{1 + C/C_d} V_0 f(t)\sigma_y \quad (\text{D.14})$$

D.2.1 Summary - Simple derivation

The energy stored in the drive capacitor is $E_d = \frac{1}{2}C_d(V_d - V_q)^2$. Keeping only the terms involving both the qubit and drive voltages yields

$$E_d = -C_d V_d V_q = -C_d V_d \frac{Q}{C} \quad (\text{D.15})$$

where Q is the qubit charge. This matches Eq. (D.11), up to the sign, in the practical limit $C \gg C_d$.

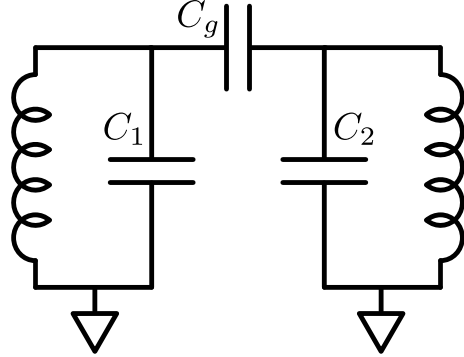


Figure D.2: Two circuits coupled through a capacitor C_g .

D.3 Coupling

D.3.1 Capacitive coupling

The circuit shown in Fig. D.2 has the following Lagrangian

$$\begin{aligned} L = & \frac{1}{2} C_1 \dot{\Phi}_1^2 + \frac{1}{2} C_2 \dot{\Phi}_2^2 \\ & + \frac{1}{2} C_g (\dot{\Phi}_1 - \dot{\Phi}_2)^2 \\ & - \frac{1}{2L_1} \Phi_1^2 - \frac{1}{2L_2} \Phi_2^2 \end{aligned} \quad (\text{D.16})$$

The kinetic term can be rewritten as

$$T = \frac{1}{2} \begin{pmatrix} \dot{\Phi}_1 & \dot{\Phi}_2 \end{pmatrix} \begin{pmatrix} C'_1 & -C_g \\ -C_g & C'_2 \end{pmatrix} \begin{pmatrix} \dot{\Phi}_1 \\ \dot{\Phi}_2 \end{pmatrix} \quad (\text{D.17})$$

where $C'_1 \equiv C_1 + C_g$ and similarly for C'_2 . The canonical momenta are

$$\begin{aligned} p_1 &= \frac{dL}{d\dot{\Phi}_1} = C'_1 \dot{\Phi}_1 - C_g \dot{\Phi}_2 \\ p_2 &= \frac{dL}{d\dot{\Phi}_2} = C'_2 \dot{\Phi}_2 - C_g \dot{\Phi}_1 \end{aligned} \quad (\text{D.18})$$

which can be written as

$$\begin{pmatrix} p_1 \\ p_2 \end{pmatrix} = \begin{pmatrix} C'_1 & -C_g \\ -C_g & C'_2 \end{pmatrix} \begin{pmatrix} \dot{\Phi}_1 \\ \dot{\Phi}_2 \end{pmatrix} \quad (\text{D.19})$$

Note the recurrence of the matrix from equation (D.17). Naming this matrix M we can write

$$T = \frac{1}{2} \begin{pmatrix} \dot{\Phi}_1 & \dot{\Phi}_2 \end{pmatrix} M \begin{pmatrix} \dot{\Phi}_1 \\ \dot{\Phi}_2 \end{pmatrix} \quad (\text{D.20})$$

$$\begin{pmatrix} \dot{\Phi}_1 \\ \dot{\Phi}_2 \end{pmatrix} = M^{-1} \begin{pmatrix} p_1 \\ p_2 \end{pmatrix} \quad (\text{D.21})$$

Substituting equation (D.21) into (D.20) and using the facts that matrix transposition commutes with matrix inversion and that M is symmetric we get

$$T = \frac{1}{2} \begin{pmatrix} p_1 & p_2 \end{pmatrix} M^{-1} \begin{pmatrix} p_1 \\ p_2 \end{pmatrix} \quad (\text{D.22})$$

The inverse of the 2x2 matrix M is

$$\begin{aligned} M^{-1} &= \frac{1}{C_1 C_2 + C_g(C_1 + C_2)} \begin{pmatrix} C'_2 & C_g \\ C_g & C'_1 \end{pmatrix} \\ &\equiv \begin{pmatrix} 1/C''_1 & 1/C''_g \\ 1/C''_g & 1/C''_2 \end{pmatrix} \end{aligned} \quad (\text{D.23})$$

Finally the kinetic term of the Langrangian is

$$T = \frac{p_1^2}{2C''_1} + \frac{p_2^2}{2C''_2} + \frac{p_1 p_2}{C''_g} \quad (\text{D.24})$$

Let us now understand the quantities C''_1 and C''_2 in a simple way. The capacitance to ground from the signal node of circuit 1 is

$$\begin{aligned} C_{1,\text{total}} &= C_1 \parallel (C_g \text{ in series with } C_2) \\ &= C_1 + \frac{C_g C_2}{C_g + C_2} \\ &= \frac{C_1 C_2 + C_g(C_1 + C_2)}{C_g + C_2} \end{aligned}$$

which is exactly equal to our expression for C''_1 . Therefore we've found that **the effective capacitance associated with the the canonical charge is just the capacitance to ground of the conjugate flux's signal node.**

The quantities p_1 and p_2 have dimensions of charge so we will rename them \tilde{Q}_1 and \tilde{Q}_2 . The tildes remind us that they are not the usual single qubit charges.

The coupling term in the Hamiltonian, eq. (D.24), is

$$H_g = \frac{\tilde{Q}_1 \tilde{Q}_2}{C''_g}. \quad (\text{D.25})$$

We would like to re-express it in terms of Pauli operators. If we use the (very good) approximation that the normal modes are harmonic we can rewrite the charge operators as

$$\tilde{Q} = -iQ_{\text{zpf}}(a - a^\dagger). \quad (\text{D.26})$$

The parameter Q_{zpf} is the rms zero point fluctuations in charge and is given by [32]

$$Q_{\text{zpf}} = \sqrt{\frac{\hbar}{2Z}} = \sqrt{\frac{\hbar\omega C}{2}} \quad (\text{D.27})$$

Substitution of this expression for the \tilde{Q} coordinates turns the coupling Hamiltonian into

$$\begin{aligned} H_g &= \frac{Q_{1,\text{zpf}}Q_{2,\text{zpf}}}{C_g''}(-i)(a_1 - a_1^\dagger)(-i)(a_2 - a_2^\dagger) \\ &= \frac{\hbar}{2}\sqrt{\omega_1\omega_2}C_1''C_2''\frac{C_g}{C_1C_2 + C_g(C_1 + C_2)}(\sigma_y \otimes \sigma_y) \\ &= \frac{1}{2}\frac{C_g}{\sqrt{C_1'C_2'}}\hbar\sqrt{\omega_1\omega_2}(\sigma_y \otimes \sigma_y) \end{aligned}$$

We combine the prefactors into a parameter g and write the Hamiltonian written as

$$H_g = g(\sigma_y \otimes \sigma_y) \quad (\text{D.28})$$

where g , called the “coupling strength”, is defined as

$$g \equiv \frac{1}{2}\frac{C_g}{\sqrt{C_1'C_2'}}\hbar\sqrt{\omega_1\omega_2}. \quad (\text{D.29})$$

D.3.2 Summary - Simple derivation

The energy in the coupling capacitor is $E_g = \frac{1}{2}C_g(V_1 - V_2)^2$. Keeping only the term which couples the qubits, we find

$$E_g = -C_gV_1V_2 = -C_g\frac{Q_1}{C_1}\frac{Q_2}{C_2}. \quad (\text{D.30})$$

This matches Eq. (D.25), up to the sign, in the practical limit $C_1, C_2 \gg C_g$.

D.4 Rotating Frame

The driving and coupling Hamiltonians we have written down were expressed in the lab frame. When doing experiments and calculations it is much easier to reason in a frame that rotates at a frequency near or equal to the resonance frequency of the device. In this section we show how to re-express the driving and coupling Hamiltonians in a rotating frame.

The single qubit Hamiltonian is

$$H_q/\hbar = -\frac{\omega_q}{2}\sigma_z \quad (\text{D.31})$$

where $\omega_q = \omega_0 + \delta\omega$. Think of ω_0 as an idle point frequency and $\delta\omega$ as a dynamic detuning. The Schrodinger picture time evolution operator is $T = \exp[-iH/\hbar]$.

In order to remove the idle point precession of the qubit state, we take as the rotation operator

$$R = T^\dagger = \exp \left[-i \frac{\omega_0}{2} t \sigma_z \right], \quad (\text{D.32})$$

e.g. we rotate the frame by the idle frequency of the qubit. We compute the remaining effective Hamiltonian H' according to [31]

$$H'/\hbar = i \dot{R} R^\dagger + R \frac{H_q}{\hbar} R \quad (\text{D.33})$$

$$= i \left(-i \frac{\omega_0}{2} \right) \sigma_z R R^\dagger + R \frac{H_q}{\hbar} R^\dagger \quad (\text{D.34})$$

$$= -\frac{\delta\omega}{2} \sigma_z. \quad (\text{D.35})$$

This is precisely the Hamiltonian of a qubit with frequency $\delta\omega$. In other words, if we go into a frame rotating at the idle frequency of the qubit, what remains is just the qubit precession at the detuning frequency. In particular if the frame rotates at the same frequency as the qubit the Hamiltonian becomes zero.

D.4.1 Operators

Since we are going to want to work in a frame in which the qubit intrinsic Hamiltonian is zero it will be useful to find the form of various operators in that frame. We list here the transformation of the Pauli operators under the rotating frame given by $R = \exp \left[-i \frac{1}{2} \omega_r t \sigma_z \right]$ [31]

$$\begin{aligned} R\sigma_x R^\dagger &= \cos(\omega_r t) \sigma_x + \sin(\omega_r t) \sigma_y \\ R\sigma_y R^\dagger &= \cos(\omega_r t) \sigma_y - \sin(\omega_r t) \sigma_x \\ R\sigma_z R^\dagger &= \sigma_z \\ R\sigma_+ R^\dagger &= e^{i\omega_r t} \sigma_+ \\ R\sigma_- R^\dagger &= e^{-i\omega_r t} \sigma_- \end{aligned}$$

D.4.2 Driving

We now consider the driving Hamiltonian in the rotating frame. From Eq. (D.14) we have the driving Hamiltonian in the lab frame

$$H_d = h_d f(t) \sigma_y \quad (\text{D.36})$$

where $h_d \equiv Q_{\text{zpf}} V_0 / (1 + C/C_d)$. We use the rotation operator

$$R = \exp \left[-i \frac{\omega_r}{2} t \sigma_z \right]. \quad (\text{D.37})$$

The transformed driving Hamiltonian is

$$\begin{aligned} R H_d R^\dagger / h_d &= e^{-i \frac{\omega_r}{2} t \sigma_z} f(t) \sigma_y e^{i \frac{\omega_r}{2} t \sigma_z} \\ &= f(t) [\cos(\omega_r t) \sigma_y - \sin(\omega_r t) \sigma_x]. \end{aligned} \quad (\text{D.38})$$

Now suppose $f(t)$ is a sinusoid with an envelope $e(t)$,

$$f(t) = e(t) \sin(\omega_d t + \phi_d) \quad (\text{D.39})$$

$$= e(t) [\cos(\phi_d) \sin(\omega_d t) + \sin(\phi_d) \cos(\omega_d t)] \quad (\text{D.40})$$

$$= e(t) [I \sin(\omega_d t) - Q \cos(\omega_d t)]. \quad (\text{D.41})$$

Multiplying everything in eq (D.38) together and throwing out the high frequency terms we get

$$\begin{aligned} RH_d R^\dagger / h_d &= \frac{e(t)}{2} [\sin(\delta\omega t + \phi_d) \sigma_y \\ &\quad - \cos(\delta\omega t + \phi_d) \sigma_x] \end{aligned} \quad (\text{D.42})$$

$$\begin{aligned} &= -\frac{e(t)}{2} \left[e^{-i(\delta\omega t + \phi_d)} \sigma_+ \right. \\ &\quad \left. + e^{i(\delta\omega t + \phi_d)} \sigma_- \right] \end{aligned} \quad (\text{D.43})$$

where $\delta\omega \equiv \omega_d - \omega_r$. In matrix form this reads

$$RH_d H^\dagger / h_d = -\frac{e(t)}{2} \begin{pmatrix} 0 & e^{i(\delta\omega t + \phi_d)} \\ e^{-i(\delta\omega t + \phi_d)} & 0 \end{pmatrix}. \quad (\text{D.44})$$

If the drive is on resonance with the frame then we are left with

$$RH_d R^\dagger / h_d = -\frac{e(t)}{2} \begin{pmatrix} 0 & e^{i\phi_d} \\ e^{-i\phi_d} & 0 \end{pmatrix} \quad (\text{D.45})$$

$$= -\frac{e(t)}{2} [I \sigma_x + Q \sigma_y]. \quad (\text{D.46})$$

This is a rotation about a time independent axis in the xy plane of the Bloch sphere. If the rotating frame frequency is the same as the qubit frequency, then the qubit Hamiltonian is zero and our on-resonance drive leads to a purely latitudinal rotation on the Bloch sphere with the angle of the rotation axis in the xy plane given by ϕ . If the qubit frequency does not match the rotating frame then the qubit Hamiltonian has a residual σ_z component and the rotation axis will be out of the xy plane.

pi pulse

For a resonant drive with $\phi_d = 0$ we have

$$RH_d R^\dagger = -\frac{e(t)}{2} \frac{V_0 Q_{\text{zpf}}}{1 + C_d/C} \sigma_x. \quad (\text{D.47})$$

The evolution of the qubit under this drive is given by the unitary operator

$$U(t) = \exp \left[i \left(\frac{1}{\hbar} \frac{1}{2} \frac{V_0 Q_{\text{zpf}}}{1 + C_d/C} \int dt e(t) \right) \sigma_x \right]. \quad (\text{D.48})$$

This results in a pi pulse when $U(t) = \sigma_x$. Since

$$\exp[i\alpha\sigma_x] = \cos(\alpha)\mathbf{I} + i\sin(\alpha)\sigma_x \quad (\text{D.49})$$

we see that the pi pulse occurs when

$$\frac{1}{2\hbar} \frac{V_0 Q_{\text{zpf}}}{1 + C_d/C} \int e(t) dt = \frac{\pi}{2} \quad (\text{D.50})$$

This relation is used to determine the appropriate drive capacitance C_d when designing a device. The accessible values of V_0 are determined by the dynamic range of available pulse generators, the level of attenuation needed to remove noise from the drive lines, and the value of C_d , which must be small enough to prevent the resistance of the drive lines from significantly damping the qubit. The value of Q_{zpf} is also important and is determined by the type of qubit.

Programming for experiment

Now that we know what the driving Hamiltonian looks like in the rotating frame we can investigate how to program our IF inputs to the IQ mixer to achieve a rotation on the Bloch sphere. From [29] we know that an input IQ signal $e(t) \exp[i\omega t + \phi]$ produces an RF signal $e(t) \cos[(\omega_c + \omega)t + \phi]$, where ω_c is the carrier frequency. Using trig identities we can rewrite this RF signal as

$$e(t) [I \cos([\omega_c + \omega]t) + Q \sin([\omega_c + \omega]t)]$$

where $I = \cos(\phi)$ and $Q = -\sin(\phi)$. If we add a phase $\pi/2$ this becomes

$$e(t) [I \sin([\omega_c + \omega]t) - Q \cos([\omega_c + \omega]t)] \quad (\text{D.51})$$

which exactly matches the form we assumed for $f(t)$ in eq. (D.41) if we take $\omega_c + \omega = \omega_d$. Therefore if we choose ω such that $\omega + \omega_c = \omega_q$ and work in the rotating frame of the qubit, the driving Hamiltonian is

$$H_d/h_d = -\frac{e(t)}{2} [I\sigma_x + Q\sigma_y]. \quad (\text{D.52})$$

In practice we don't want to have to remember to account for the carrier frequency when programming a pulse so we define a mix function which multiplies our complex signal by $\exp[i(\omega_q - \omega_c)]$. That way if we program a signal $\exp[i\phi]$ the driving Hamiltonian in the frame of the qubit is produced in the following steps

$$\begin{array}{ll} \text{program} & e(t)e^{i\phi} \\ \xrightarrow{\text{mix function}} & e(t)e^{i([\omega_q - \omega_c]t + \phi)} \\ \xrightarrow{\text{physical mixer}} & \text{Re} \left[e(t)e^{i(\omega_q t + \phi)} \right] = e(t) \cos(\omega_q t + \phi) \\ \xrightarrow{\pi/2 \text{ phase shift}} & e(t) \sin(\omega_q t + \phi) \\ \xrightarrow{\text{Hamiltonian}} & -\frac{e(t)}{2} [I\sigma_x + Q\sigma_y]. \end{array}$$

Thus our choice of angle ϕ directly maps to the angle of the rotation on the Bloch Sphere.

D.4.3 coupling

We found that the coupling Hamiltonian in the Schrodinger picture is

$$H_g = g(\sigma_y \otimes \sigma_y) \quad (\text{D.53})$$

which can be expanded as

$$\begin{aligned} H_g &= -g(\sigma^+ - \sigma^-) \otimes (\sigma^+ - \sigma^-) \\ &= g(-\sigma^+\sigma^+ - \sigma^-\sigma^- + \sigma^+\sigma^- + \sigma^-\sigma^+). \end{aligned} \quad (\text{D.54})$$

Rotating the qubits' frames at ω_{r1} and ω_{r2} respectively and throwing away high frequency terms we get

$$H_g = g(e^{i\delta\omega_{r12}t}\sigma^+\sigma^- + e^{-i\delta\omega_{r12}t}\sigma^-\sigma^+) \quad (\text{D.55})$$

where $\delta\omega_{r12} \equiv \omega_{r1} - \omega_{r2}$. If both frames rotate at the same frequency the interaction simplifies to

$$H_g = g(\sigma^+\sigma^- + \sigma^-\sigma^+). \quad (\text{D.56})$$

The matrix form, with basis states

$$[|00\rangle, |01\rangle, |10\rangle, |11\rangle]$$

(ie the states defined by Kronecker product) is

$$H_g = g \begin{bmatrix} 0 & 0 & 0 & 0 \\ 0 & 0 & 1 & 0 \\ 0 & 1 & 0 & 0 \\ 0 & 0 & 0 & 0 \end{bmatrix}. \quad (\text{D.57})$$

Appendix E

Discrete Fourier transform of White Noise

In this note we show how to compute the probability distribution of the discrete Fourier transform (DFT) of a white noise signal. For an N point sequence of white noise with Gaussian distribution of width σ , the real and imaginary parts of the discrete Fourier transform are both Gaussian distributed random variables with widths $\sigma\sqrt{N}/2$. If the DFT is normalized by the number of points N , the width becomes $\sigma/\sqrt{2N}$.

When demodulating a signal with a discrete Fourier transform (DFT) one must carefully analyze the effect of noise. The incoming signal will in general be given by

$$V_n = s_n + \xi_n \quad (\text{E.1})$$

where s_n is the desired signal and ξ_n is the noise.

E.1 White noise

We consider first the case of white noise. A true white noise process has the unique property that the correlation between noise values at two different points in time is identically zero. This property is crucial to the calculation, as will be seen below. However, in most signal processing applications, such a process does not truly exist. A noise source with constant spectral density at all frequencies would emit an infinite power, which is not physically possible. Johnson-Nyquist noise, which is typically considered to be white, rolls off above a certain cutoff frequency [24]. Even the “quantum noise” attributed to quantum measurement statistics is usually not white in practice because the transfer functions of detection hardware shape the noise spectral density. This is particularly true in the context of digital acquisition hardware where anti-aliasing filters restrict the noise spectral density to frequencies below one half the sampling rate. In those systems, the assumption that the noise samples are uncorrelated is clearly

incorrect. Nevertheless, we consider white noise here for several reasons. First, the calculation of the statistics of the DFT of true white noise can be done analytically. This will provide formulae against which we compare numerical results obtained for the realistic case of correlated noise. Second, applications with true white noise do exist. For example, repeated measurements of a quantum 2 level system will involve white noise from the randomness of the quantum measurement. On each repetition of the experiment, a given superposition state $\alpha|0\rangle + \beta|1\rangle$ yields a random result 0 or 1. The values measured on subsequent experiments are uncorrelated in principle, with correlations arising only through correlated errors in state preparation and measurement.

Assuming that the noise is Gaussian distributed with a white power spectrum, the random variables ξ_n are distributed according to a Gaussian curve and each value of ξ_n is independent of all the others. When we say that ξ_n is Gaussian distributed what we mean is that if you pick a value of n the value of ξ_n is random, but is distributed as

$$p_{\xi_n}(\xi) = \frac{1}{\sqrt{2\pi\sigma^2}} \exp\left[-\frac{\xi^2}{2\sigma^2}\right] \equiv G_\sigma(\xi).$$

The DFT of this signal is

$$V_k = \sum_{n=1}^N (s_n + \xi_n) e^{-i2\pi kn/N}. \quad (\text{E.2})$$

The DFT is linear, so we may compute each term separately. The noise part is

$$\xi_k = \sum_{n=1}^N \xi_n e^{-i2\pi kn/N}. \quad (\text{E.3})$$

Because each DFT coefficient ξ_k is given as a sum, its distribution is given as the convolution of the terms in the sum. This gives us a clear path to work the calculation: write down the distributions of the terms in the sum, then convert to the Fourier domain and compute the convolution, and finally Fourier transform back to the time domain.

Consider first only the distribution of the real part,

$$\begin{aligned} \text{Re}\xi_k &= \sum_{n=1}^N \xi_n \cos[2\pi nk/N] \\ \text{Re}\xi_k &= \sum_{n=1}^N x_n \end{aligned} \quad (\text{E.4})$$

where we've defined $x_n \equiv \xi_n \cos[2\pi nk/N]$. Note that the summands x_n are random variables. What is the distribution of x_n ? For any random variable x with distribution $p_x(x)$ the distribution of the scaled variable Ax is simply $p_{Ax}(y) = \frac{1}{A}p_x(y/A)$. Therefore the distribution of the summand x_n is

$$p_{x_n}(x) = \frac{1}{c_{n,k}} p_{\xi_n}(x/c_{n,k}) = \frac{1}{c_{n,k}} G_\sigma(x/c_{n,k}) \quad (\text{E.5})$$

where we've abbreviated $c_{n,k} \equiv \cos[2\pi nk/N]$. Because of the form of the Gauss function this simplifies to

$$p_{x_n}(x) = G_{\sigma c_{n,k}}(x). \quad (\text{E.6})$$

We want to compute the distribution of the summed quantity in (E.4). To do this we use the fact that the probability distribution of a quantity that is a sum of random variables is the convolution of the distributions of the summands. Using this fact on (E.4) gives

$$p_{\text{Re}\xi_k} = p_{x_1} \otimes p_{x_2} \otimes \cdots \otimes p_{x_N} \quad (\text{E.7})$$

where \otimes denotes convolution. This multiple convolution is made easy by going to the Fourier transform, because the Fourier transform of a convolution is the product of the Fourier transforms of the things being convolved. In other words,

$$\mathcal{F}[p_{\text{Re}\xi_k}] = \prod_{n=1}^N \mathcal{F}[p_{x_n}]. \quad (\text{E.8})$$

Inserting the form of p_{x_n} from (E.6) gives

$$\mathcal{F}[p_{\text{Re}\xi_k}] = \prod_{n=1}^N \mathcal{F}[G_{\sigma c_{n,k}}]. \quad (\text{E.9})$$

This is particularly convenient because the Fourier transform of a Gaussian function is just another Gaussian with the reciprocal width,

$$\mathcal{F}[G_\sigma(x)] = G_{1/\sigma}.$$

Therefore (E.9) becomes

$$\mathcal{F}[p_{\text{Re}\xi_k}] = \prod_{n=1}^N G_{1/(\sigma c_{n,k})}. \quad (\text{E.10})$$

Writing this out explicitly we get

$$\begin{aligned} \mathcal{F}[p_{\text{Re}\xi_k}](q) &= \prod_{n=1}^N \sqrt{\frac{\sigma^2 c_{n,k}^2}{2\pi}} \exp\left[-\frac{q^2}{2}\sigma^2 c_{n,k}^2\right] \\ &= \left(\frac{\sigma^2}{2\pi}\right)^{N/2} \left(\prod_{n=1}^N c_{n,k}\right) \cdots \\ &\quad \cdots \exp\left[-\frac{q^2}{2}\sigma^2 \sum_{n=1}^N \cos[2\pi nk/N]^2\right]. \end{aligned}$$

The factors preceding the exponential are independent of q and are therefore just a normalization constant. The exponential part is just a gaussian in q with

width $\left(\sigma^2 \sum_{n=1}^N \cos [2\pi nk/N]^2\right)^{-1/2}$. The sum can be done explicitly and is equal to $N/2$. Therefore

$$\mathcal{F}[p_{\text{Re}\xi_k}] \propto G_{(\sigma^2 N/2)^{-1/2}} \quad (\text{E.11})$$

and performing the inverse Fourier transform gives us

$$p_{\text{Re}\xi_k} = G_{\sigma/\sqrt{N/2}}. \quad (\text{E.12})$$

We have therefore computed the probability distribution of the real part of the Fourier transform of a white noise signal. The imaginary part has exactly the same distribution. Note that the result is independent of the demodulation frequency k which is a reflection of the fact that we're considering uncorrelated white noise.

Intuition (and experience) says that more data gives better signal to noise ratio, but we found that the distribution of the noise Fourier transform becomes *wider* as more data points are collected. The reason for this discrepancy is that we didn't normalize the Fourier transform. When measuring a single tone signal s_n , we have to normalize the DFT in order to get a measured Fourier amplitude that is independent of the number of measured points,

$$s_k = \frac{1}{N} \sum_{n=1}^N s_n e^{-i2\pi nk/N}. \quad (\text{E.13})$$

If we use this normalized quantity in the calculation of the noise Fourier amplitude,

$$\xi_k = \frac{1}{N} \sum_{n=1}^N \xi_n e^{-i2\pi kn/N} \quad (\text{E.14})$$

then the distribution of the real part winds up being

$$p_{\text{Re}\xi_k} = G_{\sigma/\sqrt{2N}} \quad (\text{E.15})$$

which becomes sharper as N increases, in agreement with the idea that the noise should go down as more data is collected.

There is a simple way to remember these results. The incoming noise signal had a squared width given by σ^2 . This is proportional to the power per bandwidth of the incoming signal. If we measure N points of this noise signal the total power should scale with N . Then, if we only look at one of the two resulting components, ie. the real part, we should find half the power. Therefore, the squared width of the distribution of the real part should be $\sigma^2 N/2$ which agrees with (E.12).

E.1.1 Distribution of r^2

We have shown that the real and imaginary parts of the Fourier transform are Gaussian distributed random variables with width $\sigma/\sqrt{2N}$. We now calculate

the distribution of the mod square of the Fourier transform. Define the mod square as

$$r^2 = \text{Re}\xi_k^2 + \text{Im}\xi_k^2. \quad (\text{E.16})$$

To compute the distribution of the mod square we first compute the distributions of the squares of the real and imaginary parts. We will then use the convolution rule to find the distribution of their sum. For the sake of compact notation let $x \equiv \text{Re}\xi_k$.

To compute the distribution of the square of a random variable we use the general formula for computing the distribution of a variable defined as an arbitrary function of another random variable. For a variable Y defined by $y = g(x)$ we have

$$p_Y(y) = p_X(g^{-1}(y)) |Dg^{-1}(y)| \quad (\text{E.17})$$

In our case where $g(x) = x^2$, we find $Dg^{-1}(x)/dx \propto 1/\sqrt{x}$. This leads to

$$p_{X^2}(\alpha) \propto G_{\sigma/\sqrt{2N}}(g^{-1}(\alpha)) \frac{1}{\sqrt{\alpha}} \quad (\text{E.18})$$

$$\propto \exp\left[-\frac{\alpha}{\sigma^2/N}\right] \frac{1}{\sqrt{\alpha}} \quad (\text{E.19})$$

for positive α and zero otherwise. From symmetry considerations it's clear that the square of the imaginary part has the same distribution. The distribution of the mod square is therefore given by the convolution of the function found in Eq. (E.19) with itself; the result is

$$p_{r^2}(\alpha) = \frac{1}{\sigma^2/N} \exp\left[-\frac{\alpha}{\sigma^2/N}\right]. \quad (\text{E.20})$$

Therefore the distribution of the squared modulus of the Fourier component is exponentially distributed.

From this last result we can compute the mean of the square of the Fourier coefficient,

$$\langle |\xi_k|^2 \rangle = \frac{\sigma^2}{N}. \quad (\text{E.21})$$

E.2 Correlated noise

We now turn to the case of correlated noise. Because the noise is correlated, the values ξ_n are no longer statistically independent. This means that we cannot use the multiple convolutions trick we used in the white noise case.

We begin by stepping back to the definition of the DFT. The real part of the DFT of the noise is

$$\text{Re}\xi_k = \sum_{n=1}^N \xi_n \cos[2\pi nk/N]. \quad (\text{E.22})$$

The Fourier coefficients $\text{Re}\xi_k$ are expressed as a sum of random variables. Therefore, the central limit theorem guarantees that the distribution of $\text{Re}\xi_k$ can be approximated by a Gaussian distribution as long as N is sufficiently large. In particular, N must be large enough that the correlations time of ξ_n is small compared to N . Working under the assumption that we are in this limit, $\text{Re}\xi_k$ are Gaussian distributed and we need only compute the variance. Note, however, that even if this assumption is not completely valid, a Gaussian distribution with the calculated variance should at least approximate the true distribution.

The variance of $\text{Re}\xi_k$ is

$$\langle \text{Re}\xi_k \text{Re}\xi_l \rangle = \frac{1}{N^2} \sum_{n,m=0}^{N-1} \langle \xi_n \xi_m \rangle \cos(2\pi nk/N) \cos(2\pi ml/N), \quad (\text{E.23})$$

where $\langle \cdot \rangle$ indicates an ensemble average. Our crucial observation is that $\langle \xi_n \xi_m \rangle$ is, by definition, the auto-correlation function of the noise. The Wiener-Khinchin theorem relates the auto-correlation function of a process x to its spectral density

$$\rho_x(\tau) \equiv \langle x(0)x(\tau) \rangle \quad (\text{E.24})$$

$$= \int_0^\infty S_x^e(\omega) \cos(\omega\tau) \frac{d\omega}{2\pi}. \quad (\text{E.25})$$

The superscript e on S_x^e is a reminder that this is an “engineer’s” spectral density, defined for only positive frequency. In other words, the total power P in the process is

$$P = \int_0^\infty S_x^e(\omega) \frac{d\omega}{2\pi}. \quad (\text{E.26})$$

Note that $\rho(\tau) = \rho(-\tau)$. Denoting the digital sampling time interval by δt and assuming that the autocorrelation is invariant under time shift of both measurements, we can rewrite the correlation as

$$\langle \xi_n \xi_m \rangle = \langle \xi(n\delta t) \xi(m\delta t) \rangle = \rho_\xi(\delta t |n - m|). \quad (\text{E.27})$$

Using this expression we can finally write the variance of $\text{Re}\xi_k$ as

$$\begin{aligned} \langle \text{Re}\xi_k \text{Re}\xi_l \rangle &= \\ \frac{1}{N^2} \sum_{n,m=0}^{N-1} \rho_\xi(\delta t |n - m|) \cos(2\pi nk/N) \cos(2\pi ml/N). \end{aligned} \quad (\text{E.28})$$

In practice, ρ_ξ is calculated via Eq. (E.25), with S^e determined by the transfer function of analog filters placed before the digitizer inputs. Once ρ_ξ is known, the double sum in Eq. (E.28) can be done numerically (although see Ref. [35] for examples where the sum can be done analytically).

Appendix F

External Loading of a Resonant Mode

In this appendix we derive a simple formula for the loaded quality factor of a parallel resonance circuit connected to an external lossy element.

F.1 Parallel-Series Equivalence

We consider two networks: a series resistance R_S and reactance X_S , and a parallel resistance R_P and reactance X_P . The circuits are shown in Fig. F.1. The impedance of the series network is

$$Z_S = R_S + iX_S, \quad (\text{F.1})$$

and the impedance of the parallel network is

$$Z_P = R_P \frac{1}{1 + Q_P^2} + iX_P \frac{Q_P^2}{1 + Q_P^2}. \quad (\text{F.2})$$

The series circuit has quality factor $Q_S \equiv X_S/R_S$, and the parallel circuit has quality factor $Q_P \equiv R_P/X_P$. Setting the two impedances equal yields

$$R_S = R_P \frac{1}{1 + Q_P^2} \quad X_S = X_P \frac{Q_P^2}{1 + Q_P^2}. \quad (\text{F.3})$$

Dividing these equations gives

$$Q_S = \frac{X_S}{R_S} = \frac{X_P}{R_P} Q_P^2 = Q_P. \quad (\text{F.4})$$

This is the main result of this section: the Q of equivalent parallel and series circuits are equal.

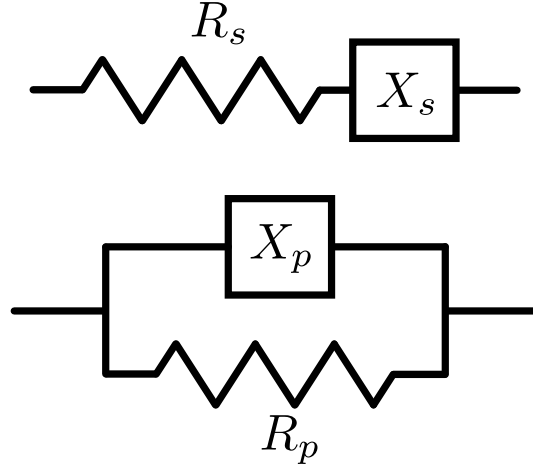


Figure F.1: Series and parallel circuits. The reactances X_S and X_P can be capacitive or inductive.

Since both quality factors are equal we can drop the subscript. We then rewrite the relations between the series and parallel components as

$$R_S = R_P \frac{1}{1+Q^2} \quad X_S = X_P \frac{Q^2}{1+Q^2}. \quad (\text{F.5})$$

These equations provide a simple way to convert a series circuit to an equivalent parallel one, and vice versa. For a given series circuit, one computes Q and then uses Eq. (F.5) to compute X_P and R_P . Note that, because the reactances X_S and X_P generally depend on frequency, Q and therefore the equivalence transformation also depend on frequency.

F.1.1 Large Q limit

In many cases, we have series or parallel circuit fragments for which $Q \gg 1$. In these cases the transformation equations simplify to

$$R_S = R_P/Q^2 \quad X_S = X_P. \quad (\text{F.6})$$

We explain this intuitively: if the series resistance is low enough that the Q is high, the parallel resistance must be large to ensure it doesn't absorb much energy. In this case the reactance dominates and is therefore unchanged in the transformation.

F.2 Loaded resonant mode

Using the series/parallel equivalence we can easily understand the effect of coupling a resonant mode to an external resistance through a coupling capacitor or

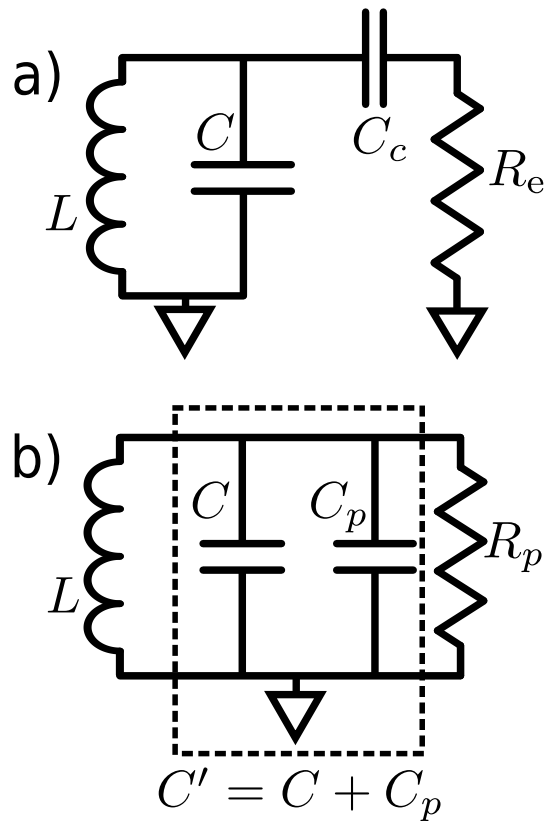


Figure F.2: Loaded resonant mode. a) The parallel oscillator is connected to an external resistor R_e through a coupling capacitor C_c . b) Using the series/parallel transformation we can think of the series damping circuit as a parallel circuit. In this case the capacitance C_c adds with the internal capacitance of the mode and the resistor is transformed up to a higher resistance.

inductor. We work specifically in the $Q \gg 1$ limit. For illustration we calculate case of capacitive coupling, and then state the result for inductive coupling. Consider the circuit shown in Figure F.2 in which a resonator coupled to a resistor R_e through a coupling capacitor C_c . To understand the effect of the shunt circuit on the resonator, we convert the shunt to an equivalent parallel resistance and capacitance. The Q of attached damping circuit is

$$Q_e = \frac{1}{\omega C_c R_e}. \quad (\text{F.7})$$

The equivalent parallel reactance is

$$X_P = -1/\omega C_c, \quad (\text{F.8})$$

and the equivalent parallel resistance is

$$R_P = R_e Q_e^2. \quad (\text{F.9})$$

The series damping circuit is thus transformed to a parallel capacitor and resistor. Note that the new parallel resistor adds in parallel with any pre-existing resistor in the oscillator. This is why Q values usually add in parallel.

The quality factor of the resonant mode near resonance is

$$Q = \omega_0 R_P C' \quad (\text{F.10})$$

where $C' = C + C_c \approx C$, as illustrated in Fig. F.2. Substituting in for R_P we get

$$Q = \omega_0 R_e Q_e^2 C \quad (\text{F.11})$$

$$= \frac{\omega_0 R_e C}{\omega^2 R_e^2 C_c^2} \quad (\text{F.12})$$

$$= \frac{C}{C_c} Q_e, \quad (\text{F.13})$$

where in the last step we've restricted to the case $\omega/\omega_0 \approx 1$. This is the second main result: the total quality factor is the Q_e of the external circuit scaled by the ratio of the coupling capacitance to the mode's internal capacitance.

If the coupling capacitor were replaced with a coupling inductor L_c we would get

$$Q = \frac{L_c}{L} Q_e. \quad (\text{F.14})$$

The Q which arises from the coupling of the resonator to an external load is called the “coupling Q ”. The coupling Q adds in parallel with the internal quality factor Q_i of the resonator for the reason mentioned above, to produce the full “loaded quality factor” Q_l of the resonator:

$$Q_l^{-1} = Q_i^{-1} + Q_c^{-1}. \quad (\text{F.15})$$

In summary, when a resonant mode is connected to an external resistor R_e through a coupling capacitor C_c or inductor L_c , the coupling quality factor for the mode is given by

$$Q_c = \frac{C}{C_c} Q_e \quad \text{or} \quad Q_c = \frac{L_c}{L} Q_e \quad (\text{F.16})$$

where $Q_e = X/R_e$ and X is the reactance of either L_c or C_c near the mode's resonance frequency.

Bibliography

- [1] O Astafiev, Yu A Pashkin, T Yamamoto, Y Nakamura, and JS Tsai. Single-shot measurement of the josephson charge qubit. *Physical Review B*, 69(18):180507, 2004.
- [2] R. Barends, J. Kelly, A. Megrant, D. Sank, E. Jeffrey, Y. Chen, Y. Yin, B. Chiaro, J. Mutus, C. Neill, P. O'Malley, P. Roushan, J. Wenner, T. C. White, A. N. Cleland, and John M. Martinis. Coherent josephson qubit suitable for scalable quantum integrated circuits. *Phys. Rev. Lett.*, 111:080502, Aug 2013.
- [3] R Barends, J Kelly, A Megrant, A Veitia, D Sank, E Jeffrey, TC White, J Mutus, AG Fowler, B Campbell, et al. Superconducting quantum circuits at the surface code threshold for fault tolerance. *Nature*, 508(7497):500–503, 2014.
- [4] R Barends, J Wenner, M Lenander, Y Chen, RC Bialczak, J Kelly, E Lucero, P OMalley, M Mariantoni, D Sank, et al. Minimizing quasi-particle generation from stray infrared light in superconducting quantum circuits. *Applied Physics Letters*, 99(11):113507, 2011.
- [5] Jan Benhelm, Gerhard Kirchmair, Christian F Roos, and Rainer Blatt. Towards fault-tolerant quantum computing with trapped ions. *Nature Physics*, 4(6):463–466, 2008.
- [6] Alexandre Blais, Ren-Shou Huang, Andreas Wallraff, SM Girvin, and R Jun Schoelkopf. Cavity quantum electrodynamics for superconducting electrical circuits: An architecture for quantum computation. *Physical Review A*, 69(6):062320, 2004.
- [7] Rainer Blatt and David Wineland. Entangled states of trapped atomic ions. *Nature*, 453(7198):1008–1015, 2008.
- [8] Sergio Boixo, Troels F Rønnow, Sergei V Isakov, Zhihui Wang, David Wecker, Daniel A Lidar, John M Martinis, and Matthias Troyer. Quantum annealing with more than one hundred qubits. *arXiv preprint arXiv:1304.4595*, 2013.

- [9] Carlton M Caves. Quantum limits on noise in linear amplifiers. *Physical Review D*, 26(8):1817, 1982.
- [10] Intel Corporation. Intel earnings release, 2014.
- [11] Daniel Esteve, Michel H. Devoret, and John M. Martinis. Effect of an arbitrary dissipative circuit on the quantum energy levels and tunneling of a josephson junction. *Phys. Rev. B*, 34:158–163, Jul 1986.
- [12] Austin G. Fowler, Matteo Mariantoni, John M. Martinis, and Andrew N. Cleland. Surface codes: Towards practical large-scale quantum computation. *Phys. Rev. A*, 86:032324, Sep 2012.
- [13] J. E. Johnson, C. Macklin, D. H. Slichter, R. Vijay, E. B. Weingarten, John Clarke, and I. Siddiqi. Heralded state preparation in a superconducting qubit. *Phys. Rev. Lett.*, 109:050506, Aug 2012.
- [14] B. D. Josephson. Possible new effects in superconductive tunnelling. *Physics Letters*, 1:251–253, Jul 1962.
- [15] Jens Koch, Terri M. Yu, Jay Gambetta, A. A. Houck, D. I. Schuster, J. Majer, Alexandre Blais, M. H. Devoret, S. M. Girvin, and R. J. Schoelkopf. Charge-insensitive qubit design derived from the cooper pair box. *Phys. Rev. A*, 76:042319, Oct 2007.
- [16] Arjen K. Lenstra and Hendrik W. Lenstra Jr., editors. *The development of the number field sieve*. Springer Berlin, Heidelberg, 1993.
- [17] François Mallet, Florian R Ong, Agustin Palacios-Laloy, Francois Nguyen, Patrice Bertet, Denis Vion, and Daniel Esteve. Single-shot qubit readout in circuit quantum electrodynamics. *Nature Physics*, 5(11):791–795, 2009.
- [18] John M Martinis, S Nam, J Aumentado, and C Urbina. Rabi oscillations in a large josephson-junction qubit. *Physical Review Letters*, 89(11):117901, 2002.
- [19] A Megrant, C Neill, R Barends, B Chiaro, Yu Chen, L Feigl, J Kelly, Erik Lucero, Matteo Mariantoni, PJJ OMalley, et al. Planar superconducting resonators with internal quality factors above one million. *Applied Physics Letters*, 100(11):113510–113510, 2012.
- [20] JE Mooij, TP Orlando, L Levitov, Lin Tian, Caspar H Van der Wal, and Seth Lloyd. Josephson persistent-current qubit. *Science*, 285(5430):1036–1039, 1999.
- [21] KW Murch, SJ Weber, C Macklin, and I Siddiqi. Observing single quantum trajectories of a superconducting qubit. *arXiv preprint arXiv:1305.7270*, 2013.

- [22] Y Nakamura, Yu A Pashkin, T Yamamoto, and JS Tsai. Coherent manipulations of charge-number states in a cooper-pair box. *Physica Scripta*, 2002(T102):155, 2002.
- [23] Yu Nakamura, Yu A Pashkin, and JS Tsai. Coherent control of macroscopic quantum states in a single-cooper-pair box. *Nature*, 398(6730):786–788, 1999.
- [24] Harry Nyquist. Thermal agitation of electric charge in conductors. *Physical review*, 32(1):110–113, 1928.
- [25] Aaron D OConnell, M Ansmann, Radoslaw C Bialczak, Max Hofheinz, Nadav Katz, Erik Lucero, C McKenney, Matthew Neeley, Haohua Wang, Eva M Weig, et al. Microwave dielectric loss at single photon energies and millikelvin temperatures. *Applied Physics Letters*, 92(11):112903, 2008.
- [26] David M Pozar. *Microwave engineering*. John Wiley & Sons, 2009.
- [27] Robert Raussendorf and Jim Harrington. Fault-tolerant quantum computation with high threshold in two dimensions. *Phys. Rev. Lett.*, 98:190504, May 2007.
- [28] MD Reed, BR Johnson, AA Houck, L DiCarlo, JM Chow, DI Schuster, L Frunzio, and RJ Schoelkopf. Fast reset and suppressing spontaneous emission of a superconducting qubit. *App. Phys. Lett.*, 96(20):203110–203110, 2010.
- [29] Daniel Sank. Appendix C.
- [30] Daniel Sank. Appendix F.
- [31] Daniel Sank. Appendix A.
- [32] Daniel Sank. Appendix B.
- [33] Daniel Sank. Appendix D.
- [34] Daniel Sank. Appendix E.
- [35] Joannes Schoukens and J Renneboog. Modeling the noise influence on the fourier coefficients after a discrete fourier transform. *IEEE Trans. Instrum. Meas*, 35(3):278–286, 1986.
- [36] D. I. Schuster, A. Wallraff, A. Blais, L. Frunzio, R.-S. Huang, J. Majer, S. M. Girvin, and R. J. Schoelkopf. ac stark shift and dephasing of a superconducting qubit strongly coupled to a cavity field. *Phys. Rev. Lett.*, 94:123602, Mar 2005.
- [37] Peter W Shor. Algorithms for quantum computation: discrete logarithms and factoring. In *Foundations of Computer Science, 1994 Proceedings., 35th Annual Symposium on*, pages 124–134. IEEE, 1994.

- [38] D. H. Slichter, R. Vijay, S. J. Weber, S. Boutin, M. Boissonneault, J. M. Gambetta, A. Blais, and I. Siddiqi. Measurement-induced qubit state mixing in circuit qed from up-converted dephasing noise. *Phys. Rev. Lett.*, 109:153601, Oct 2012.
- [39] Anders Sørensen and Klaus Mølmer. Quantum computation with ions in thermal motion. *Phys. Rev. Lett.*, 82:1971–1974, Mar 1999.
- [40] Caspar H Van der Wal, ACJ Ter Haar, FK Wilhelm, RN Schouten, CJPM Harmans, TP Orlando, Seth Lloyd, and JE Mooij. Quantum superposition of macroscopic persistent-current states. *Science*, 290(5492):773–777, 2000.
- [41] D Vion, A Aassime, A Cottet, P Joyez, H Pothier, C Urbina, D Esteve, and Michel H Devoret. Manipulating the quantum state of an electrical circuit. *Science*, 296(5569):886–889, 2002.
- [42] A Wallraff, DI Schuster, A Blais, L Frunzio, J Majer, MH Devoret, SM Girvin, and RJ Schoelkopf. Approaching unit visibility for control of a superconducting qubit with dispersive readout. *Physical review letters*, 95(6):060501, 2005.
- [43] Andreas Wallraff, David I Schuster, Alexandre Blais, L Frunzio, R-S Huang, J Majer, S Kumar, Steven M Girvin, and Robert J Schoelkopf. Strong coupling of a single photon to a superconducting qubit using circuit quantum electrodynamics. *Nature*, 431(7005):162–167, 2004.
- [44] Tsuyoshi Yamamoto. Private communication.